HOKKAIDO UNIVERSITY

Title	Proposal of a constitutive model for the behavior of unsaturated soils subjected to freeze-thaw action
Author(s)	羅, 斌
Citation	北海道大学. 博士(工学) 甲第13792号
Issue Date	2019-09-25
DOI	10.14943/doctoral.k13792
Doc URL	http://hdl.handle.net/2115/77022
Type	theses (doctoral)
File Information	Luo_Bin.pdf

Instructions for use

Hokkaido University Collection of Scholarly and Academic Papers : HUSCAP

Proposal of a constitutive model for the behavior of unsaturated soils subjected to freeze-thaw action

凍結融解作用を受ける不飽和土の挙動解析に対する

構成モデルの提案

By

Bin LUO

A thesis submitted in partial fulfillment of the requirements for the degree of

Doctor of Philosophy in Engineering

under the guidance and supervision of

Professor Tatsuya Ishikawa

Examined by the Doctoral Committee

Professor Tatsuya Ishikawa

Professor Yoshiaki Fujii

Professor Yoichi Watabe

Professor (Associate) Satoshi Nishimura

September 2019

English Engineering Education Program (e^3)

Laboratory of Analytical Geomechanics

Division of Field Engineering for the Environment

Graduate School of Engineering

Hokkaido University

Sapporo, Hokkaido, Japan

ABSTRACT

The failure of earth structures subjected to freeze-thaw frequently occurs in seasonal cold regions like Hokkaido, Japan. Frost heave and thaw settlement are deemed as two main factors affecting the performance and safety of infrastructures like road, railway, pipeline, and soil slope. Subsurface soils are unsaturated in most cases, however, the estimation method on frost heave and thaw settlement of unsaturated soil are not well established. This study focuses on numerical modeling of freeze-thaw behavior of unsaturated soil, especially on freeze-thaw deformation.

A coupled thermo-hydro-mechanical (THM) model is presented in detail first, which captures the main behaviors of soil subjected to freeze-thaw. For instance, the phase change of water-ice, the reduction of permeability induced by freezing, together with the stiffing of frozen soil are all modeled. More specially, practical experimental equations are applied to model frost heave and thaw settlement. On purpose of validating model, frost heave test was simulated. The model can simulate the correlation between frost heave and water absorption under saturated condition. The influence of overburden pressure on freeze-thaw deformation is also reproduced, however, the model fails to estimate the cooling rate effect. Then, a pavement structure located above a box culvert was simulated to investigate uneven upheave of pavement. After that, stress change in pavement induced by freeze-thaw was studied.

Further development was conducted to overcome the limitations of the above-mentioned model. Recent achievements and progress in unsaturated soil and frozen soil are integrated into the model. Modified governing equations are presented, together with better consideration on nonlinear soil properties. More specifically, attention is paid to the analogy between soil water characteristic curve (SWCC) and soil freezing characteristic curve (SFCC), along with suction induced freezing point depression. Furthermore, ice segregation criteria, frost heave, and direction of thaw settlement are modeled in a more rational way. The validity of the newly proposed model was examined by simulating frost heave test under saturated and unsaturated conditions. Finally, freeze-thaw behavior of an unsaturated soil slope in the seasonal cold region was simulated to verify the applicability of the model for a field-scale problem. The thermal pattern of soil slope is reproduced in which frost penetration at slope top is deeper than that at slope toe and isothermal is not parallel to slope surface. Water redistribution induced by freezing is reproduced together with water-ice phase change and ice accumulation. Mechanism of unique freeze-thaw deformation pattern is revealed. Frost heave generates in heat flow and/or thermal gradient

direction, not necessary to be perpendicular to slope surface, while thaw settlement mainly develops along gravity direction.

In conclusion, a numerical model is proposed for freeze-thaw behavior of unsaturated soil. It is found that the numerical model proposed in this study performs well for estimation on frost have and thaw settlement. The model is ready for field-scale applications to serve design, construction, and maintenance of earth structure in cold regions, although some limitations exist and further verifications are recommended.

ACKNOWLEDGEMENT

First, I would like to express my sincere gratitude to my supervisor Prof. Tatsuya Ishikawa, for his patient guidance, understanding, and support throughout my doctoral program. It is Sensei who introduce me to the field of unsaturated and frozen soil and encourage me to explore unknown. Sensei sets a good example for me in rigorous academic attitude and hard working. The research environment and resource provided by Sensei is also greatly appreciated. Without Sensei's persistent guidance, this dissertation would not have been possible.

Appreciation is due to all members of the doctoral committee, Prof. Yoshiaki Fujii, Prof. Yoichi Watabe and Prof. (Assoc.) Satoshi Nishimura for their constructive comments and suggestions not only on this dissertation but also on annual evaluations. Discussions with Nishimura Sensei has been a great help in understanding the nature of the multi-physics model and inspiring my research.

I am particularly grateful for the assistance given by Prof. Yuzuru Ito, Prof. (Assoc.) Takayuki Kawaguchi, and Prof. (Assoc.) Tetsuya Tokoro. The valuable data provided by them make model validation and verification possible. Sincere thanks are also offered to Prof. Satoshi Akagawa and Dr. Yasushi Ueda for their advice and questions which deepen my understanding of the mechanism of frost heave. I would like to thank the following companies for their assistance with the providing of data, East Nippon Expressway Co., Ltd., and Seiken Co., Ltd.

I would like to offer my sincere thanks to Prof. (Assoc.) Koichi Isobe and Prof. (Asst.) Shoji Yokohama for their supports. I gratefully acknowledge the students of Laboratory of Analytical Geomechanics for their help during my doctoral program. This research was made possible through financial support from the China Scholarship Council (CSC).

Finally, my special thanks are extended to my beloved wife, my parents, family, and friends. Without their encouragement and support all through these years, it would not be possible for me to arrive in Japan and complete my doctoral study at Hokkaido University.

TABLE OF CONTENTS

ABSTRACT i
ACKNOWLEDGEMENT iii
TABLE OF CONTENTS iv
LIST OF FIGURES vii
LIST OF TABLES x
1 INTRODUCTION 1
1.1 BACKGROUND 1
1.2 OBJECTIVES AND METHODOLOGY 3
1.3 ORGANIZATION OF THESIS 4
2 LITERATURE REVIEW 5
2.1 HYDRODYNAMIC MODEL 5
2.2 RIGID ICE MODEL 6
2.3 SEGREGATION POTENTIAL MODEL 6
2.4 THM MODEL 7
2.5 MODEL FOR FREEZE-THAW DEFORMATION OF UNSATURATED SOIL 8
3 MULTIPHYSICS MODELING OF FREEZE-THAW BEHAVIOR 9
3.1 GOVERNING EQUATIONS FOR THERMO-HYDRO-MECHANICAL COUPLING 9
3.1.1 Mass conservation equation for hydraulic field 9
3.1.2 Energy conservation equation for thermal field 11
3.1.3 Equilibrium equation for mechanical field 12
3.1.4 Physical properties under undrained conditions 13
3.1.5 Summary of governing equations 16
3.2 SOIL PROPERTIES FOR UNSATURATED AND FREEZING CONDITION 17
3.2.1 Hydraulic properties 17
3.2.2 Thermal properties 18
3.2.3 Mechanical properties 18
3.3 MODELING OF FREEZE-THAW BEHAVIOR 19
3.3.1 Treatment of freezing and thawing 19
3.3.2 Modeling of frost heave and thaw settlement 20
3.4 SOLVING THE GOVERNING EQUATION 22
3.4.1 Differentiation of time 22
3.4.2 Calculation of displacement 22
3.4.3 Calculation of change of water and heat 23
3.5 FLOW CHART OF COMPUTATION 27
4 MODEL VALIDATION AND APPLICATION 28

4.1 MODEL VALIDATION 28
4.1.1 Simulation of frost heave test 28
4.1.2 Determination of inputs 29
4.1.3 Results and discussions 32
4.1.4 Remarks 34
4.2 THE FREEZE-THAW BEHAVIOR OF PAVEMENT AROUND A BOX CULVERT 35
4.2.1 Problem statement 35
4.2.2 Initial and boundary conditions 37
4.2.3 Results and discussions 37
4.2.4 Remarks 45
4.3 STRESS CHANGE IN PAVEMENT SUBJECTED TO FREEZE-THAW 46
4.3.1 Problem statement 46
4.3.2 Numerical model 46
4.3.3 Results and discussions 49
4.3.4 Remarks 54
5 FURTHER DEVELOPMENT OF MODEL 55
5.1 MODIFIED GOVERNING EQUATIONS 55
5.1.1 Mass conservation equation 55
5.1.2 Energy conservation equation 55
5.1.3 Equilibrium equation 56
5.1.4 Summary of modified governing equations 57
5.2 MODIFIED NONLINEAR SOIL PROPERTIES 57
5.2.1 Hydraulic properties 57
5.2.2 Thermal properties 58
5.2.3 Mechanical properties 59
5.3 SFCC AND ITS DEPENDENCE ON TOTAL WATER SATURATION 59
5.3.1 SFCC derived from SWCC 59
5.3.2 Dependence of SFCC on total water saturation 60
5.4 ICE PRESSURE AND SEGREGATION CRITERION 61
5.5 MODELING OF FROST HEAVE AND THAW SETTLEMENT 61
5.5.1 Frost heave 61
5.5.2 Thaw settlement 62
5.6 SUMMARY ON FURTHER DEVELOPED MODEL 62
5.7 MODEL VALIDATION 1: SIMULATION ON FROST HEAVE (SILT SOIL) 63
5.7.1 A representative frost heave test 63
5.7.2 Performance of model for saturated case 65

5.7.3 Performance of model for unsaturated case 68
5.7.4 Remarks 71
5.8 MODEL VALIDATION 2: SIMULATION ON THAW SETTLEMENT (CLAY SOIL) . 72
5.8.1 Frost heave test 72
5.8.2 Simulation on frost heave test 72
5.8.3 Results and discussions 75
5.8.4 Remarks 78
5.9 MODEL APPLICATION: SIMULATION ON SOIL SLOPE 79
5.9.1 Problem statement 79
5.9.2 Soil properties 80
5.9.3 Initial and boundary conditions 81
5.9.4 Results and discussions 83
5.9.5 Remarks 94
6 CONCLUSIONS AND RECOMMENDATIONS 95
LIST OF REFERENCES 97
LIST OF NOTATIONS 102

LIST OF FIGURES

Figure 1.1 Frost-induced pavement roughness and cracking (After. Hayashi et al., 2006)... 1
Figure 1.2 Horizontal cracking in the sidewall of culvert (After. Hayashi et al., 2006) 2
Figure 1.3 Frost heave damage of the small stage drainage (After. Tozuka et al., 2006)..... 2
Figure 1.4 Surface collapse of slope due to thaw settlement (After. Ueno et al., 2010) 3
Figure 3.1 Treatment of latent heat during freezing 19
Figure 3.2 Modeling volume change during the freeze-thaw process..... 21
Figure 3.3 Element division and calculation of flow velocity..... 24
Figure 3.4 Boundary elements and boundary conditions 26
Figure 3.5 Flowchart of THM analysis 27
Figure 4.1 Experimental apparatus for frost heave test 28
Figure 4.2 Simulation boundary conditions for frost heave test 29
Figure 4.3 Dependence of permeability on effective stress..... 30
Figure 4.4 SWCC of Touryo soil..... 30
Figure 4.5 Evaluation of fitting frost heave ratio 31
Figure 4.6 Fitting of thaw contraction coefficient..... 31
Figure 4.7 Influence of water supply on frost heave 33
Figure 4.8 Influence of overburden pressure on frost heave 33
Figure 4.9 Influence of cooling rate on frost heave..... 34
Figure 4.10 Box culvert profile and finite element mesh 35
Figure 4.11 Comparison of temperature variation at the back of culvert 38
Figure 4.12 Temperature distribution at the start of freeze process 39
Figure 4.13 Temperature distribution at the end of freeze process..... 39
Figure 4.14 Uneven freeze-thaw deformation of pavement in freeze process 40
Figure 4.15 Uneven freeze-thaw deformation of pavement in thaw process 41
Figure 4.16 Comparison of stress variation of reinforcement 42
Figure 4.17 Distribution of principal stress vector in freeze process 42
Figure 4.18 Countermeasure against frost heave: layout of XPS..... 43
Figure 4.19 Fatigue life and roughness of pavement under different thermal and load combination conditions 44
Figure 4.20 Profile of simulated pavement 47
Figure 4.21 Temperature boundary in simulation 49
Figure 4.22 Temperature history in the pavement 50
Figure 4.23 Temperature distribution on March 1st 50
Figure 4.24 Temperature distribution on April 1st 51
Figure 4.25 Stress variation in the pavement 52

Figure 4.26 Temperature and stress at the top of the subgrade 53
Figure 4.27 An allowable number of equivalent wheel load and change of stress at the top of the subgrade 54
Figure 5.1 Schematic interpretation of THM coupling 62
Figure 5.2 Volumetric total water content, and temperature profile 63
Figure 5.3 Pore-water pressure and relative hydraulic conductivity profiles 64
Figure 5.4 Volumetric water and ice content profile and frost heave ratio relationship 65
Figure 5.5 Simulation on correlation of water migration and frost heave 66
Figure 5.6 Simulation on influence of overburden for open-system: Frost heave 66
Figure 5.7 Simulation on the influence of overburden for open-system: Thaw settlement 67
Figure 5.8 Simulation on influence of cooling rate for open-system: Frost heave 67
Figure 5.9 Simulation on influence of cooling rate for open-system: Thaw settlement 68
Figure 5.10 Simulation on influence of overburden for closed-system: Frost heave 69
Figure 5.11 Simulation on influence of overburden for closed-system: Thaw settlement .. 69
Figure 5.12 Simulation on influence of initial saturation for closed-system: Frost heave .. 70
Figure 5.13 Simulation on influence of initial saturation for closed-system: Thaw settlement 70
Figure 5.14 Time history of the pedestal and top plate temperature 72
Figure 5.15 Frost heave and water absorption 73
Figure 5.16 Determination of thaw settlement coefficient 74
Figure 5.17 Boundary conditions - open system (freezing) 75
Figure 5.18 Boundary conditions - open system (thawing) 75
Figure 5.19 The relationship between frost heave and water absorption 76
Figure 5.20 Influence of permeability on consolidation 76
Figure 5.21 Relationship between thaw settlement and water drainage 77
Figure 5.22 The influence of overburden pressure on frost heave 78
Figure 5.23 Size, instrument configuration, mesh and boundary conditions of slope 80
Figure 5.24 Daily average air temperature and temperature at slope surface 82
Figure 5.25 Ground temperature at 30 cm depth 83
Figure 5.26 Variation of frost penetration depth 84
Figure 5.27 Simulated temperature distribution on March 1st, 2005 (Unit: Celsius degree) 85
Figure 5.28 Simulated heat flow vector in slope on March 1st, 2005 (Unit: W/m^2) 85
Figure 5.29 Simulated liquid-water saturation distribution on March 1st, 2005 86
Figure 5.30 Simulated total-water saturation distribution on March 1st, 2005 86
Figure 5.31 Simulated water redistribution during November 1st, 2004 to March 1st, 2005

..... 87
Figure 5.32 Simulated latent heat for water-ice phase change on March 1st, 2005 (Unit: J) 88
Figure 5.33 Simulated pore-water pressure distribution on March 1st, 2005 (Unit: MPa) . 88
Figure 5.34 Simulated water flow vector in slope on March 1st, 2005 (Unit: m/h)..... 89
Figure 5.35 Simulated frost heave deformation on March 1st, 2005 (Unit: m) 89
Figure 5.36 Simulated thaw settlement deformation on May 29th, 2005 (Unit: m) 90
Figure 5.37 Deformation perpendicular to slope surface 91
Figure 5.38 Deformation along slope surface 91
Figure 5.39 Trajectory of upper measuring target 92
Figure 5.40 Trajectory of middle measuring target 92
Figure 5.41 Trajectory of lower measuring target 93

LIST OF TABLES

Table 2.1 Models proposed for freeze-thaw deformation of unsaturated soils 8
Table 4.1 Input parameters in frost-heave test analysis of Touryo soil 32
Table 4.2 Input parameters in box culvert analysis 36
Table 4.3 Input parameters in pavement analysis..... 48
Table 5.1 Summarization of test conditions and results of Fujinomori soil 73
Table 5.2 Input parameters in frost-heave test analysis of Fujinomori soil..... 74
Table 5.3 Input parameters in soil slope analysis 81

1 INTRODUCTION

1.1 BACKGROUND

The sustainable development of society fairly relies on infrastructure providing transport convenience and keeping human beings safe. As well known, more than 50 percent of land in the northern hemisphere is in cold region and exposed to seasonal climatic change, which leads to the cyclic freeze-thaw of the ground. This severe temperature variation often damages or degrades the performance of infrastructure like road, railway, as well as a pathway of the airfield. The soil is a type of construction material widely present in various earth structure, which also undergoes the seasonal freeze-thaw process. Unlike the artificially frozen soil in the deep ground, the soil under nature freezing condition is partially saturated right below ground surface in most cases. The freeze-thaw action of this unsaturated subsurface soil, together with the structure above or in it, is the main concern shared by researchers and practitioners for decades.

Accompanying with the freeze-thaw process, the frost heave of subsurface soil often causes severe roughness and cracking of structures like pavements (Figure 1.1). More seriously, the subsequent thaw weakening may further damage the structure and cause traffic volume restriction. Apparently, the safety and comfort of driving on this kind of pavement are profoundly affected, and structural failures and maintenance costs are increased.

Figure 1.1 Frost-induced pavement roughness and cracking (After. Hayashi et al., 2006)

The frost heave not only occurs in the surface structure with low overburden but also in underground structure with high confining pressure (Figure 1.2). The frost heaving force is the

main concern in this case which may crack the reinforced concrete structure. In a seasonal cold region, the distress of the drainage system induced by frost heave is also reported (Figure 1.3) together with surface collapse of slope due to freeze-thaw (Figure 1.4). According to all these structure failures, we observe that the frost heave plays a key role, and this heaving often takes place in partially saturated soil which is generally believed not susceptible to freezing and heaving.

Figure 1.2 Horizontal cracking in the sidewall of culvert (After. Hayashi et al., 2006)

Figure 1.3 Frost heave damage of the small stage drainage (After. Tozuka et al., 2006)

Figure 1.4 Surface collapse of slope due to thaw settlement (After. Ueno et al., 2010)

1.2 OBJECTIVES AND METHODOLOGY

The objective of this study is to propose a numerical model to characterize the primary behavior of unsaturated soil subjected to freeze-thaw, mainly interested in frost heave and thaw settlement. Since the freeze-thaw is a complex process involving seepage, thermal transfer, phase change, and deformation, a multi-physical model is required to comprehensively capture the behavior in each field and interactions between them.

To achieve this objective, the governing equation for each field should involve the influence of other fields. Also, the soil properties in one field may affected by another. For example, the freezing of soil may reduce the water permeability and increase the stiffness of soil. All these complexities get freeze-thaw become a nonlinear problem. Only by providing a model properly integrating all these considerations together, we can predict the behavior of unsaturated freezing soil correctly.

Besides the general aspects of freeze-thaw behavior concerned by the community, the freezing-induced heaving, and subsequent thaw weakening draw author's attention. The modeling of these behaviors is considerably essential both to theory advance and requisite in practice.

For all these purposes, the modeling and its validation is the main task of this study. Checking the performance of the proposed model from the element test scale to field application scale is

required to make it an applicable analysis tool.

1.3 ORGANIZATION OF THESIS

This dissertation is divided into six chapters.

Chapter 1 Introducing the background of this study. The objective, purpose, and main task are briefly presented. The organization of this dissertation is also outlined.

Chapter 2 Presenting the state of art for unsaturated freezing soil including four typical types of coupling models for freezing soil and frost heave.

Chapter 3 Introducing a coupled thermo-hydro-mechanical model. The formula of governing equations, soil properties, frost heave, thaw settlement, and numerical implementation are explained in detail.

Chapter 4 Presenting the validation of the model by simulating the frost heave test. Thereafter, a case study is performed to research the freeze-thaw behavior of pavement around a box culvert. One more simulation is conducted on stress change in pavement subjected to freeze-thaw.

Chapter 5 Introducing further development on the existing model. The modified governing equation, soil properties, modeling of frost heave and thaw settlement are explained. Special concerns on SFCC for unsaturated soil and the dependence of SFCC on total water saturation is introduced. Performance of the further developed model is examined by simulation frost heave test under saturated and unsaturated conditions. Finally, a case study on a soil slope in seasonal cold region is simulated to reveal special deformation pattern during freeze-thaw process.

Chapter 6 Summarizing the finds and conclusions of this research.

2 LITERATURE REVIEW

Frost heave and thaw settlement cause damages to various engineering structures like road, railway, pipeline, slope, and retaining wall in cold region. The mechanism of frost heave has been studied for decades and different hypothesis (primary heave or secondary heave) proposed to explain the formation and growth of ice lens which contributes to the uplift of the ground surface. Temperature, moisture, and soil properties are generally deemed as three primary factors affecting frost heave, as well as overburden pressure which is also believed having great impact on heaving (Konrad and Morgenstern, 1982). Estimation on frost heave amount draws wide attentions from practical engineer and researchers. The numerical model is necessary to describe the behavior of freezing soil which is complicated and hard to be captured by analytical equation. Similarly, the numerical method like finite element method (FEM) and finite difference method (FDM) are required to solve mathematical formula due to the nature that freezing and thawing of soil is a transient process. Three typical models first come into mind when we come to frost heave model, including hydrodynamic model, rigid ice model, and segregation potential model.

2.1 HYDRODYNAMIC MODEL

In the early stage of model development, the freezing of soil is mainly related to heat and flow transport process, along with the interaction between these two fields which is also known as coupled heat-flow analysis. The hydraulic analogy between partially frozen soil and unsaturated soil without ice was studied for different types of soils (Koopmans and Miller, 1966). It is believed that Harlan (1973) proposed the first hydrodynamic model and pointed out analogy can be made between the mechanisms of water transport in partially frozen soils and those in unsaturated soils. By use of this analogy, a Darcian approach is applied to the analysis of coupled heat-fluid transport in porous media with freezing and thawing. Water redistribution and infiltration to frozen soil are examined from a phenomenological point of view, and the effects of soil type and initial conditions on the response of a hypothetical soil column are studied. A one-dimensional model of these processes was developed by Guymon and Luthin (1974) and was based on an equivalent quasilinear variational functional for the Richards equation and the heat conduction equation including convective components. Taylor and Luthin (1978) performed analyses utilize a modified form of a model presented by Harlan. Later, Guymon et al. (1980) further developed a macro thermodynamic model that simulates heat and moisture transfer from an element of soil undergoing freezing to compute frost heave. It is assumed that a portion of water in the element will not freeze, and all water in addition to this amount that freezes in excess of the soil porosity results in a corresponding heave. The freezing process is assumed to be isothermal. A two-dimensional model of coupled heat and moisture flow in frost-heaving soils was developed based upon well-known equations of heat and moisture flow in soils by Guymon et al. (1984).

Newman and Wilson (1997) presented an approach for predicting heat and mass transfer in freezing unsaturated soil when frost heave does not occur. The theoretical formulation uses soil-freezing and soil-water characteristic curve data to combine the heat and mass transfer relationships into a single equation for freezing or frozen regions of the soil. Hansson et al. (2004) presented a new method to account for phase changes in a fully implicit numerical model for coupled heat transport and variably saturated water flow involving conditions both above and below zero temperature. The method is based on a mixed formulation for both water flow and heat transport similar to the approach commonly used for the Richards equation. Painter and Karra (2014) proposed a constitutive relation for phase partitioning of water in unsaturated frozen soils. This relation compares well with existing experimental data on unfrozen water content as a function of temperature for different total water content values.

2.2 RIGID ICE MODEL

For rigid ice model, it is assumed that soil ice grows and moves as a rigid body. This type of model is put forward to physically model a special zone that is frozen fringe in frost-heaving soil, also initiation criteria and growth of discrete ice lens are well studied based on secondary heave theory. Miller (1978) first proposed the concept of rigid ice model. Gilpin (1980) proposed a model predicting ice lensing and heave rates as a function of the basic soil properties (thermal conductivities and particle size) and the externally applied boundary conditions (surface temperatures and overburden pressure). O'Neill and Miller (1985) conducted analysis concentrating on activity within the fringe, also connecting that activity to heat and mass flows in the more frozen and unfrozen zones. Each component in a set of governing differential equations is developed from rational physics and thermodynamics, using previous experimental work. It is assumed that the soil-ice grows through interconnected interstices; hence it constitutes and can move as a rigid body. Sheng et al. (1995, 2013) developed a frost heave model which simulates the formation of ice lenses for saturated salt-free soils. Quasi-steady state heat and mass flow were considered. The neutral stress was determined as a simple function of the unfrozen water content and porosity.

2.3 SEGREGATION POTENTIAL MODEL

The segregation potential model for frost heave prediction is a semiempirical method which relates heaving rate to temperature gradient behind frost front in freezing soil. Konrad and Morgenstern (1980) revealed that freezing soil can be characterized by two parameters, the segregation-freezing temperature and the overall permeability of the frozen fringe. Konrad and Morgenstern's (1981) paper showed experimentally that the segregation potential was also a function of the average suction in the frozen fringe which was readily expressed in terms of the

suction at the frost front. As a result, it is also shown that measured water intake flux during freezing is dependent on the freezing path used to initiate the final ice lens. A thermodynamic explanation of the dependence of segregation potential on suction in the frozen fringe is also offered. Konrad and Morgenstern (1984) presented a procedure for calculating the amount of heave under a chilled gas pipeline based on a finite-difference formulation of the heat and mass transfer in saturated soils. The frost heave of the soil is characterized in terms of the segregation potential concept developed in earlier papers by the authors.

2.4 THM MODEL

Although above-mentioned models have many merits, shortcoming and limitation are remain that the stress is only introduced as a factor affecting ice lens initial or heaving rate (Mu and Ladanyi, 1987). A trend on merging heat-moisture analysis with stress analysis arises as frost expansion and stress field all are interested in by researchers.

Li et al. (2000, 2002) established the theoretical frame for the heat-moisture-deformation coupling behaviors of the freezing soil, based on the equilibrium, continuity and energy principles of the soil particle, ice and water three-phase porous medium, with the consideration of the force interaction between the soil skeleton and ice particle, and the energy jump behaviors during the phase-changing between ice and water. Li et al. (2008) further discussed the air phase in the unsaturated freezing soil in two ideal situations: air in the soil is linked to the atmosphere (the open porous medium) and air in the soil is isolated from the atmosphere (the sealed porous medium). The corresponding theoretical modeling framework for a multi-phase porous medium with the interaction of water, heat, and deformation is established. Nishimura et al. (2009) presented a fully coupled THM finite element (FE) formulation that considers freezing and thawing in water-saturated soils. The formulation considers each thermal, hydraulic and mechanical process, and their various interactions, through fundamental physical laws and models. By employing a combination of ice pressure, liquid pressure and total stress as state variables, a new mechanical model has been developed that encompasses frozen and unfrozen behavior within a unified effective-stress-based framework. Thomas et al. (2009) presented coupled THM model, which is solved by way of a transient finite element approach, considers a number of processes, including conduction, convection, phase change, the movement of moisture due to cryogenic suctions, and the development of ice lenses. Liu and Yu (2011) introduced the development and implementation of a multiphysical model to simulate the coupled hydro-thermo-mechanical processes in freezing unsaturated porous materials. The model couples the Fourier's law for heat transfer, the generalized Richards' equation for fluid transfer in unsaturated media, and the mechanical constitutive relationship. Zhang and Michalowiski (2015) developed the constitutive model, capable of simulating freezing and thawing of soils, and associated changes in the soil

strength.

2.5 MODEL FOR FREEZE-THAW DEFORMATION OF UNSATURATED SOIL

These models provide us good insights into thermo-hydro-mechanical behavior of freezing soil, however, most of them are set up for saturated soils. As well known, the subsurface soil where is exposed to weather change is partially saturated in most cases. More recently, the significance of vapor flow on water redistribution and heaving in unsaturated freezing is described in which very low groundwater level and sealed top boundary were expected and assigned (Zhang et al, 2016; Yin et al, 2018). However, the liquid water flow may still dominate mass movement in unsaturated soils with relatively high saturation as higher water saturation blocks pathway and suppresses vapor flow.

A numerical model is expected to predict both frost heave and thaw settlement of unsaturated soil. Special concerns are paid on the 2D application and actions in T-H-M fields and model validation. Existing models are listed in Table 2.1, which are proposed for frost heave and/or thaw settlement of unsaturated soil. There are few models can predict both frost heave and thaw settlement of unsaturated soil with proper consideration on behaviors in all THM fields. Most importantly, it is fairly essential to verify the model from a laboratory element test scale to field-scale application.

Table 2.1 Models proposed for freeze-thaw deformation of unsaturated soils

Numerical model reference	Frost heave	Thaw settlement	Number of dimensions	Multi-field	Model verification/ validation
Corapcioglu and Panday (1995)	No	Yes	1D	T-H	-
Shoop and Bigl (1997)	Yes	Yes	1D	T-H	Model test
Li et al. (2008)	Yes	No	2D	T-H-M	Field data
Li et al. (2015)	Yes	Yes	2D	T-H combined M	Model test
Zheng and Kanie (2015)	Yes	No	2D	Combined THM	-
Tai et al. (2017)	Yes	Yes	2D	T-H	Field data

Existing models proposed for predicting frost heave or thaw settlement of unsaturated soil.
T: Thermal H: Hydraulic M: Mechanical

3 MULTIPHYSICS MODELING OF FREEZE-THAW BEHAVIOR

This chapter first presents the mathematical model that is a derivation of equations which govern behaviors in hydraulic, thermal and mechanical fields. Then nonlinear soil properties are described, as well as modeling of freeze-thaw processes and frost heave. Finally, solving of governing equations and flow chart of computation are explained.

3.1 GOVERNING EQUATIONS FOR THERMO-HYDRO-MECHANICAL COUPLING

3.1.1 Mass conservation equation for hydraulic field

The mass conservation law must be followed for continuity flow in porous material, no matter it happens in partially saturated soil with positive temperature or in freezing soil with water migration due to subzero temperature. Neglecting water in air phase (vapor) and taking account of liquid water, mass conservation equation is given in the form of,

$$\frac{\partial M_w}{\partial t} = -\nabla \cdot \left(\rho_w \boldsymbol{v_w} \right) \tag{3.1}$$

where M_w is mass of water; t is time; $\nabla\cdot$ is divergence operator; ρ_w is density of water; and $\boldsymbol{v_w}$ is flux vector of water.

Introducing the relation between mass and corresponding volumetric water content, Equation 3.1 is represented as,

$$\frac{\partial \left(\rho_w S_w n \right)}{\partial t} = -\nabla \cdot \left(\rho_w \boldsymbol{v_w} \right) \tag{3.2}$$

where n is porosity; and S_w is degree of saturation for liquid water. The right side of the equation represents mass change of liquid pore-water in unit volume over unit time. The left side of equation implies that the mass change dependents on change of water density, porosity and degree of saturation for water. Taking derivative of the left side of Equation 3.2 with respect to these three factors,

$$\frac{\partial \left(\rho_w S_w n \right)}{\partial t} = S_w n \frac{\partial \rho_w}{\partial t} + \rho_w n \frac{\partial S_w}{\partial t} + \rho_w S_w \frac{\partial n}{\partial t} \tag{3.3}$$

For the first term on the right side in Equation 3.3, considering given water mass, the equation below holds,

$$dM_w = d\left(\rho_w V_w \right) = V_w d\rho_w + \rho_w dV_w = 0 \tag{3.4}$$

where V_w is volume of water. The change of water density is expressed as,

$$d\rho_w = -\rho_w \frac{dV_w}{V_w} = -\rho_w \varepsilon_w \tag{3.5}$$

where ε_w is strain of water which could be induced by various factors like mechanical compression

and thermal expansion.

$$d\rho_w = -\rho_w \varepsilon_w = -\rho_w \left(\frac{1}{K_w} du_w + \alpha_{Tw} dT \right) \tag{3.6}$$

where K_w is bulk modulus of water; u_w is pore-water pressure; α_{Tw} is thermal expansion coefficient of water; and T is temperature. The first term on the right side in Equation 3.3 is rewritten as,

$$S_w n \frac{\partial \rho_w}{\partial t} = -\rho_w S_w n \frac{1}{K_w} \frac{\partial u_w}{\partial t} - \rho_w S_w n \alpha_{Tw} \frac{\partial T}{\partial t} \tag{3.7}$$

For the second term on the right side in Equation 3.3, introducing the relation between degree of saturation and pore-water pressure in unsaturated-saturated soil mechanics and applying derivative chain rule,

$$\rho_w n \frac{\partial S_w}{\partial t} = \rho_w n \frac{\partial S_w}{\partial u_w} \frac{\partial u_w}{\partial t} \tag{3.8}$$

More familiarly, the concept of specific moisture capacity of soil, which defines as the volume of water released or absorbed per unit volume soil to the change of matrix suction. It is also known as the slope of soil water characteristic curve (SWCC).

$$C_H = \frac{d\left(V_w / V_0\right)}{du_w} = \frac{d\theta_w}{du_w} \cong n \frac{dS_w}{du_w} \tag{3.9}$$

where C_H is specific moisture capacity of soil; V_0 is volume of soil element; and θ_w is volumetric water content. Substituting Equation 3.9 into Equation 3.8 then,

$$\rho_w n \frac{\partial S_w}{\partial t} = \rho_w C_H \frac{\partial u_w}{\partial t} \tag{3.10}$$

For the third term on the right side in Equation 3.3, the change of porosity is equivalent as a change of volumetric strain of soil, as soil herein is treated as elastic porous material. Furthermore, soil particles are much stiffer than pore fluid, then volumetric strain is attributed to compression of soil skeleton. For small strain problem,

$$\rho_w S_w \frac{\partial n}{\partial t} = \rho_w S_w \frac{\partial \varepsilon_v}{\partial t} = \rho_w S_w \frac{\partial \left(\nabla \cdot \boldsymbol{u} \right)}{\partial t} \tag{3.11}$$

where ε_v is volumetric strain of soil element; $\boldsymbol{u}$ is displacement vector of soil element. Substituting Equation 3.7, 3.10 and 3.11 into Equation 3.3 then

$$\begin{aligned} \frac{\partial \left(\rho_w S_w n \right)}{\partial t} &= -\rho_w S_w n \frac{1}{K_w} \frac{\partial u_w}{\partial t} - \rho_w S_w n \alpha_{Tw} \frac{\partial T}{\partial t} + \rho_w C_H \frac{\partial u_w}{\partial t} + \rho_w S_w \frac{\partial \left(\nabla \cdot \boldsymbol{u} \right)}{\partial t} \\ &= \rho_w \left(C_H - \frac{S_w n}{K_w} \right) \frac{\partial u_w}{\partial t} - \rho_w S_w n \alpha_{Tw} \frac{\partial T}{\partial t} + \rho_w S_w \frac{\partial \left(\nabla \cdot \boldsymbol{u} \right)}{\partial t} \end{aligned} \tag{3.12}$$

Combining Equation 3.12 and Equation 3.2,

$$\frac{1}{\rho_w} \nabla \cdot \left(\rho_w \boldsymbol{v_w} \right) = \frac{1}{K_b} \frac{\partial u_w}{\partial t} + S_w n \alpha_{Tw} \frac{\partial T}{\partial t} - S_w \frac{\partial \left(\nabla \cdot \boldsymbol{u} \right)}{\partial t} \tag{3.13}$$

$$\frac{1}{K_b} = \frac{S_w n}{K_w} - C_H \tag{3.14}$$

where K_b is a physical property value equivalent to the reciprocal of volume elastic constant of the pore water in the unsaturated region.

Darcy's law is applied to describe the flow of water through soil.

$$\boldsymbol{v_w} = -k_w \nabla h \tag{3.15}$$

$$h = \frac{u_w}{\rho_w g} + z \tag{3.16}$$

where k_w is coefficient of water permeability; ∇ is gradient operator; h is total hydraulic potential head; z is elevation with respect to a reference; and g is gravity acceleration.

For unsaturated soil, the coefficient of water permeability is smaller than that under the saturated case, and concept of relative hydraulic conductivity is introduced here.

$$k_w = k_{wr} k_s \tag{3.17}$$

where k_{wr} is relative water hydraulic conductivity; and k_s is saturated water hydraulic conductivity.

The left side of the Equation 3.13 is the change of water volume in unit volume per unit time, and it is described as follows,

$$\frac{\partial m}{\partial t} = \frac{1}{\rho_w} \nabla \cdot \left(\rho_w \boldsymbol{v_w} \right) \tag{3.18}$$

where m is storage volume of water per unit volume.

Finally, continuity equation is written as follow,

$$\frac{\partial m}{\partial t} = \frac{1}{K_b} \frac{\partial u_w}{\partial t} + S_w n \alpha_{Tw} \frac{\partial T}{\partial t} - S_w \frac{\partial \left(\nabla \cdot \boldsymbol{u} \right)}{\partial t} \tag{3.19}$$

3.1.2 Energy conservation equation for thermal field

The energy conservation in porous material is given as,

$$C_T \frac{\partial T}{\partial t} = \nabla \cdot \left(-\lambda_T \nabla T \right) - C_{Tw} \nabla \cdot \left(\boldsymbol{v_w} T \right) \tag{3.20}$$

where C_T is volumetric heat capacity of soil; λ_T is thermal conductivity of soil; and C_{Tw} is volumetric heat capacity of water. The first term on the right side represents conductive heat transfer, which is referred to as Fourier formula. The heat advected by water flow is described as the second term on the right side of the equation.

For freezing soil, the phase change from water to ice plays a key role in heat transfer,

$$C_T \frac{\partial T}{\partial t} + L \frac{\partial \theta_i}{\partial t} = \nabla \cdot \left(-\lambda_T \nabla T\right) - C_{Tw} \nabla \cdot \left(\boldsymbol{v}_w T\right) \tag{3.21}$$

where L is latent heat of fusion of water. Introducing the ice content and negative temperature, taking the derivative chain rule,

$$\frac{\partial \theta_i}{\partial t} = \frac{\partial \theta_i}{\partial T} \frac{\partial T}{\partial t} \tag{3.22}$$

where θ_i is volumetric ice content; and $\partial\theta_i/\partial T$ is the slope of soil freezing characteristic curve (SFCC) describing unfrozen water content and negative temperature relation.

Substituting Equation 3.22 into Equation 3.21, the energy conservation equation is given as,

$$\left(C_T + L \frac{\partial \theta_i}{\partial T}\right) \frac{\partial T}{\partial t} = \nabla \cdot \left(-\lambda_T \nabla T\right) - C_{Tw} \nabla \cdot \left(\boldsymbol{v}_w T\right) \tag{3.23}$$

3.1.3 Equilibrium equation for mechanical field

Assuming soil behaves as a linear and isotropic material, the strain-stress relation is expressed as,

$$\frac{\sigma'_m}{\partial t} = K_d \frac{\partial \varepsilon_v}{\partial t} \tag{3.24}$$

where σ'_m is mean effective stress; and K_d is bulk modulus for the soil structure under drained conditions.

According to Bishop's effective stress law (Bishop, 1959), introducing pore-water pressure, the constituent equation becomes the following equation,

$$\frac{\partial \sigma_m}{\partial t} = \frac{\partial \sigma'_m}{\partial t} + S_w \frac{\partial u_w}{\partial t} = K_d \frac{\partial \varepsilon_v}{\partial t} + S_w \frac{\partial u_w}{\partial t} \tag{3.25}$$

where σ_m is mean total normal stress.

Rewriting Equation 3.25 with respect to volumetric strain

$$\frac{\partial \varepsilon_v}{\partial t} = \frac{1}{K_d} \frac{\partial \sigma_m}{\partial t} - \frac{S_w}{K_d} \frac{\partial u_w}{\partial t} \tag{3.26}$$

The strain induced by temperature change has a dilatational character, causing thermal expansion or contraction and do not cause shear. The thermal strain is proportional to temperature change. The phase change of water-ice also causes volumetric expansion when soil is freezing under subzero temperature.

$$\frac{\partial \varepsilon_v}{\partial t} = \frac{1}{K_d} \frac{\partial \sigma_m}{\partial t} - \frac{S_w}{K_d} \frac{\partial u_w}{\partial t} + \alpha_{Td} \frac{\partial T}{\partial t} + \frac{\partial \varepsilon_{f/t}}{\partial t} \tag{3.27}$$

where α_{Td} is thermal expansion coefficient of soil under drained condition; and $\varepsilon_{f/t}$ is frost heave or thaw settlement strain.

Again, rewriting Equation 3.27 with respect to mean total stress

$$\frac{\partial \sigma_m}{\partial t} = K_d \frac{\partial \varepsilon_v}{\partial t} + S_w \frac{\partial u_w}{\partial t} - K_d \alpha_{Td} \frac{\partial T}{\partial t} - K_d \frac{\partial \varepsilon_{f/t}}{\partial t} \tag{3.28}$$

From the constituent equation and the continuity equation, the term of water pressure can be eliminated. First, rewrite the continuity equation represented by Equation 3.19 as,

$$\frac{\partial u_w}{\partial t} = K_b \frac{\partial m}{\partial t} - K_b S_w n \alpha_{Tw} \frac{\partial T}{\partial t} + K_b S_w \frac{\partial (\nabla \cdot \boldsymbol{u})}{\partial t} \tag{3.29}$$

Substituting Equation 3.29 into Equation 3.28, the following equation is finally obtained.

$$\begin{aligned} \frac{\partial \sigma_m}{\partial t} &= K_d \frac{\partial \varepsilon_v}{\partial t} + S_w \left(K_b \frac{\partial m}{\partial t} - K_b S_w n \alpha_{Tw} \frac{\partial T}{\partial t} + K_b S_w \frac{\partial (\nabla \cdot \boldsymbol{u})}{\partial t} \right) - K_d \alpha_{Td} \frac{\partial T}{\partial t} - K_d \frac{\partial \varepsilon_{f/t}}{\partial t} \\ &= \left(K_d + K_b S_w^2 \right) \frac{\partial \varepsilon_v}{\partial t} + K_b S_w \frac{\partial m}{\partial t} - \left(K_b S_w^2 n \alpha_{Tw} + K_d \alpha_{Td} \right) \frac{\partial T}{\partial t} - K_d \frac{\partial \varepsilon_{f/t}}{\partial t} \end{aligned} \tag{3.30}$$

Then, the constituent equation can be written as follows,

$$\frac{\partial \sigma_m}{\partial t} = K \frac{\partial \varepsilon_v}{\partial t} + \frac{\partial \sigma_0}{\partial t} \tag{3.31}$$

$$K = K_d + K_b S_w^2 \tag{3.32}$$

$$\frac{\partial \sigma_0}{\partial t} = K_b S_w \frac{\partial m}{\partial t} - \left(K_b S_w^2 n \alpha_{Tw} + K_d \alpha_{Td} \right) \frac{\partial T}{\partial t} - K_d \frac{\partial \varepsilon_{f/t}}{\partial t} \tag{3.33}$$

where K is bulk modulus for the soil structure.

Constitutive equation including the shear component is as follows,

$$\frac{\partial \sigma_{ij}}{\partial t} = \left(K - \frac{2}{3} G \right) \frac{\partial \varepsilon_{kk}}{\partial t} \delta_{ij} + 2G \frac{\partial \varepsilon_{ij}}{\partial t} + \frac{\partial \sigma_0}{\partial t} \delta_{ij} \tag{3.34}$$

where σ_{ij} is total stress tensor; G is shear modulus for the soil structure; ε_{kk} is mean strain tensor; ε_{ij} is infinitesimal strain tensor; and δ_{ij} is Kronecker delta.

In addition, the static equilibrium equation is given as,

$$\sigma_{ij,j} + \rho g_i = 0 \tag{3.35}$$

Considering the displacement-strain relation, the equation to be finally solved is obtained.

$$\left\{ \frac{1}{2} C_{ijkl} \left(u_{k,l} + u_{l,k} \right) + \sigma_0 \delta_{ij} \right\}_{,j} + \rho g_i = 0 \tag{3.36}$$

where C_{ijkl} is elastic constant tensor.

3.1.4 Physical properties under undrained conditions

In conducting the simulation, it is necessary to obtain physical property values such as K_b, α_{Tw},

and α_{Td} as mentioned above. Performing experiments controlling deformation, temperature, and pore-water pressure to obtain these physical properties. Finally, constituent equations are simplified by substituting obtained physical property values under undrained condition.

Undrained bulk modulus

First, let us consider a case where an isotropic loading test is performed under an undrained and isothermal condition using a saturated sample, and the undrained bulk modulus K_u is obtained.

$$\frac{\partial \varepsilon_v}{\partial t} = \frac{1}{K_u}\frac{\partial \sigma_m}{\partial t} \tag{3.37}$$

Alternatively, writing to the mean stress by the following equation.

$$\frac{\partial \sigma_m}{\partial t} = K_u \frac{\partial \varepsilon_v}{\partial t} \tag{3.38}$$

At the same time, the pore-water pressure is measured, and it is considered that the ratio β to the mean stress was obtained.

$$\frac{\partial u_w}{\partial t} = \beta \frac{\partial \sigma_m}{\partial t} \tag{3.39}$$

where β is pore-pressure coefficient B (Skempton, 1954).

Combining Equation 3.38 and 3.39, σ_m is eliminated.

$$\frac{\partial u_w}{\partial t} = \beta K_u \frac{\partial \varepsilon_v}{\partial t} \tag{3.40}$$

On the other hand, from the continuity equation of water, Equation 3.19, the following equation is obtained by taking undrained saturated condition into account.

$$\frac{\partial m}{\partial t} = \frac{1}{K_b}\frac{\partial u_w}{\partial t} - S_w \frac{\partial \varepsilon_v}{\partial t} = 0 \tag{3.41}$$

$$\frac{\partial u_w}{\partial t} = K_b \frac{\partial \varepsilon_v}{\partial t} \tag{3.42}$$

Comparing the coefficients in Equation 3.40 and 3.42, the following relationship exists.

$$\beta K_u = K_b \tag{3.43}$$

Furthermore, from Equation 3.30, in view of the undrained condition,

$$\frac{\partial \sigma_m}{\partial t} = \left(K_d + K_b\right)\frac{\partial \varepsilon_v}{\partial t} \tag{3.44}$$

Comparing the coefficients in Equation 3.38 and 3.44, then

$$K_u = K_d + K_b \tag{3.45}$$

Substituting Equation 3.45 into Equation 3.43,

$$\beta\left(K_d + K_b\right) = K_b \tag{3.46}$$

$$K_b = \frac{\beta}{1-\beta} K_d \tag{3.47}$$

$$K_u = \frac{1}{1-\beta} K_d \tag{3.48}$$

Regarding the unsaturated case, when determining the volume elastic constant under undrained conditions, keep Equation 3.14 in mind, then following relation is obtained.

$$K_b = -\frac{1}{C_H} \tag{3.49}$$

Thermal expansion coefficient

Next, a thermal expansion test is performed under undrained conditions to obtain thermal expansion coefficient of soil under undrained condition α_{Tu}.

$$\frac{\partial \varepsilon_v}{\partial t} = \alpha_{Tu} \frac{\partial T}{\partial t} \tag{3.50}$$

According to the constitutive Equation 3.30 for the undrained condition,

$$\frac{\partial \sigma_m}{\partial t} = \left(K_d + K_b S_w^2\right) \frac{\partial \varepsilon_v}{\partial t} - \left(K_b S_w^2 n \alpha_{Tw} + K_d \alpha_{Td}\right) \frac{\partial T}{\partial t} \tag{3.51}$$

Substituting Equation 3.50 into Equation 3.51,

$$\left(K_b S_w^2 \alpha_{Tu} + K_d \alpha_{Tu}\right) \frac{\partial T}{\partial t} - \left(K_b S_w^2 n \alpha_{Tw} + K_d \alpha_{Td}\right) \frac{\partial T}{\partial t} = 0 \tag{3.52}$$

Let assume the thermal expansion coefficient for the drained and undrained condition are approximately equal, namely

$$\alpha_{Tu} \approx \alpha_{Td} \tag{3.53}$$

Comparing the coefficient of the first and second term in Equation 3.52 then

$$K_b S_w^2 n \alpha_{Tw} = K_b S_w^2 \alpha_{Tu} \tag{3.54}$$

Substituting Equation 3.53 and Equation 3.54 into Equation 3.51, then the constitutive equation is written as,

$$\frac{\partial \sigma_m}{\partial t} = \left(K_d + K_b S_w^2\right) \frac{\partial \varepsilon_v}{\partial t} - \left(K_d + K_b S_w^2\right) \alpha_{Tu} \frac{\partial T}{\partial t} = K_u \frac{\partial \varepsilon_v}{\partial t} - K_u \alpha_{Tu} \frac{\partial T}{\partial t} \tag{3.55}$$

Accordingly, Equation 3.33 is expressed as,

$$\frac{\partial \sigma_0}{\partial t} = K_b S_w \frac{\partial m}{\partial t} - K_u \alpha_{Tu} \frac{\partial T}{\partial t} - K_d \frac{\partial \varepsilon_{f/t}}{\partial t} \tag{3.56}$$

Also, the continuity equation is written as follow,

$$\frac{\partial m}{\partial t} = \frac{1}{K_b} \frac{\partial u_w}{\partial t} + S_w \alpha_{Tu} \frac{\partial T}{\partial t} - S_w \frac{\partial \varepsilon_v}{\partial t} \tag{3.57}$$

Combining Equation 3.15, 3.16, 3.18, and 3.57, finally, mass conservation equation is as follow,

$$\nabla \cdot \left[-k_w \nabla \left(\frac{u_w}{\rho_w g} + z \right) \right] = \frac{1}{K_b} \frac{\partial u_w}{\partial t} + S_w \alpha_{Tu} \frac{\partial T}{\partial t} - S_w \frac{\partial \varepsilon_v}{\partial t} \qquad 3.58$$

3.1.5 Summary of governing equations

Mass conservation equation

$$\nabla \cdot \left[-k_w \nabla \left(\frac{u_w}{\rho_w g} + z \right) \right] = \frac{1}{K_b} \frac{\partial u_w}{\partial t} + S_w \alpha_{Tu} \frac{\partial T}{\partial t} - S_w \frac{\partial \varepsilon_v}{\partial t} \qquad 3.58$$

Energy conservation equation

$$\left(C_T + L \frac{\partial \theta_i}{\partial T} \right) \frac{\partial T}{\partial t} = \nabla \cdot \left(-\lambda_T \nabla T \right) - C_{Tw} \nabla \cdot \left(\boldsymbol{v}_w T \right) \qquad 3.23$$

Static equilibrium equation

$$\left\{ \frac{1}{2} C_{ijkl} \left(u_{k,l} + u_{l,k} \right) + \sigma_0 \delta_{ij} \right\}_{,j} + \rho g_i = 0 \qquad 3.36$$

$$\frac{\partial \sigma_0}{\partial t} = K_b S_w \frac{\partial m}{\partial t} - K_u \alpha_{Tu} \frac{\partial T}{\partial t} - K_d \frac{\partial \varepsilon_{f/t}}{\partial t} \qquad 3.56$$

3.2 SOIL PROPERTIES FOR UNSATURATED AND FREEZING CONDITION

When the temperature is lowered from room temperature, water freezes at around 0 °C. It is deemed that various changes will occur in the physical properties of the soil undergoing freeze-thaw.

3.2.1 Hydraulic properties

Dependence of permeability on effective stress

For a field-scale simulation, the permeability may vary along the elevation. The saturated water hydraulic conductivity is assumed to depend on the effective stress (Potts and Zdravkovic, 1999).

$$k_s = \left(\sigma'_m\right)^{-a} k_0 \tag{3.59}$$

where k_0 is coefficient of water permeability when mean effective stress equals 0; a is a fitting parameter.

Permeability of unsaturated soil

Regarding relative permeability of water, the van Genuchten-Mualem (VGM) model is adopted (van Genuchten, 1980; Mualem, 1976),

$$k_{wr} = \left(S_e\right)^{1/2}\left[1-\left(1-S_e^{\frac{\lambda}{\lambda-1}}\right)^{\frac{\lambda-1}{\lambda}}\right]^2 \tag{3.60}$$

$$S_e = \left[1+\left(\alpha\psi\right)^{\lambda}\right]^{\frac{1-\lambda}{\lambda}} \tag{3.61}$$

$$S_e = \frac{S_w - S_{rr}}{S_{rs} - S_{rr}} \tag{3.62}$$

where S_e is effective degree of saturation; α, λ are fitting parameters; S_{rr} is residual degree of saturation; S_{rs} is saturated degree of saturation; and ψ is suction which is defined as the difference of pore air pressure u_a and pore-water pressure u_w.

It should be noted that effective degree of saturation represents pore water that is substantially movable, also, stress and deformation of soil due to the movement of pore water is defined by effective degree of saturation. Therefore, effective degree of saturation is assumed to be equivalent to degree of saturation.

$$S_w \cong S_e \tag{3.63}$$

Taking the derivative of effective degree of saturation with respect to suction, then the relation between effective degree of saturation and suction in incremental form can be found.

$$C_H \approx \frac{\partial S_e}{\partial \psi} = -\alpha\left(\lambda - 1\right) S_e^{\frac{\lambda}{\lambda-1}} \left(1 - S_e^{\frac{\lambda}{\lambda-1}}\right)^{\frac{\lambda-1}{\lambda}} \quad 3.64$$

Permeability of freezing soil

It is well known that permeability decreases rapidly when soil is freezing since the formation of pore ice blocks the path of water flow. In general, the permeability of frozen soil is deemed as three orders smaller than unfrozen permeability (Tokoro et al., 2016).

$$k_{wf} = 0.001 k_w \quad 3.65$$

where k_{wf} is coefficient of frozen water permeability.

3.2.2 Thermal properties

The thermal conductivity of soil is assumed not to be affected by freezing. In addition, since it is influenced by degree of saturation, it is possible to input by a function (table form) which is based on experimental data.

$$\lambda_T = f\left(S_w\right) \quad 3.66$$

The heat capacity of soil in the unsaturated state is modeled by following equation. That is, as the moisture content increased, the heat capacity of water also increases.

$$C_T = \left(1 - n\right) C_{Tp} + n S_w C_{Tw} \quad 3.67$$

where C_{Tp} is volumetric heat capacity of soil particles. Similarly, the density and the latent heat of soil also accounts for changes in volumetric water content.

$$\rho = \rho_d + n S_w \rho_w \quad 3.68$$

$$L_f = n S_w L \quad 3.69$$

where ρ_d is dry density of soil; and L_f is total latent heat stored in water.

3.2.3 Mechanical properties

The pore ice bonds the surrounding soil particles, accordingly, the frozen soil becomes stiffer compared with unfrozen one. For the sake of simplicity, a linear relation is given as below

$$E = f\left(S_i\right) = \left(S_i / S_w\right)\left(E_f - E_u\right) + E_u \quad 3.70$$

where E is Young's modulus of soil; E_u is Young's modulus of unfrozen soil; E_f is Young's modulus of frozen soil; and S_i is degree of saturation for ice.

3.3 MODELING OF FREEZE-THAW BEHAVIOR

3.3.1 Treatment of freezing and thawing

The influence of latent heat is modeled. Consider a case where amount of heat per unit time is going to be taken away by the cooling. It is assumed that proportion of b out from Δq is consumed by latent heat L_f and remaining contributes to temperature change. It models heterogeneity of temperature distribution due to difference in heat conductivity between soil skeleton and that of pore water, likely, existence of unfrozen water is also modeled to some extent. This phase change continues for time t and the temperature changes until T_f, and thereafter the influence of latent heat disappears. The temperature change during this time is obtained by the following equation.

$$\Delta T = (1-b)\Delta q / C_T \tag{3.71}$$

The ratio of consumption of latent heat is obtained as follows.

$$b = L_f / (T_f C_T + L_f) \tag{3.72}$$

Therefore, if final freezing temperature T_f can be obtained by experiments, the ratio b can be determined. A graphical interpretation is presented as follow. It should note that a linear variation of latent heat over temperature is applied here, equivalently, the $\partial\theta_i/\partial T$ term in Equation 3.23 is set as a constant (Figure 3.1).

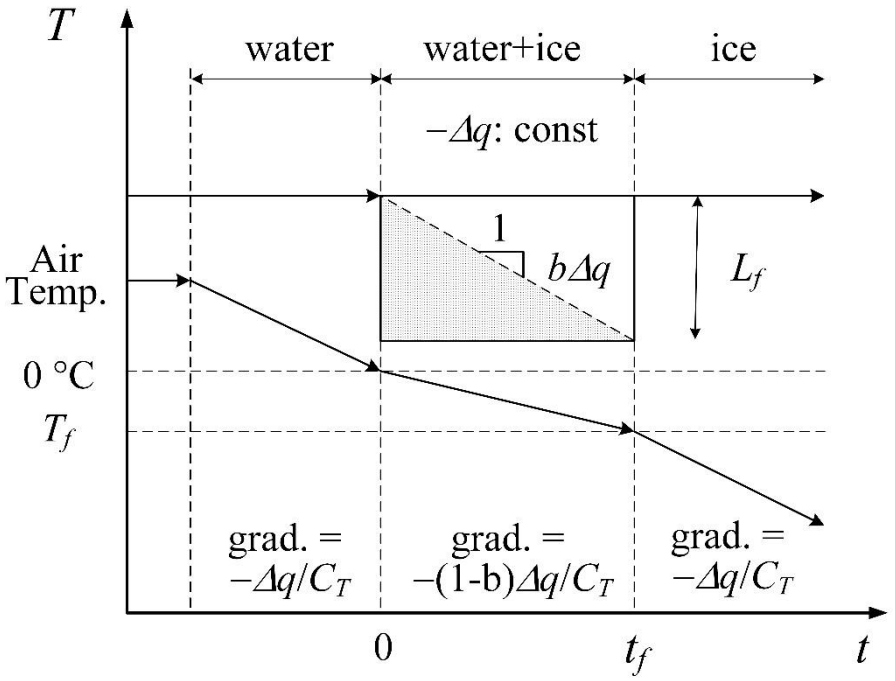

Figure 3.1 Treatment of latent heat during freezing

3.3.2 Modeling of frost heave and thaw settlement

The frost expansion strain (ε_f) and thaw contraction strain (ε_t) were introduced into the coupled THM analysis model. These factors are generated by frost heave and thaw settlement of soils over the temperature range from 0 °C to T_f. Based on results of rost heave test, the frost expansion strain (ε_f) can be expressed as:

$$\varepsilon_f = \kappa_f \left(\frac{\varepsilon_{fmax} S_{w0}}{\varsigma \sigma'_n + 1} + 1.09 m_w \right) \tag{3.73}$$

where ε_{fmax} is maximum frost expansion strain of saturated soil without overburden pressure; S_{w0} is initial degree of saturation; σ'_n is effective stress at the direction of heat flow; and κ_f, ς are fitting parameters.

It is assumed that freezing expansion strain ε_f proportional with the ratio of latent heat consumed to maximum latent heat corresponding ε_{fmax}. Furthermore, when temperature is below 0 °C, it is decided to add amount that inflowing water freezes and expands. In addition, the freezing expansion strain is linearly related to the degree of saturation, and at the same time, it is assumed that it becomes a small value when the effective stress in the heat flow direction becomes large.

When the temperature rises, a phenomenon opposite to the one occurring during temperature drop process generates in soils. According to results of frost heave test, we found that total thaw contraction strain is associated with total stress. For simplicity, thaw contraction strain during the thawing process given as:

$$\varepsilon_t = \omega \varepsilon_f = \left(c + d \ln \sigma_n \right) \varepsilon_f \tag{3.74}$$

where ω is coefficient of thaw contraction; σ_n is total stress at the direction of heat flow; and c and d are fitting parameters.

Figure 3.2 is a schematic of the freeze-thaw process and corresponding frost heave and thaw settlement, along with thermal expansion and contraction. The top two figures show variation of temperature during freeze-thaw process. The change rate of temperature over ranges from 0 °C to T_f is smaller, comparing with unfrozen state with positive temperature and frozen state with a temperature lower than T_f. As mentioned above, some portion of heat budget is consumed by phase change of water-ice fusion, thus frost heave and thaw settlement generate over this specific temperature range that is from 0 °C to T_f, as shown in middle two figures. In addition, the thermal contraction during freezing process and thermal contraction during thawing process are also modeled. Combining these two parts, the volumetric change induced by temperature change is illustrated in bottom two figures.

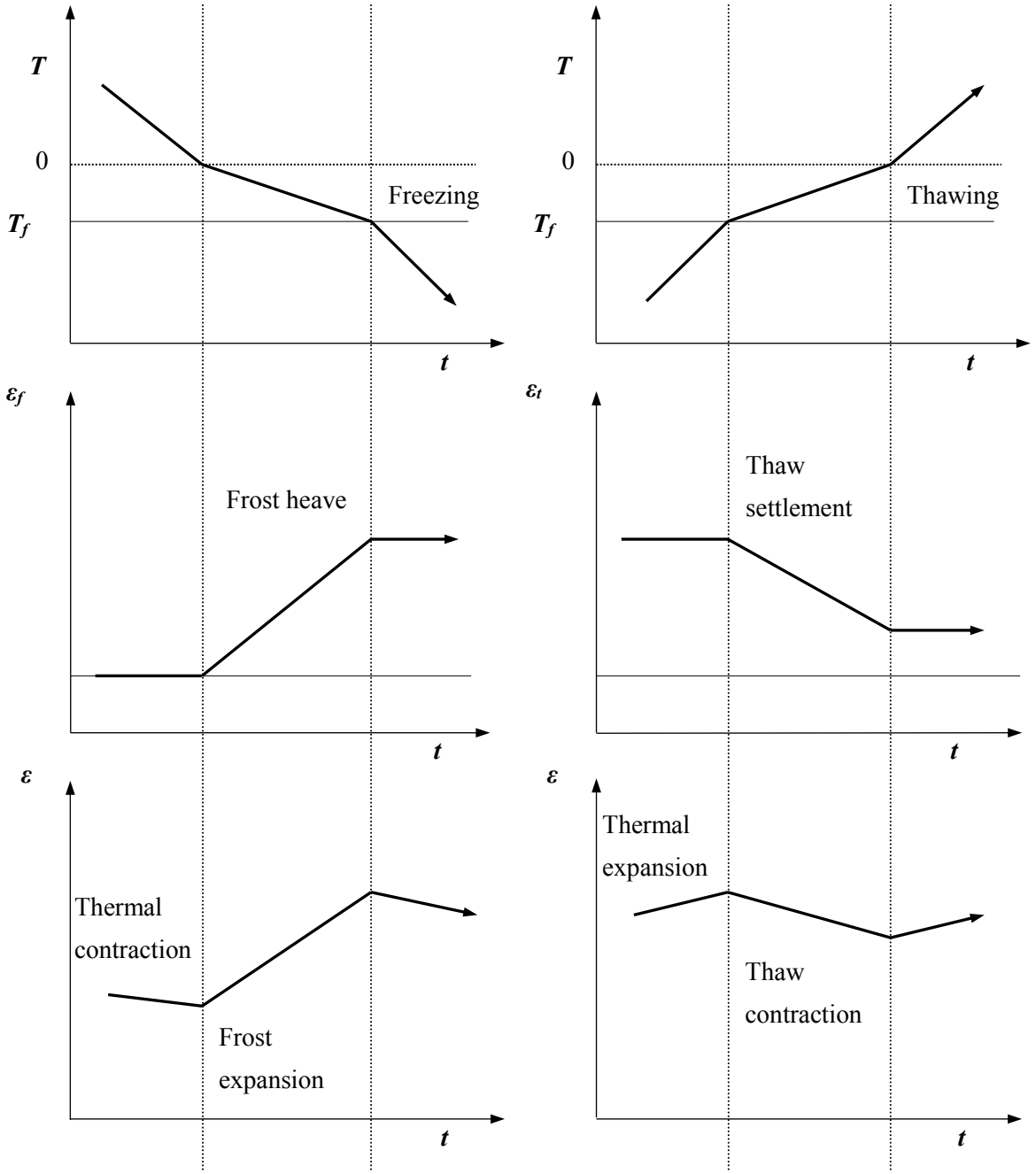

Figure 3.2 Modeling volume change during the freeze-thaw process

3.4 SOLVING THE GOVERNING EQUATION

3.4.1 Differentiation of time

In solving governing equations, approximating the time derivative contained in the equation by difference

$$\frac{\partial}{\partial t} = \frac{\Delta}{\Delta t} \tag{3.75}$$

Next, the second term on the left side in the equilibrium Equation 3.36 is treated as a known term.

$$\left\{ \frac{1}{2} C_{ijkl} \left(\Delta u_{k,l} + \Delta u_{l,k} \right)^{t+1} + \Delta \sigma_0^t \delta_{ij} \right\}_{,j} + \rho g_i = 0 \tag{3.76}$$

Applying Equation 3.56 on a given time step t,

$$\Delta \sigma_0^t = K_b S_w \Delta m^t - K_u \alpha_{Tu} \Delta T^t - K_d \Delta \varepsilon_{f/t}^t \tag{3.77}$$

By solving this, the increment of deformation, stress, strain, etc. at t+1 is determined. Each term included in Equation 3.77 is obtained as follows using the value at time t in consideration of the Equation 3.15, 3.16 and 3.18.

$$\Delta m^t = \frac{1}{\rho_w} \nabla \cdot \left(\rho_w \boldsymbol{v}_w^t \right) \Delta t \tag{3.78}$$

$$\boldsymbol{v}_w^t = -k_w \nabla \left(\frac{u_w^t}{\rho_w g} - z \right) \tag{3.79}$$

If the increment of volumetric strain is obtained by solving Equation 3.76, the increment of pore water pressure is obtained by using the following equation derived from Equation 3.57.

$$\Delta u_w^{t+1} = K_b S_w \Delta \varepsilon_v^{t+1} - K_b S_w \alpha_{Tu} \Delta T^t + K_b \Delta m^t \tag{3.80}$$

By repeating this operation for each increment of time, a solution is sought.

3.4.2 Calculation of displacement

The best-known method for approximating Equation 3.76 under necessary boundary conditions is the finite element method. Since the finite element method is detailed in numerous documents, it is merely to show the finite element equation finally obtained here. We will use the commonly used symbols to explain the outline.

$$\sum_{e=1}^{E} \left(\int [B]^T [C_u][B] \{\Delta u\} dV_e \right) - \sum_{e=1}^{E} \left(\int [B]^T \{\Delta \sigma_0\} dV_e \right) = 0 \tag{3.81}$$

$$[B] = [\partial][N] \tag{3.82}$$

where $\{\Delta\sigma_0\}$ corresponds to the second term on the left side of Equation 3.76, the stress vector in two-dimensional problem.

$$\{\Delta\sigma_0\} = \left(K_b S_w \Delta m^t - K_u \alpha_{Tu} \Delta T^t - K_d \Delta\varepsilon^t_{f/t}\right)\{110\}^T \tag{3.83}$$

Stress vector is given as.

$$\{\sigma\} = \{\sigma_x \sigma_y \tau_{xy}\}^T \tag{3.84}$$

Equation 3.81 can be written as follows.

$$[K_u]\{\Delta u\} - \{\Delta F\} = 0 \tag{3.85}$$

Here, $\{K_u\}$ is a global stiffness matrix. Therefore, the displacement can be obtained by setting the second term on the right side of Equation 3.85 as a known load term $\{\Delta F\}$.

From the strain obtained, pore water pressure change of element is obtained based on Equation 3.80, and it takes a constant value within the element as well as the strain.

3.4.3 Calculation of change of water and heat

For the calculation of the displacement, it is necessary to obtain mass change Δm in each element. On the other hand, as shown in the previous section, pore water pressure is determined as a constant value in the element, and the second derivative in Equation 3.23 cannot be performed within an element.

Therefore, using the above-mentioned interpolation function [N], the pore pressure gradient within the element is assumed, and the average value of the gradient of all the elements surrounding one node is obtained for each node, which is further differentiated to calculate mass change. However, it is assumed that element division is the same as used for calculation of displacement.
Hereinafter, this technique will be described by taking a two-dimensional problem as an example.

Let's consider the case where the two elements are in contact with each other on the side l_a (Figure 3.3). In each element, it is assumed that there is a pressure difference of ϕ at the center of gravity and node O on the side l_a, and the pressure gradient in the x' direction (normal direction of the side l_a) is determined as follows.

$$\frac{\Delta\phi}{\Delta x} = \frac{\phi_1}{x_1'}\cos\theta_a \tag{3.86}$$

In addition, the pressure gradient is considered constant within a triangle shown by oblique lines. For two elements (1 and 2) in contact with the side l_a, the pressure gradient is obtained with each element. The area of the triangle indicated by the shaded area of each element is averaged using

the area as a weight, and the obtained pressure gradient is regarded as the value at the node *O* and *P*.

$$\left(\frac{\Delta\phi}{\Delta x}\right)_O = \left(\frac{\Delta\phi}{\Delta x}\right)_P = \frac{\frac{A_1}{3}\frac{\phi_1}{x_1'}\cos\theta_a + \frac{A_2}{3}\frac{\phi_2}{x_1'}\cos(-\theta_a)}{\frac{A_1}{3}+\frac{A_2}{3}} \tag{3.87}$$

where θ_a is an angle obtained by measuring the normal of the side l_a from the reference coordinate system.

$$\frac{A_1}{3} = \frac{1}{2} l_a x_1' \tag{3.88}$$

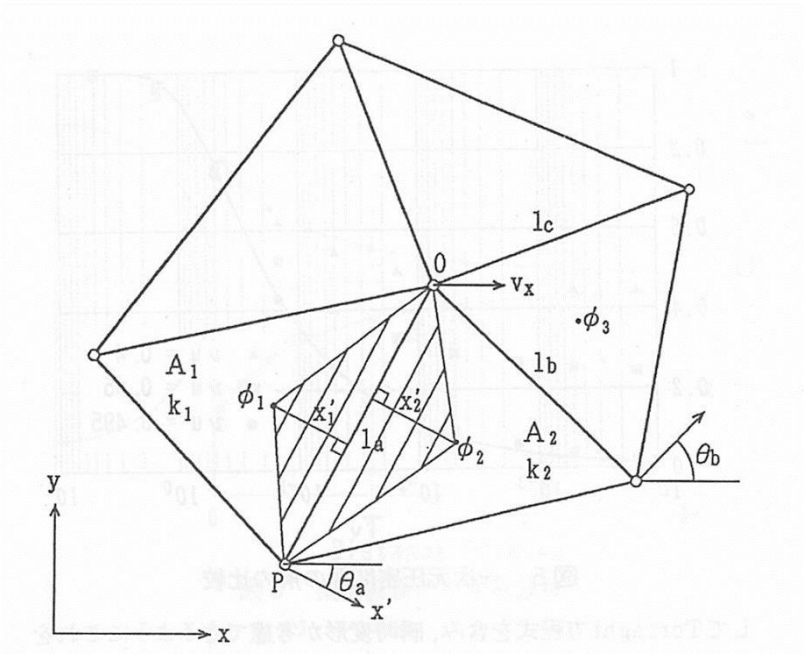

Figure 3.3 Element division and calculation of flow velocity

Considering Equation 3.87, then Equation 3.88 is written as,

$$\left(\frac{\Delta\phi}{\Delta x}\right)_O = \frac{\phi_1 - \phi_2}{x_1' + x_2'}\cos\theta_a \tag{3.89}$$

In this method, the pressure difference (ϕ_1-ϕ_2) of the two elements is eventually divided by the distance in the normal direction of the side l_a to regard it as a pressure gradient, and this is taken as the value of the node on the side l_a. Therefore, this method can be regarded as a type of difference method. However, since the distance used to obtain the pressure gradient is not the distance connecting the points (the center of gravity of the element) that define the pore water pressure, but the distance in the normal direction of the side l_a, this is different from the difference method. In addition, if the shape of each element largely deviates from the equilateral triangle,

the difference between these two distances becomes large, which is considered to degrade calculation accuracy.

For the pressure gradient at the node O, the pressure gradient is similarly obtained for all the elements surrounding it, and this is taken as the average of the area of each element as a weight.

$$\left(\frac{\Delta\phi}{\Delta x}\right)_O = \frac{\frac{1}{2}l_a\phi_1\cos\theta_a + \frac{1}{2}l_a\phi_2\cos\left(-\theta_a\right) + \frac{1}{2}l_b\phi_2\cos\theta_b + \ldots}{\frac{A_1}{3} + \frac{A_2}{3} + \frac{A_3}{3} + \ldots} \tag{3.90}$$

The flow velocity at node O can be obtained by multiplying the pressure gradient by the permeability coefficient. Here, for the hydraulic conductivity coefficient, the value of the element surrounding the node O is also averaged by weighting each area.

$$\left(v_x\right)_O = \frac{\bar{k}_w}{\rho_w g}\left(\frac{\Delta\phi}{\Delta x}\right)_O \tag{3.91}$$

$$\frac{1}{\bar{k}_w} = \frac{\frac{1}{k_1}A_1 + \frac{1}{k_2}A_2 + \frac{1}{k_3}A_3 + \ldots}{A_1 + A_2 + A_3 + \ldots} \tag{3.92}$$

Finally, the following equation is obtained as the flow velocity at the node O.

$$\left(v_x\right)_O = \frac{1}{\rho_w g}\frac{\frac{1}{2}l_a\phi_1\cos\theta_a + \frac{1}{2}l_a\phi_2\cos\left(-\theta_a\right) + \frac{1}{2}l_b\phi_2\cos\theta_b + \ldots}{\frac{A_1}{3k_1} + \frac{A_2}{3k_2} + \frac{A_3}{3k_3} + \ldots} \tag{3.93}$$

When pressure is applied at the boundary as shown in Figure 3.4, the pressure gradient is obtained by the same method with the value at the side l as ϕ^s.

$$\frac{\Delta\phi}{\Delta x} = \frac{\phi - \phi^s}{x'}\cos\theta \tag{3.94}$$

Therefore, the flow velocity at the node O is as follows.

$$\left(v_x\right)_O = \frac{1}{\rho_w g}\frac{\frac{1}{2}l\phi\cos\theta + \frac{1}{2}l\phi^s\cos\left(-\theta\right)}{\frac{A}{3k}} \tag{3.95}$$

That is, if the side sharing node is a boundary, the weight of the numerator of Equation 3.91 is multiplied by the pressure of the boundary by 1/2 of the side length (the length projected on each coordinate axis). In addition, when the flow velocity v^s is given at the boundary,

$$\left(v_x\right)_O = v_x^s \tag{3.96}$$

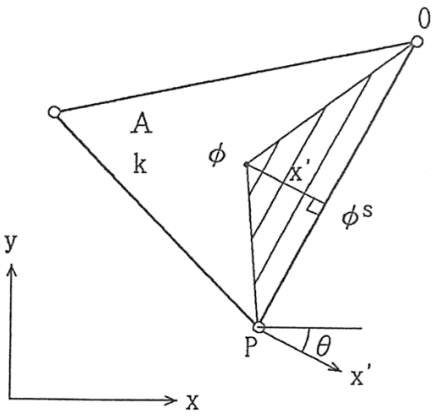

Figure 3.4 Boundary elements and boundary conditions

In this method, we consider the interpolation function (first-order function) in the finite element method as the weight of the pressure gradient, and by integrating it in the target region, this approximation value is obtained, from which the flow velocity at the node is obtained.

After the flow velocity vector is obtained at each node, the flow velocity distribution in the element is assumed again using the interpolation function, and the approximate value of the mass change Δm is obtained.

$$\Delta m = \frac{\partial v_i}{\partial x_i} \Delta t \tag{3.97}$$

By using the flow velocity $\{v\}$ at the node and the interpolation function $[N]$.

$$\Delta m = -\frac{\partial}{\partial x_i} [N] \{v_i\} \Delta t = -[B_i] \{v_i\} \Delta t \tag{3.98}$$

3.5 FLOW CHART OF COMPUTATION

The flowchart of the created analysis program is shown in the figure below.

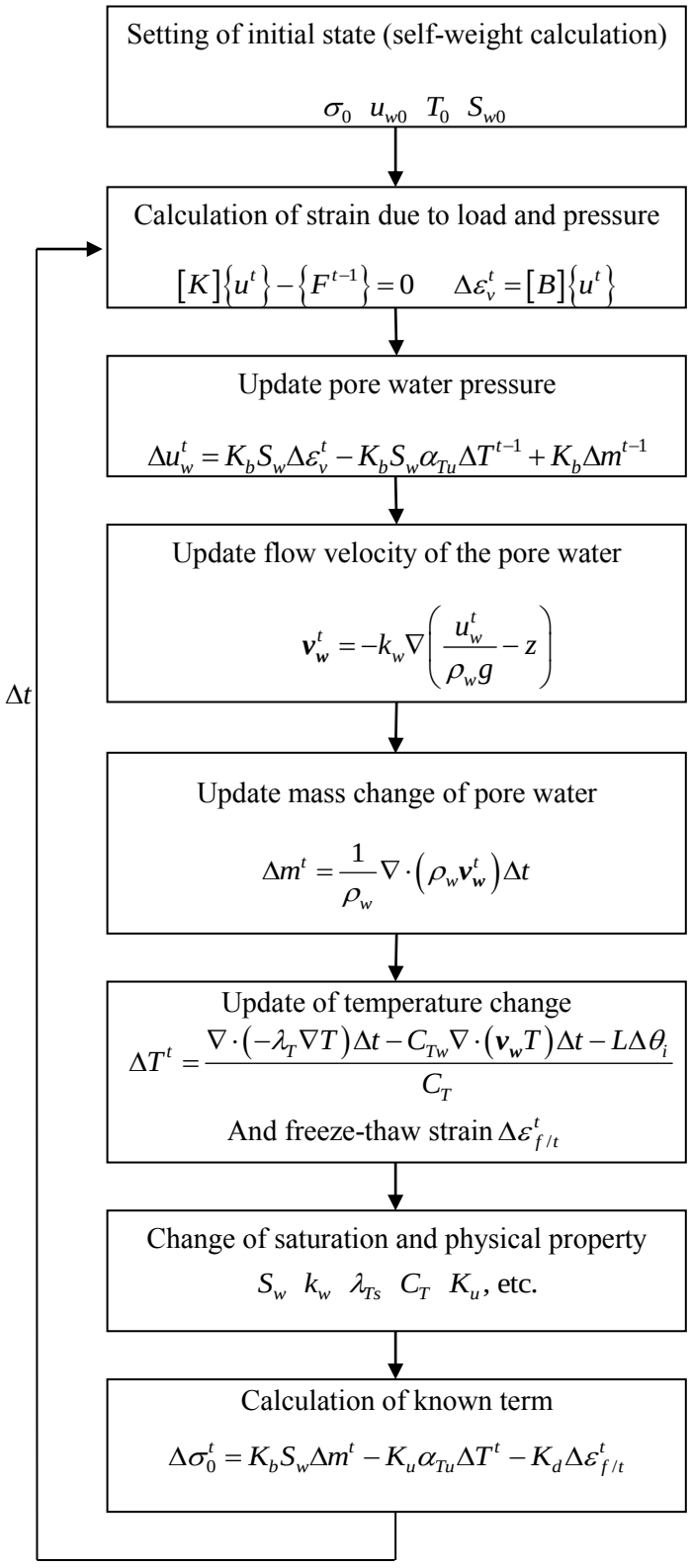

Figure 3.5 Flowchart of THM analysis

4 MODEL VALIDATION AND APPLICATION

4.1 MODEL VALIDATION

4.1.1 Simulation of frost heave test

The validity of the developed THM analysis is examined using a series of simulated frost heave tests (Ishikawa et al., 2015). The experimental apparatus for frost heave test is presented in Figure 4.1. The test procedure follows the standard "Test Method for Frost Heave Prediction of Soils" (JGS 0171-2003) of the Japanese Geotechnical Society (2015).

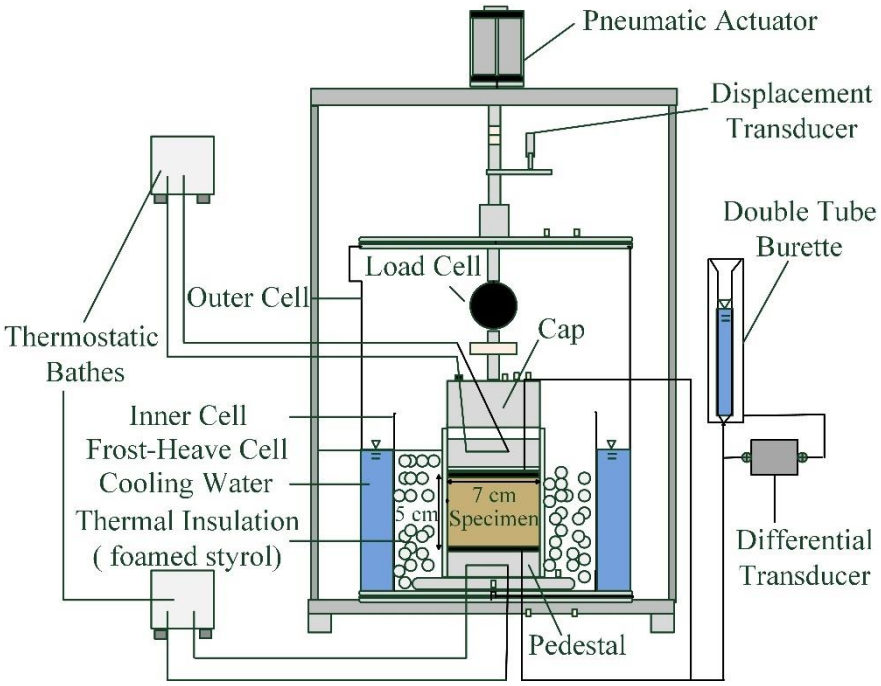

Figure 4.1 Experimental apparatus for frost heave test

Figure 4.2 shows the size and boundary conditions of a two-dimensional FE model under the plane-strain condition, together with the element mesh. The side boundaries are given as impervious and thermal insulation boundary to simulate one-dimensional frost heave test. The soil specimen is frozen from bottom-up, while the water can be absorbed into specimen from the top end to feed the growth of ice lens. The boundaries considered here are in accordance with the actual test conditions.

The simulated frost heave test for a frost-susceptible soil was performed as follows,

1. Initial stability analysis: the average initial degree of saturation (S_{w0}) of a test specimen was set at the intended value, and the temperatures of all elements were set at 0.8 °C. Gravitational acceleration of 9.8 m/s^2 was then applied, and the prescribed overburden pressure (σ_{ob}) loaded on

the top surface for one-dimensional consolidation of the test specimen. Note that S_{w0} = 100%; σ_a = 2.5, 5.0, 10.0, 50.0, 100.0 kPa.

2. Freeze process analysis: the test specimen was frozen from below by decreasing the temperature of the base surface at a given cooling rate (U) while keeping the top surface at 0.8 °C. Note that U = 0.2, 0.4, 0.8 °C/h.

Thaw process analysis: the test specimen was thawed from both ends by rapidly increasing the temperatures of the top and base surfaces to 5 °C and keeping them at that temperature for 20 hours.

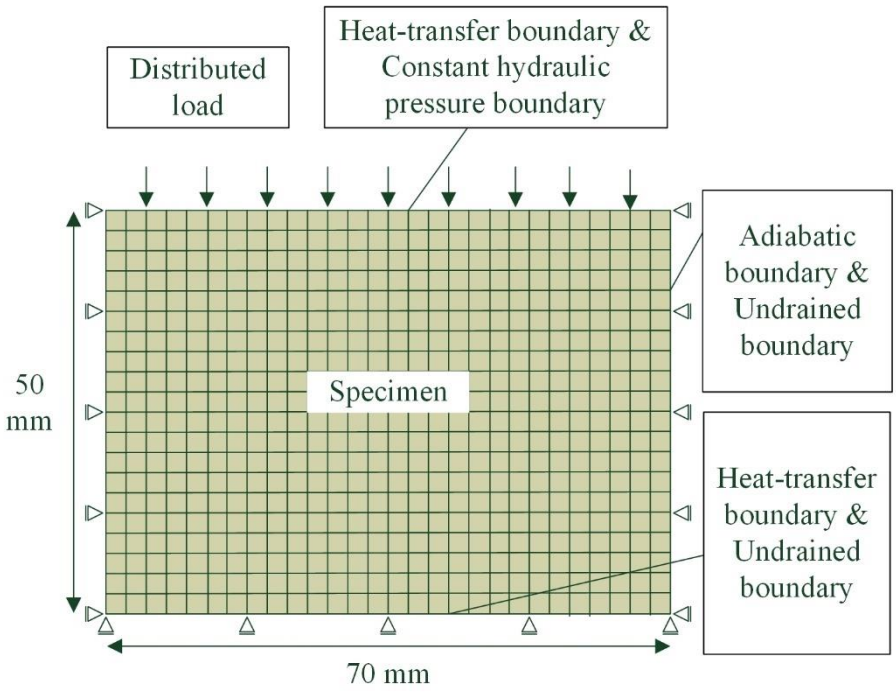

Figure 4.2 Simulation boundary conditions for frost heave test

4.1.2 Determination of inputs

The test material is a high frost-susceptible, weathered, and cohesive volcanic soil (Touryo soil) consisting of 21% silt, 26% clay, and 53% sand. The coefficient in Equation 3.59 is obtained through consolidation test data which describes the influence of effective stress level on the permeability of water.

$$k_s = \left(\sigma'_m\right)^{-a} k_0 \qquad 3.59$$

VG parameters in Equation 3.61 and 3.62 are fitted based on water retention test data (Figure 4.4)

$$S_e = \left[1+\left(\alpha\psi\right)^{\lambda}\right]^{\frac{1-\lambda}{\lambda}} \qquad 3.61$$

$$S_e = \frac{S_w - S_{rr}}{S_{rs} - S_{rr}} \qquad 3.62$$

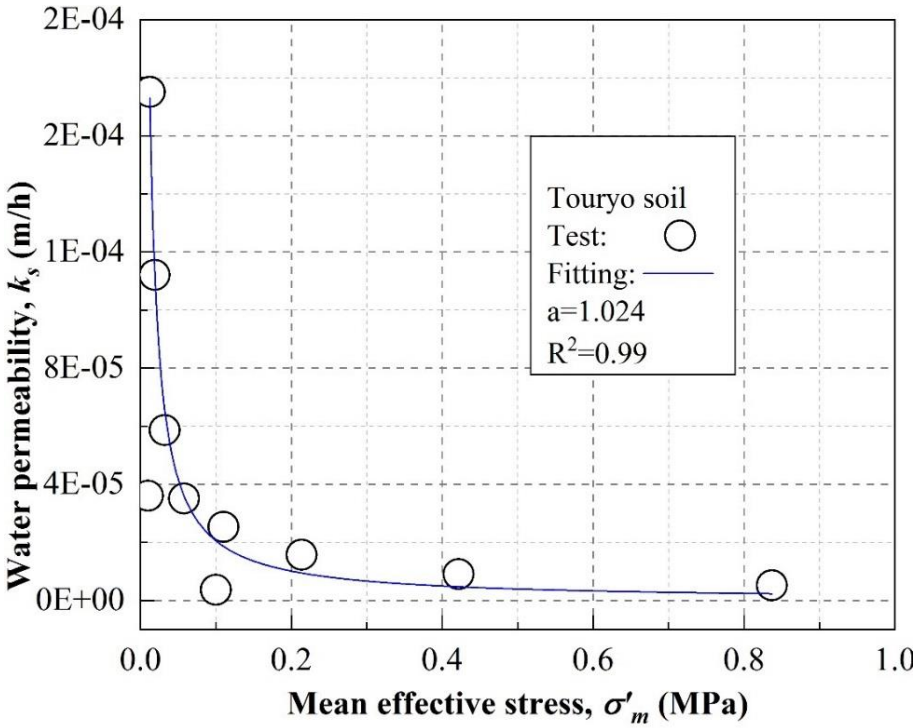

Figure 4.3 Dependence of permeability on effective stress

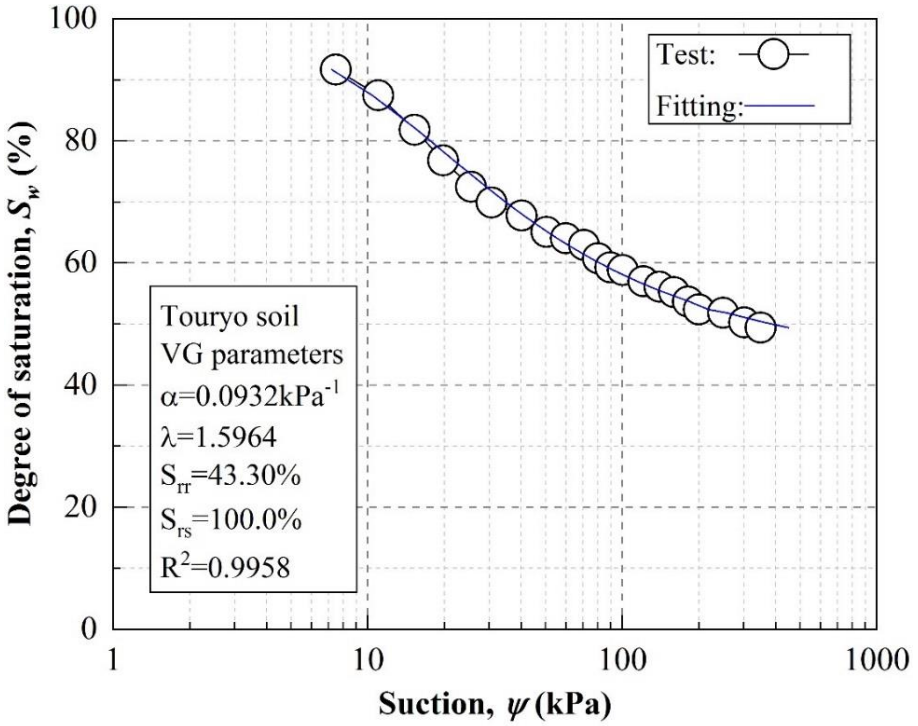

Figure 4.4 SWCC of Touryo soil

The constants related to frost heave and thaw settlement in Equation 3.73 and 3.74 were obtained through parameter fitting based on data from the frost heave test, as shown in Figure 4.5 and Figure 4.6.

$$\varepsilon_f = \kappa\left(\frac{\varepsilon_{fmax} S_{w0}}{\varsigma\sigma_n' + 1} + 1.09 m_w\right) \quad 3.73$$

$$\varepsilon_t = \omega\varepsilon_f = (c + d\ln\sigma_n)\varepsilon_f \quad 3.74$$

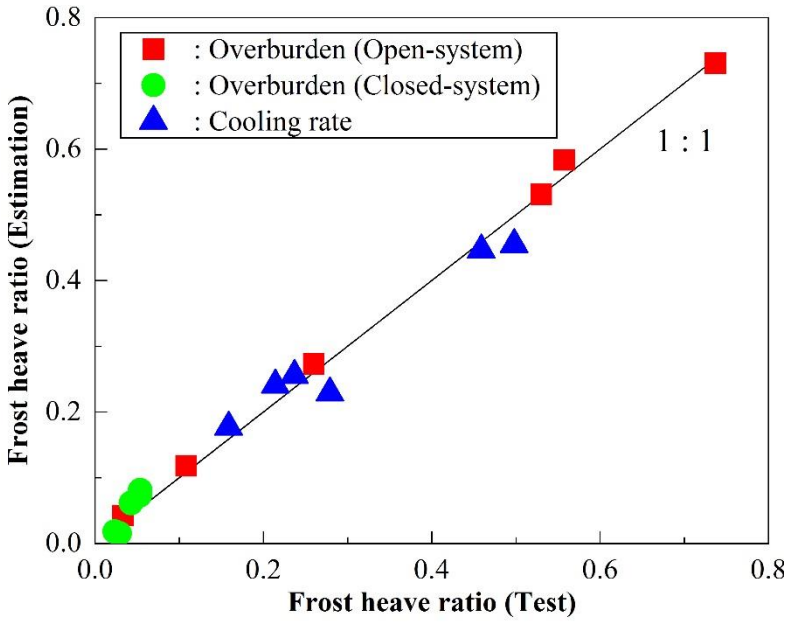

Figure 4.5 Evaluation of fitting frost heave ratio

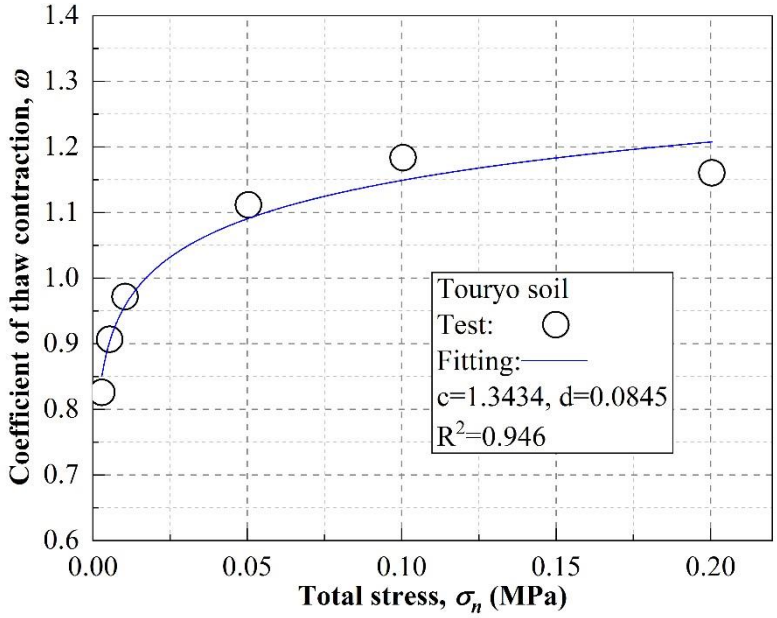

Figure 4.6 Fitting of thaw contraction coefficient

Saturated water hydraulic conductivity (k_s) was set based on the permeability test results. The other parameters were given by referring to the results of various laboratory element tests for Touryo soil under similar experimental conditions, and the common values employed in previous studies. The input parameters in this study are listed in Table 4.1.

Table 4.1 Input parameters in frost-heave test analysis of Touryo soil

Parameters	Values
Dry density of soil (ρ_d) kg/m^3	1400
Porosity (n)	0.450
Final freezing temperature (T_f) °C	-0.2
Thermal conductivity of soil (λ_T) W/m°C	1.610
Volumetric heat capacity of soil particles (C_{Tp}) J/m^3°C	1.8E+6
van Genuchten-Mualem fitting parameter (α) 1/MPa	93.20
van Genuchten-Mualem fitting parameter (λ)	1.596
Saturated degree of saturation (S_{rs}) %	100.0
Residual degree of saturation (S_{rr}) %	43.30
Saturated water hydraulic conductivity (k_s) m/s	1.0E-8
Saturated water hydraulic conductivity fitting parameter (a)	1.024
Thermal expansion coefficient under undrained condition (α_{Tu}) 1/°C	1.2E-5
Young's modulus of soil (E) MPa	40.0
Poisson's ratio (υ)	0.40
Frost heave fitting parameter (κ_f)	0.749
Maximum frost expansion strain (ε_{fmax})	0.306
Frost heave fitting parameter (ς) 1/MPa	28.64
Thaw settlement fitting parameter (c)	1.343
Thaw settlement fitting parameter (d) 1/MPa	0.085

4.1.3 Results and discussions

The dependency of freeze-thaw behavior on various factors is presented in Figure 4.7-Figure 4.9. Under the same experimental conditions, both the axial strain and the water absorption and drainage in the freeze-thaw process predicted by the THM analysis match well with actual test results (Figure 4.7). Frost heave is generated by the absorption water, which demonstrates how water migration towards the freezing front plays a significant role in volumetric expansion during the freezing process. However, analysis overestimates frost heave amount while simulated water drainage is greater than test one during the thawing process.

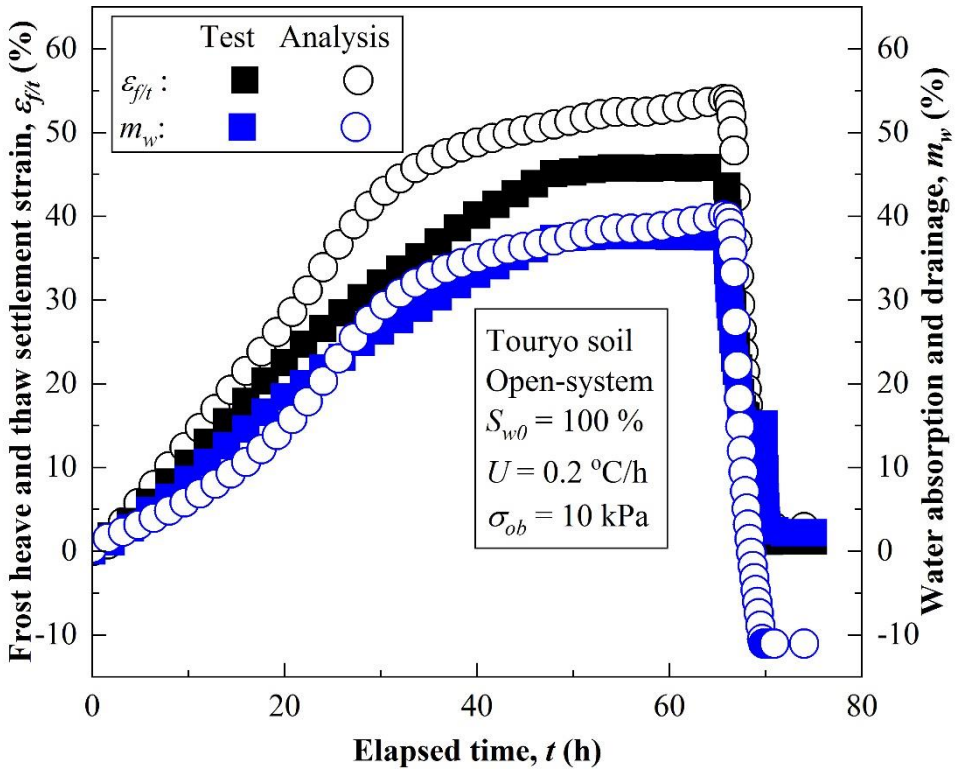

Figure 4.7 Influence of water supply on frost heave

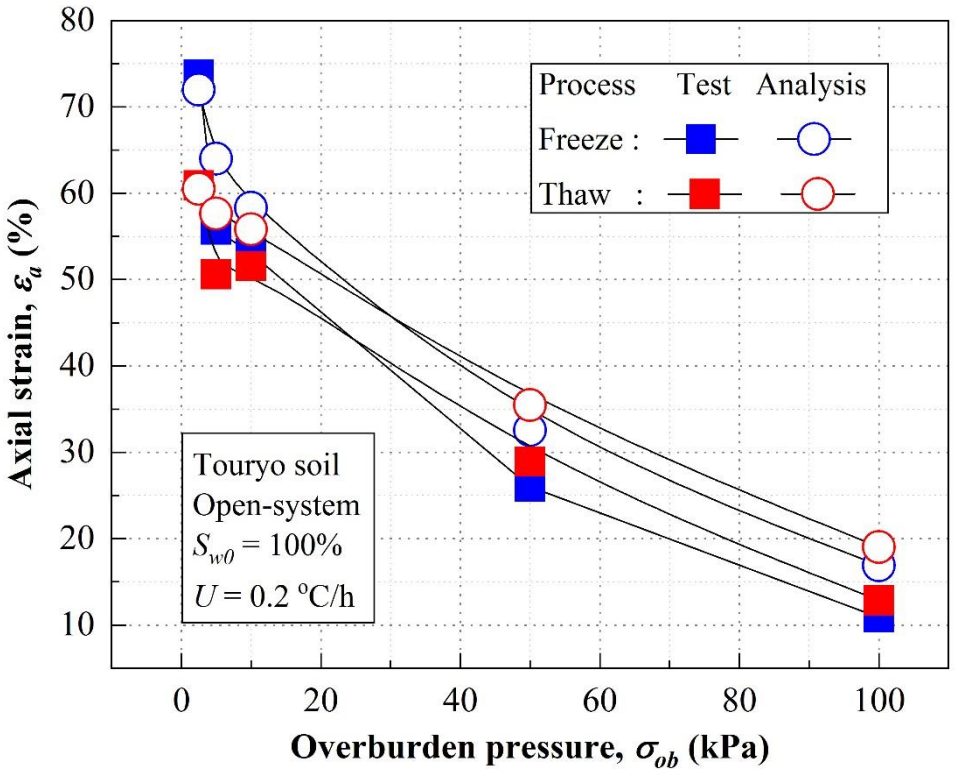

Figure 4.8 Influence of overburden pressure on frost heave

The influence of overburden pressure (σ_{ob}) is depicted in Figure 4.8. As overburden pressure increases, axial strain decreases. It is harder with higher overburden pressure for segregation ice to separate the closely packed soil skeleton and form a new ice lens than it is with lower overburden pressure. For low levels of overburden pressure (within 10 kPa), the thaw settlement is less than frost heave. Conversely, the thaw settlement is greater than frost heave for higher levels of overburden pressure (10-100 kPa). However, the model tends to always overestimate frost heave amount for open-system case.

For the cooling rate (U), with a rapid lowering of temperature and advance of the freezing front the transportation of water towards the frost line is reduced, induced by decreased permeability in the freezing soil. Consequently, the soil cooled more rapidly exhibits smaller frost heave. However, the model fails to reproduce the influence of cooling rate on frost heave (Figure 4.9).

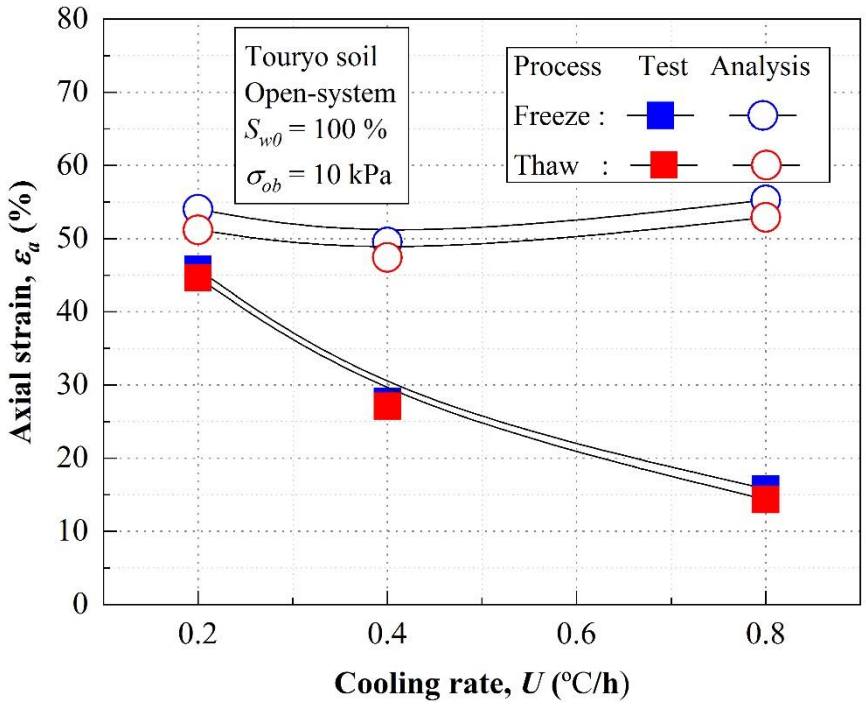

Figure 4.9 Influence of cooling rate on frost heave

4.1.4 Remarks

The model generally enables to predict freeze-thaw behavior of saturated soil, however, limitations remain. The model overestimates frost heave amount for open-system case and fails to predict influence of cooling rate on frost heave. Some uncertainty is that determination of final freezing temperature empirically depends on user experience. There are also some drawbacks not well-considered like phase transition of intake water, influence of ice content on soil properties. Most importantly, validity of model for unsaturated soil is not examined.

4.2 THE FREEZE-THAW BEHAVIOR OF PAVEMENT AROUND A BOX CULVERT

4.2.1 Problem statement

In 2001, weather in Hokkaido was severely cold. The annual freezing index far exceeded the average of the previous ten years (761 °C·day) and reached 1003 °C·day. Uneven frost heave of pavement and cracks in the sidewall of culverts due to volume expansion of frost-susceptible backfill were observed. A field monitoring of this pavement was conducted by Toyota et al. (2002). Thermometers and strain gauges were installed in boreholes beside the culvert and on reinforcements in the sidewall, respectively (Figure 4.10). The backfill around culvert was classified as silt soil with a high liquid limit (MH), comprising 7.2% gravel, 30.3% sand, 35.0% silt, and 27.5% clay-size particles, exhibiting high frost susceptibility. Its water content, plastic limit and liquid limit ranges were 31.0-64.0%, 26.4-37.4%, and 53.3-71.6%, respectively.

The input material parameters are summarized in Table 4.2. Asphalt mixture, concrete, and extruded polystyrene (XPS) are non-frost susceptible materials; while C-40, sand, and C-80 have low frost susceptibility. For simplicity, the frost heave induced by the materials mentioned above is neglected. Touryo soil and backfill have a similar fine particle size distribution. Hence it is reasonable to employ Touryo soil as a substitute of frost-susceptible in-situ soil.

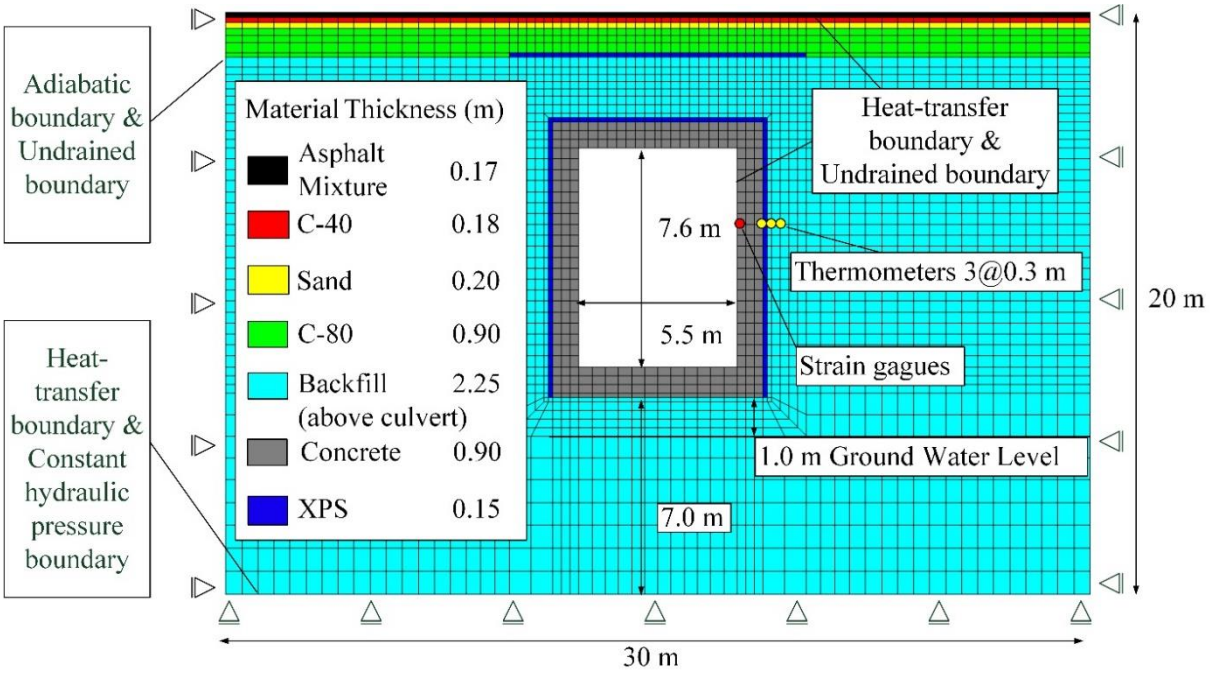

Figure 4.10 Box culvert profile and finite element mesh

Table 4.2 Input parameters in box culvert analysis

Parameters	Touryo	C-40	Sand	C-80	Asphalt	Concrete	XPS
Dry density of soil (ρ_d) kg/m^3	1400	2000	1600	2000	2200	2300	25
Porosity (n)	0.450	0.300	0.250	0.200	0.030	0.050	0.020
Final freezing temperature (T_f) °C	-0.2	-0.2	-0.2	-0.2	-0.2	-0.2	-0.2
Thermal conductivity of soil (λ_T) W/m°C	1.61	2.51	1.97	2.13	1.45	0.94	0.03
Volumetric heat capacity of soil particles (C_{Tp}) J/m^3°C	1.8E+6	1.8E+6	1.9E+6	1.7E+6	1.8E+6	2.0E+6	4.5E+4
van Genuchten-Mualem fitting parameter (α) 1/MPa	93.20	846.6	846.6	846.6	na	na	na
van Genuchten-Mualem fitting parameter (λ)	1.596	1.360	1.360	1.360	na	na	na
Saturated degree of saturation (S_{rs}) %	100.0	94.93	94.93	94.93	na	na	na
Residual degree of saturation (S_{rr}) %	43.30	23.94	23.94	23.94	na	na	na
Saturated water hydraulic conductivity (k_s) m/s	1.0E-8	1.0E-5	1.0E-5	1.0E-5	1.0E-10	1.0E-10	1.0E-10
Fitting parameter (a)	1.024	1.024	1.024	1.024	na	na	na
Thermal expansion coefficient under undrained condition (α_{Tu}) 1/°C	1.2E-5	1.0E-5	1.0E-5	1.0E-5	3.0E-5	1.0E-5	5.0E-5
Young's modulus (E) MPa	40	300	200	40	10000	21700	25
Poisson's ratio (υ)	0.40	0.35	0.35	0.40	0.35	0.20	0.10
Fitting parameter (κ_f)	0.749	na	na	na	na	na	na
Maximum frost expansion strain (ε_{fmax})	0.306	na	na	na	na	na	na
Fitting parameter (ς) 1/MPa	28.64	na	na	na	na	na	na
Fitting parameter (c)	1.343	na	na	na	na	na	na
Fitting parameter (d) 1/MPa	0.085	na	na	na	na	na	na

4.2.2 Initial and boundary conditions

Figure 4.10 also shows the finite element mesh, where relatively fine meshing around the culvert was given to enable precise reproduction of frost heave.

Based on long-term air temperature monitoring data, the surface temperature condition of pavement and culvert was simplified to sinusoidal variation and given as:

$$T = T_m + A \cdot \sin\left(\frac{2\pi t}{p} + \varphi\right) + \Delta T \qquad 4.1$$

where T_m is mean annual temperature; A is surface temperature amplitude; t is time (day); p is a corresponding period, 365 days; and φ is an initial phase.

ΔT is the increment of temperature induced by boundary layer, considered to be 3 °C for pavement surface and 0 °C for culvert surface. At the bottom, the temperature is expressed as (Andersland and Ladanyi, 2004):

$$T = T_m + A \cdot \exp(-z\sqrt{\frac{\pi}{\alpha_u p}}) \cdot \sin\left(\frac{2\pi t}{p} + \varphi - z\sqrt{\frac{\pi}{\alpha_u p}}\right) \qquad 4.2$$

where z is depth below the air temperature boundary, 7 m; and α_u is thermal diffusivity, 4.89E-7 W/m^2°C.

Heat flow from the earth's interior is assumed to be negligible. The pavement structure was simulated as follows:

1. Initial stability analysis: initial temperature distribution was obtained through a ten years heat transfer governing by 4.1 and 4.2, where T_m was 6.4 °C and A was 15.6 °C obtained from meteorological data from 1990 to 2000. Matric suction was linearly distributed along the direction of elevation. The geostatic stress field was gained by assuming the lateral pressure coefficient as 0.5.

2. Freeze and thaw process analysis: a lower temperature was applied to simulate severely cold weather, where T_m and A were given as 5.5 °C and 16.3 °C, respectively (in 2001). The freezing process was performed for 3000 hours, referring to observed air temperature and freezing index. Then, 3000 hours of the thawing process was performed until frozen soil thawed completely.

4.2.3 Results and discussions

Temperature Distribution

Figure 4.11 indicates the time histories of simulated and measured temperatures of the backfill immediately behind the culvert. When the air temperature is below 0 °C, the temperature of all

points of measurement gradually drops. However, the temperature rises as the distance of the point of measurement from the back of the culvert increases. During the entire freezing process, the temperature of the 0.6 m location was always above 0 °C, while the 0.3 m location drops below 0 °C. The thickness of the culvert sidewalls is 0.9 m. Accordingly, the depth of frost penetration from the inner surface of culvert ranges between 1.2-1.5 m which is deeper than design value (1.2 m). The overall behavior of the simulated temperature change agrees well with the measured one. Considering the difference between backfill and Touryo soil, such simulated results are reasonable, and this model can be used to predict temperature distributions around the culvert.

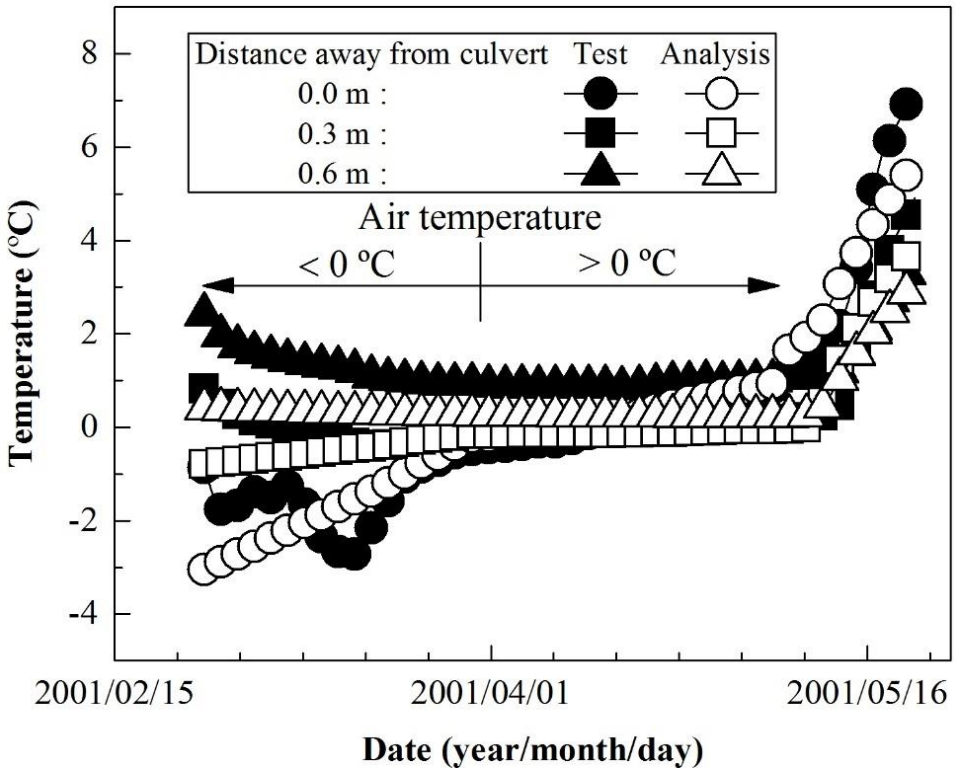

Figure 4.11 Comparison of temperature variation at the back of culvert

Figure 4.12 illustrates the initial temperature distribution. The temperature distribution right before the thawing process was begun as shown in Figure 4.13. The 0 °C isotherm penetrates deep into frost susceptible soil around the culvert. The frost penetrated much deeper in the subsurface layer right above the culvert than it did in the zone far away from the culvert. For the adjacent area, when air temperature drops and cooling energy flows into the pavement, heat flow from deeper soil delays advance of the freezing front. For the pavement located above the culvert, cooling will occur from the upper pavement surface and the lower inner surface of the culvert, which is different from that in the adjacent pavement.

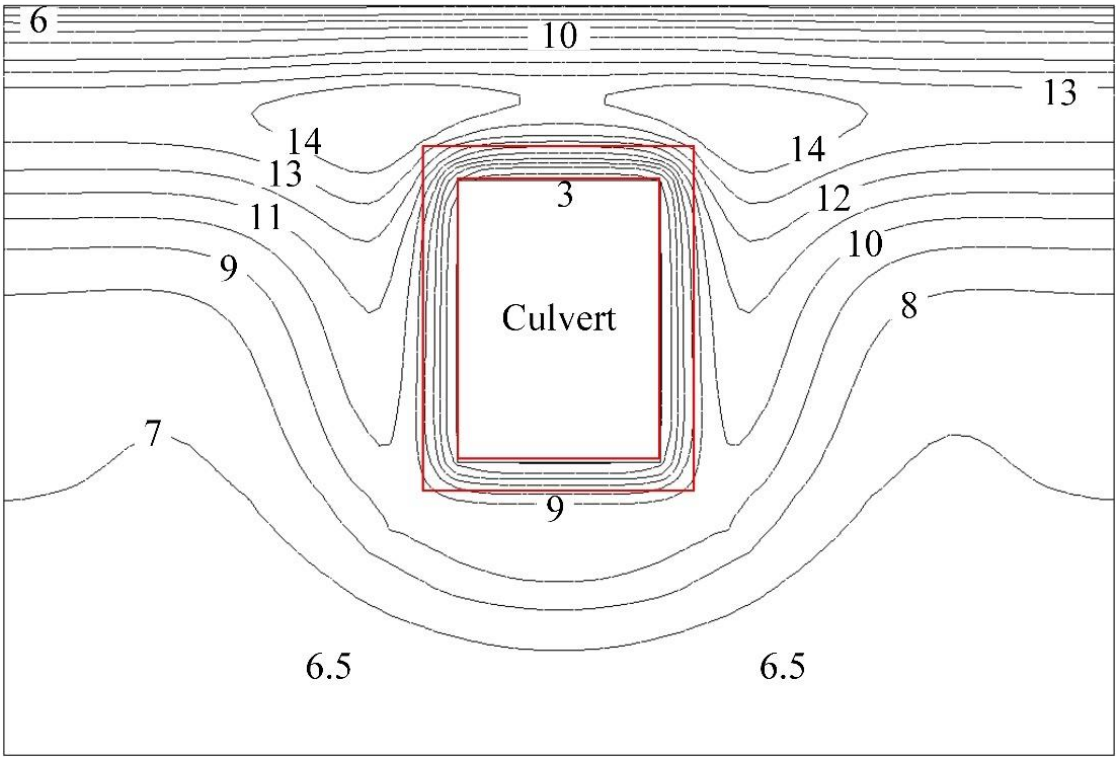

Figure 4.12 Temperature distribution at the start of freeze process

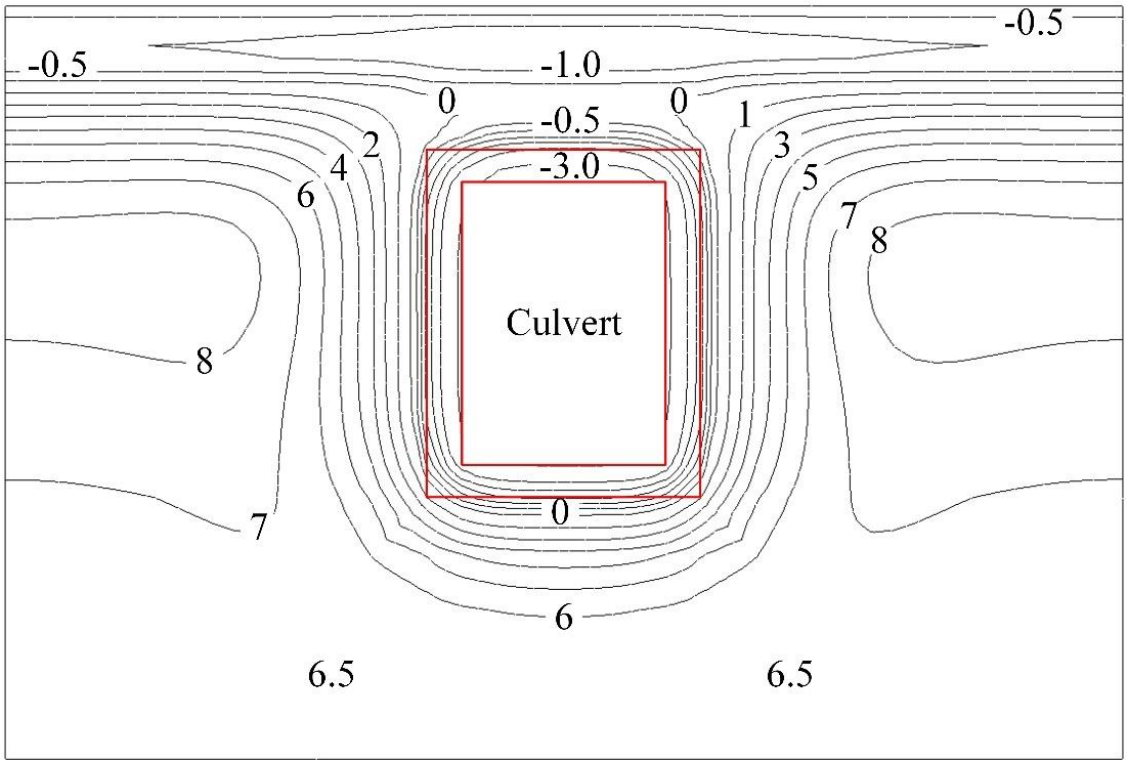

Figure 4.13 Temperature distribution at the end of freeze process

Uneven Freeze-Thaw Deformation

For the particular thermal regime mentioned above, the ground surface over the box culvert tends to upheave more than the adjacent zone (Figure 4.14). The amount of upheaving at points A and B was 13.5 mm and 1.7 mm, respectively, resulting in 11.8 mm uneven frost heave along the longitudinal direction of pavement. Though the estimated value is less than the observed 20-30 mm, this non-uniform deformation may also lead to roughness and cracking of pavement, significantly affecting the safety and comfort of driving. Also, the enhanced dynamic interaction between automobile and pavement structure will in turn further degrade pavement performance. Compared with the ground surface heave, horizontal expansion deformation of the culvert is relatively small (0.3 mm). As the confining stress at the back of culvert ranges from 70-150 kPa, which is larger than that of the fill (0-70 kPa) above the culvert, such phenomena are rational considering the relation between overburden pressure and axial strain (Figure 4.8).

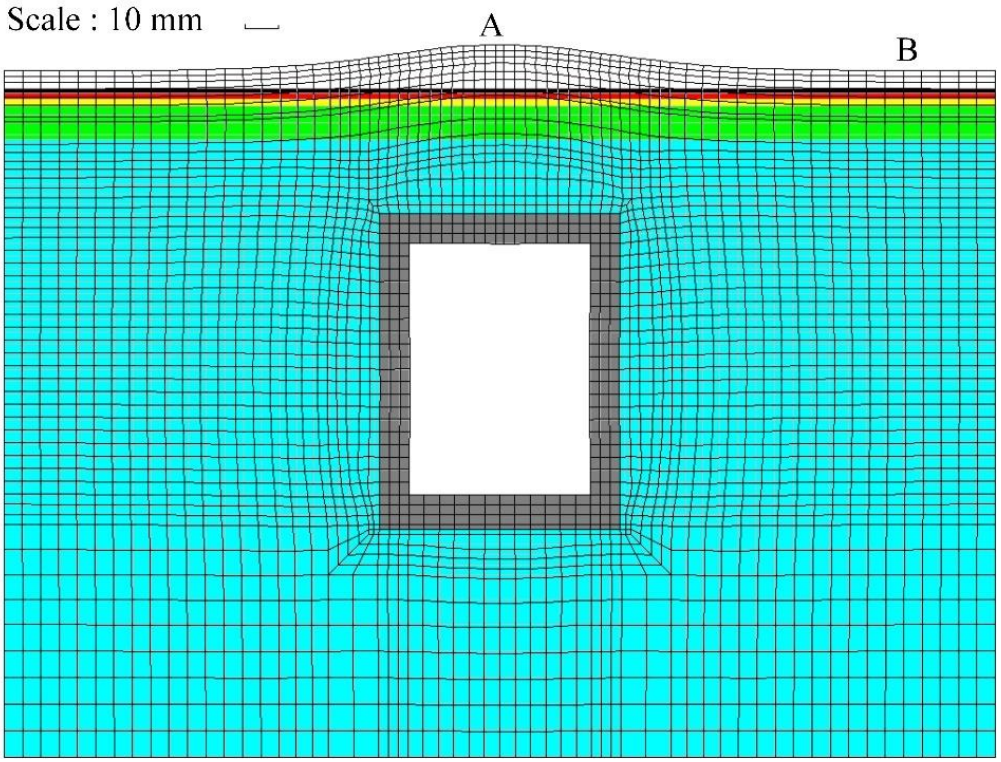

Figure 4.14 Uneven freeze-thaw deformation of pavement in freeze process

A dip above the culvert can be observed during the thawing process, and these dips causing severe roughness are significantly disruptive to traffic. However, the depth of dip, the difference in elevation between points A and C, is only 1.2 mm in this simulation (Figure 4.15).

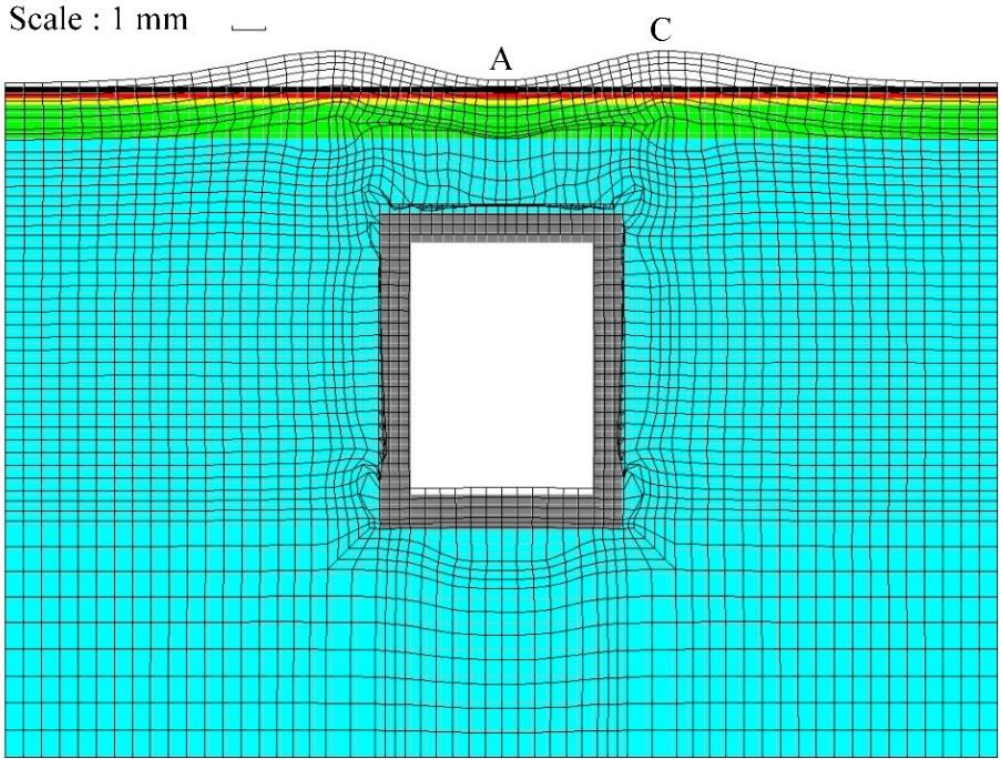

Figure 4.15 Uneven freeze-thaw deformation of pavement in thaw process

Frost Heaving Force

The frost expansion of soil at the back of culvert induced frost heaving force, considered to be 32 kPa simulated horizontal stress. According to design information, the uniform distributed load was applied to the 8.5 m high doubly-clamped beam. The reinforcement stress was obtained using principles of reinforced concrete structures. Figure 4.16 compares simulated and monitored reinforcement stress. A positive value represents the tension of the steel bar, while negative value describes the relaxation of stress. When the air temperature rises, tensile stress is reduced. The maximum stress relaxation measured was -140 MPa, while the simulated value was -104 MPa. Taking the difference between backfill and Touryo soil into account, this coupled THM analysis can accurately reproduce the freeze-thaw behavior of pavement located on a box culvert both qualitatively and quantitatively.

Compressive stress (blue arrow) and tensile stress (red arrow) during the freezing process are illustrated in Figure 4.17. The middle of the sidewall is subjected to tensile stress on its inner surface, induced by frost heaving force and releasing during the subsequent thaw process. Earth pressure and self-weight cause initial reinforcement tensile stress of 70 MPa. Adding the additional 104 MPa tensile stress due to frost heaving force, the total tensile stress is 174 MPa, which is close to the 250 MPa reinforcement yield stress. This stress level is likely high enough to cause long-term damage, and it has been reported that a 0.24 mm wide crack appeared in the

culvert sidewall. Uneven frost heave and decreasing temperature produce tension in the asphalt mixture layer. As tensile stress on top of asphalt mixture layer (1 MPa) is larger than that at the bottom (0.5 MPa), it is thought that top-down cracking may be produced. On the contrary, with the presence of wheel load total tensile stress at the bottom (1.1 MPa) is greater than that on top (0.4 MPa), resulting in bottom-up cracking. When automobiles cross the culvert, pavement undergoes alternating stress which may significantly shorten its fatigue life.

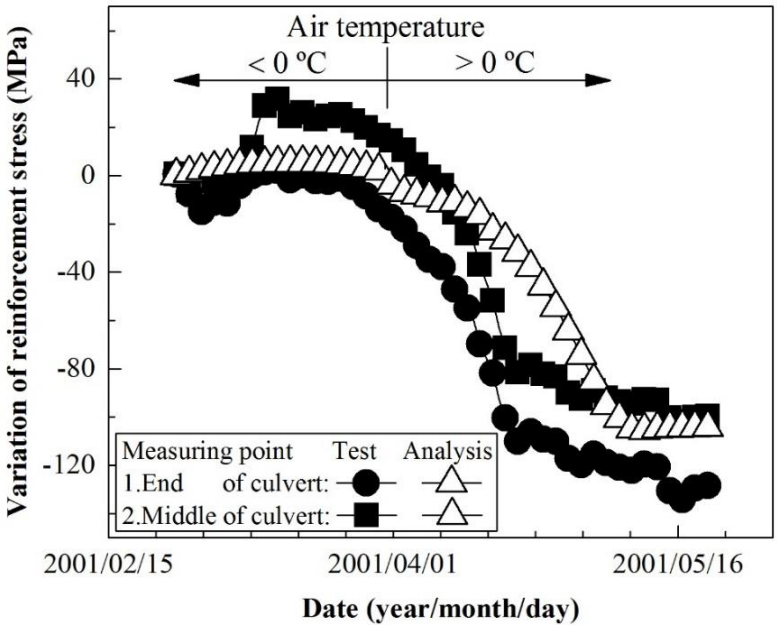

Figure 4.16 Comparison of stress variation of reinforcement

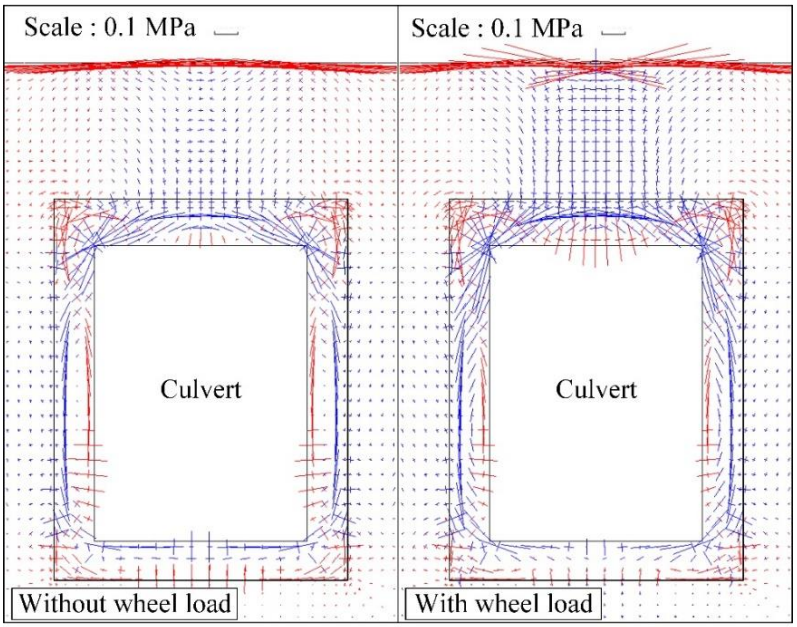

Figure 4.17 Distribution of principal stress vector in freeze process

Countermeasure Against Frost Heave

The allowable number of equivalent 49 kN wheel load (N_{fa}) is employed to evaluate pavement fatigue life (Japan Road Association, 2006). A larger N_{fa} means a longer fatigue life and service time.

$$N_{fa} = \beta_{a1} Z \left(6.167 \times 10^{-5} \varepsilon_t^{-3.291\beta_{a2}} E_1^{-0.854\beta_{a3}} \right) \quad 4.3$$

where N_{fa} is required number of cyclic wheel loads to cause cracking in the asphalt mixture layer; Z is parameter associated with volume characteristics of the asphalt mixture layer; E_1 is Young's module of the asphalt mixture layer, related to temperature, and ranging from 5000 to 10000 MPa; β_{a1}, β_{a2}, and β_{a3} are empirical correction coefficient; and ε_t is tensile strain at the bottom of the asphalt mixture layer.

To mitigate damage caused by uneven frost heave, the applicability of using an insulation material to improve thermal regime was evaluated by performing parametric studies with and without insulation material under five different conditions (Figure 4.18).

Condition No.	XPS around culvert	Length of XPS under C-80 (m)	Schematic diagram
1	No	No insulation installed below C-80	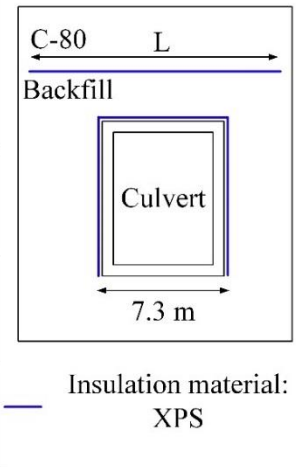
2	Yes		
3		7.3	
4		10.3	
5		13.3	

Figure 4.18 Countermeasure against frost heave: layout of XPS

The XPS material is introduced in the model. Condition 1 is given without any insulation material. Four of the remaining conditions have XPS around the culvert. Among the four conditions, three conditions include XPS installed below C-80 with different lengths. The fatigue life and roughness of pavement under different thermal and load conditions were investigated (Figure 4.19).

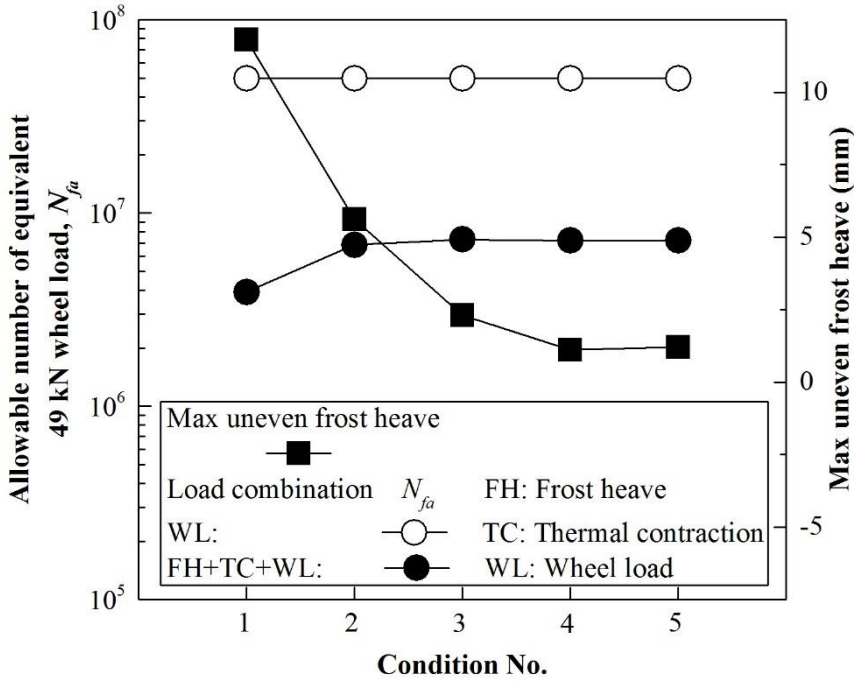

Figure 4.19 Fatigue life and roughness of pavement under different thermal and load combination conditions

Without any insulation, material condition 1 shows the largest uneven frost heave and smallest N_{fa}. Frost heave and thermal contraction have a more significant impact on fatigue life of asphalt layer than wheel load, as determined through comparison of unfilled and filled circles in Figure 4.19. In condition 2, double-sided cooling converts into single-sided cooling with the XPS material around the culvert. As a result, uneven frost heave is less than that of condition 1, and thus N_{fa} in the freezing process increases. In addition to the XPS wrapped around the culvert, the presence of XPS between C-80 and backfill can further reduce frost heave significantly, as shown in condition 3. As the length of XPS under C-80 is increased, uneven frost heave is gradually decreased. When the length of XPS reaches 10.3 m, exceeding each side of the culvert by 1.5 m, the difference of uneven deformation becomes negligible (condition 4). Accordingly, laying XPS both around the culvert and underneath the C-80 layer can minimize uneven frost heave and improve pavement lifespan.

4.2.4 Remarks

The following conclusions can be derived from this study:

1. A coupled THM model, specially developed to predict the freeze-thaw behavior of unsaturated soil, has been proposed and implemented into a finite element system. The performance of the model is demonstrated through a good agreement between analytical predictions and measurements of frost heave tests under different conditions.

2. The simulation reproduced the primary behavior of the pavement during the freeze-thaw process. The frost penetration depth is much deeper for the pavement right above the culvert than in the adjacent zones. A hump and a dip of pavement appear above the culvert during the freeze and thaw processes, respectively. The frost heaving force is high enough to cause cracking of the culvert. Uneven frost heave and thermal contraction cause considerable tensile stress in the asphalt mixture layer and this has a more significant impact on the fatigue life than the wheel load. An insulation material wrapped around the culvert and above the frost-susceptible soil may mitigate the damage from uneven frost heave.

4.3 STRESS CHANGE IN PAVEMENT SUBJECTED TO FREEZE-THAW

4.3.1 Problem statement

In the seasonal cold region, the pavement is exposed to climatic change which causes periodic temperature variation and freeze-thaw of soils in the pavement. For porous material like soil, the phase transition of pore-water to ice results in changes of the physical and mechanical index including permeability, thermal properties, and resilient modulus, etc. These changes highly affect the performance of the pavement structure which is treated as a multilayer system in engineering design. A series of the study was conducted to investigate the relationship between the change of resilient modulus and freeze-thaw of soils by former researchers (Cole et al., 1981; Simonsen and Isacsson, 2001; Simonsen et al., 2002), along with thaw weakening of pavement structures (Janoo and Berg, 1990). The in-situ survey and laboratory experiments were carried out to investigate the effects of climatic change and material properties on mechanistic-empirical pavement design guide (MEPDG) in cold region; it is indicated that there is a need to consider resilient modulus related to freezing and thawing for the design based on multilayer elastic theory (Abe et al., 2011). Recently from an investigation on the stress distribution in the ground beneath pavements, the change of stress distribution associated with freezing and thawing was pointed out (Kishikawa et al., 2017). For the conventional stress analysis method, the value of resilient modulus needs to be assigned manually for the frozen and thawed stage; a time-depend stress change is hard to be achieved. The prerequisite for accurate stress analysis is the determination of temperature distribution in the pavement; then the proper resilient modulus values can be set. As the thermal analysis is a complex boundary value problem, which is also associated with seepage analysis, a comprehensive analysis method that can implement multi-field analysis is expected.

4.3.2 Numerical model

A typical pavement structure in the cold snowy region, Hokkaido (Kitami city), is selected and simulated (Figure 4.20). The pavement is composed of surfacing layer, base course, frost protection layer (subbase) and subgrade. In the simulation, only one-half of the pavement is considered for simplicity, and simulated domain extends 7 m in width and 5 m in depth. Subsurface layers, which are close to the pavement surface and influenced by climatic change, are given fine meshing (0.1 m) to capture time-dependent stress change. Elements of larger size (0.25 m) are assigned to lower part of the model to reduce calculation scale and save computation time. There is no potential frost heave reported in investigation mentioned before, therefore the stress change induced by frost heave is not accounted. Thermal expansion and contraction are also ignored to examine the main concern of this study, that is the effects of frost-induced change of resilient modulus of subsurface soils on stress change in the pavement.

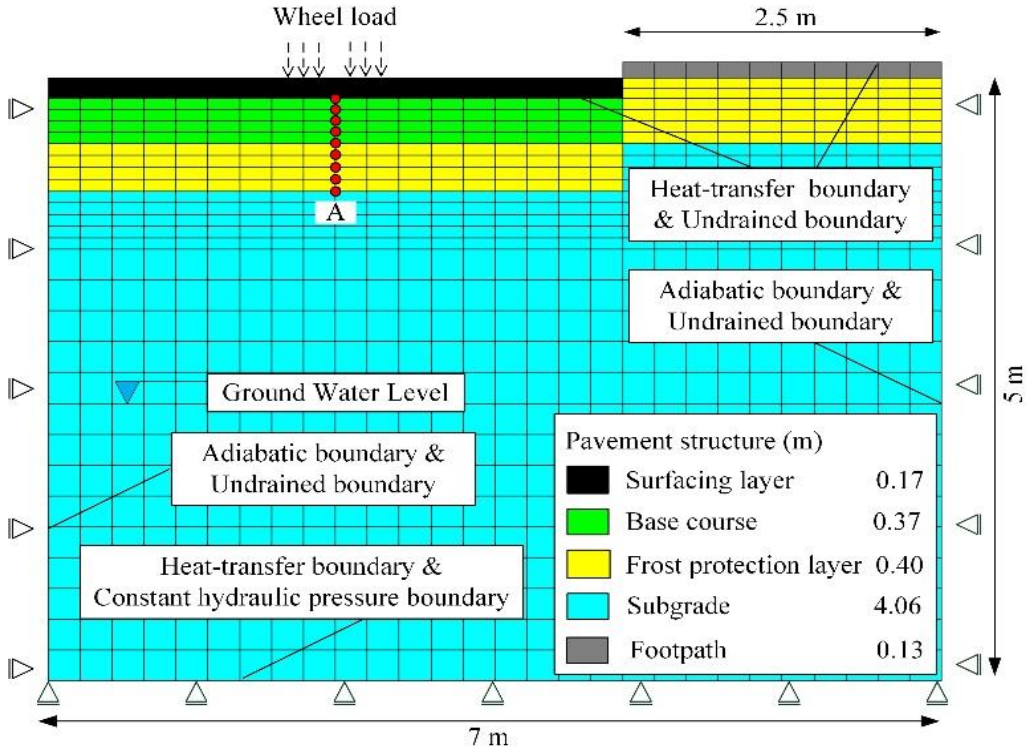

Figure 4.20 Profile of simulated pavement

The flexible pavement in this simulation consists of several types of materials. Surfacing layer is made of asphalt concrete, while graded gravel (C-40) constitutes a base course distributing wheel load to underneath layers. The footpath is constructed using concrete material. Since detailed information on in-situ soils is not available, two types of volcanic soils used in pavement engineering in Hokkaido are specified for frost protection layer and subgrade, which may somewhat differ from the field condition. For frost protection layer, non-frost susceptible coarse-grained volcanic soil (Komaoka soil) can limit or prevent frost penetration in frost-susceptible subgrade soil and further load distribution. A representative fine-grained volcanic soil (Touryo soil) is chosen as subgrade soil.

Representative values for the input parameters of these materials are selected for the sake of generality (Table 4.3). More specifically, the values of resilient modulus of unfrozen, frozen and thawed soils are referenced from the previous study, in which the falling weight deflectometer test (FWD test) and resilient modulus test (MR test) are conducted to estimate the climatic effects on the modulus of pavement materials. Note that the temperature dependence of the modulus of asphalt concrete is roughly considered by specifying two different values for unfrozen and frozen asphalt. It is also should note that the constant thermal conductivity may reduce the frost penetration in this research.

Table 4.3 Input parameters in pavement analysis

Parameters	Asphalt	C-40	Komaoka	Touryo	Concrete
Dry density of soil (ρ_d) kg/m^3	2100	2000	1400	1400	2200
Porosity (n)	0.030	0.230	0.670	0.450	0.050
Final freezing temperature (T_f) °C	0	-0.05	-0.10	-0.20	0
Thermal conductivity of soil (λ_T) W/m°C	1.45	1.66	2.16	1.61	0.94
Volumetric heat capacity of soil particles (C_{Tp}) J/m^3°C	1.8E+6	1.8E+6	1.9E+6	1.8E+6	2.0E+6
van Genuchten-Mualem fitting parameter (α) 1/MPa	-	825.14	121.69	93.20	-
van Genuchten-Mualem fitting parameter (λ)	-	1.42	2.09	1.596	-
Saturated water hydraulic conductivity (k_s) m/s	1.0E-10	1.0E-5	1.0E-5	1.0E-8	1.0E-10
Young's modulus of unfrozen soil (E_u) MPa	6000	300	200	40	21700
Young's modulus of frozen soil (E_f) MPa	12000	2000	2000	2000	21700
Young's modulus of thawed soil (E_t) MPa	6000	150	100	20	21700
Poisson's ratio (υ)	0.35	0.35	0.35	0.40	0.20

As the ground surface is hardened by impervious material like asphalt concrete and cement, no infiltration (rainfall and snowfall) is considered. Accordingly, the constant pore-water pressure is employed at the bottom boundary to achieve constant groundwater level (2.8 m below surface). A linear suction gradient (negative pore-water pressure) is set above the groundwater level, then water content is determined based on VG model. A sinusoidal function is applied to approximate and simplify periodic temperature variation (Equation 4.1), and the recent 5 years' meteorological data is used to perform curve fitting and determine the coefficients in the equation. Likewise, the ground temperature at the bottom of the model is also described by a sine function which is weakened and delayed behind surface temperature (Equation 4.2). It is well known that snow accumulation significantly reduces heat transfer between ground and atmosphere. The surface temperature of the footpath, therefore, is assumed to be 0 °C when the air temperature drops below 0 °C and snowfall accumulates on the footpath, to roughly estimate thermal effects of the snowpack.

A surface temperature is calculated by assigning mean annual temperature, 6.77 °C; surface temperature amplitude, 15.37 °C; corresponding period, 365 days; initial phase, -2.98 rad; an increment of temperature for black surface pavement, 3 °C. The ground temperature is determined by setting depth below the air temperature boundary, 5 m; thermal diffusivity, 5.17E-2 m^2/day

(Figure 4.21).

The initial temperature condition is obtained through a 5 years' heat transfer till thermal equilibrium with the temperature boundaries described previously. Distributed loads are imposed at the surface layer for interested time steps to simulate wheel load (0.61 MPa), which is derived from standard traffic load (49 kN), and the change of stress increment induced by traffic load can be studied in this multi-layer system.

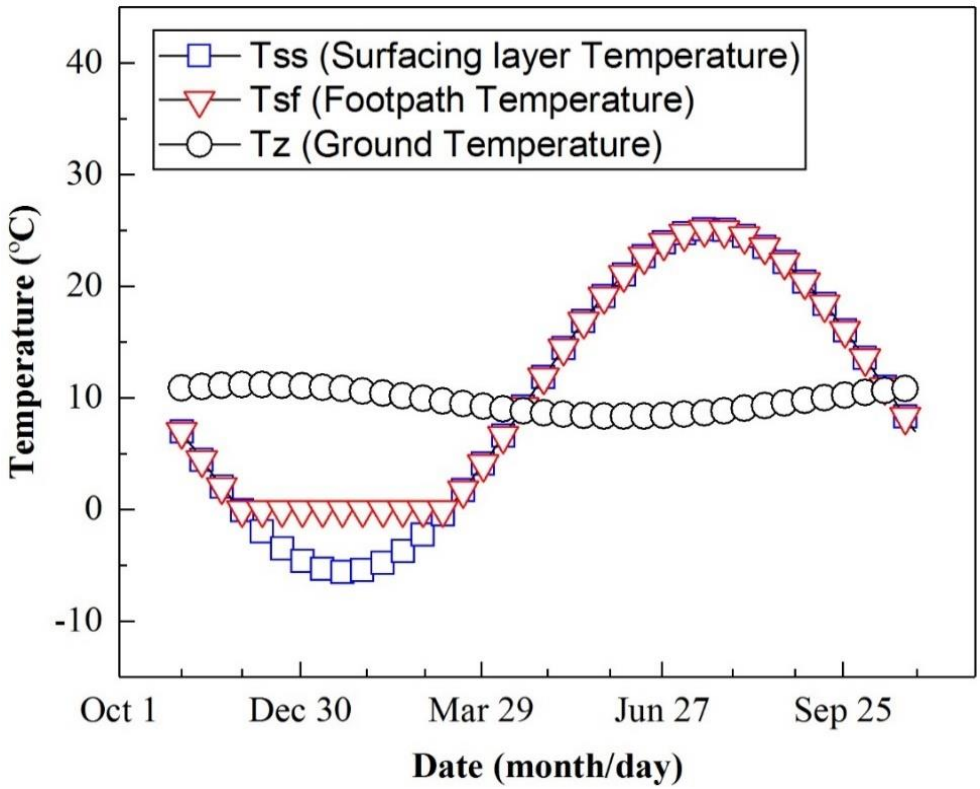

Figure 4.21 Temperature boundary in simulation

4.3.3 Results and discussions

The freeze-thaw of pavement

Frost line penetrates pavement gradually when the air temperature drops below 0 °C (Figure 4.22). Surfacing layer and base course retain less water, accordingly, 0 °C line goes through these two layers rapidly. However, it takes apparently longer time to freeze frost protection layer that has a larger water content and heat capacity. For this reason, the existence of frost protection layer contributes to resisting the advance of frost penetration into subgrade that always keeps unfrozen.

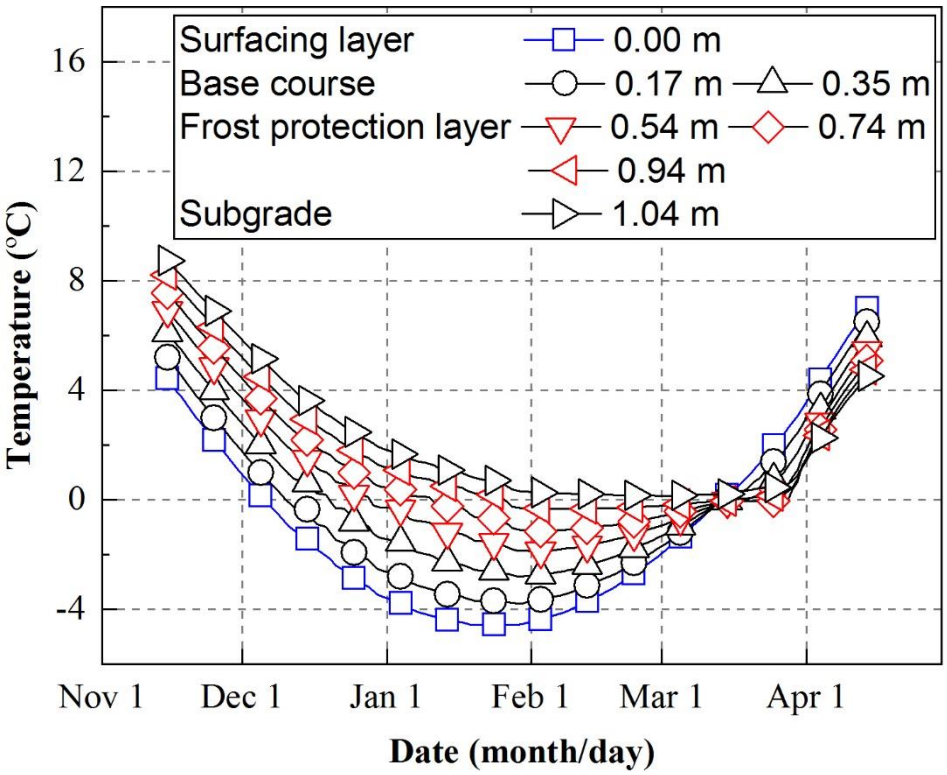

Figure 4.22 Temperature history in the pavement

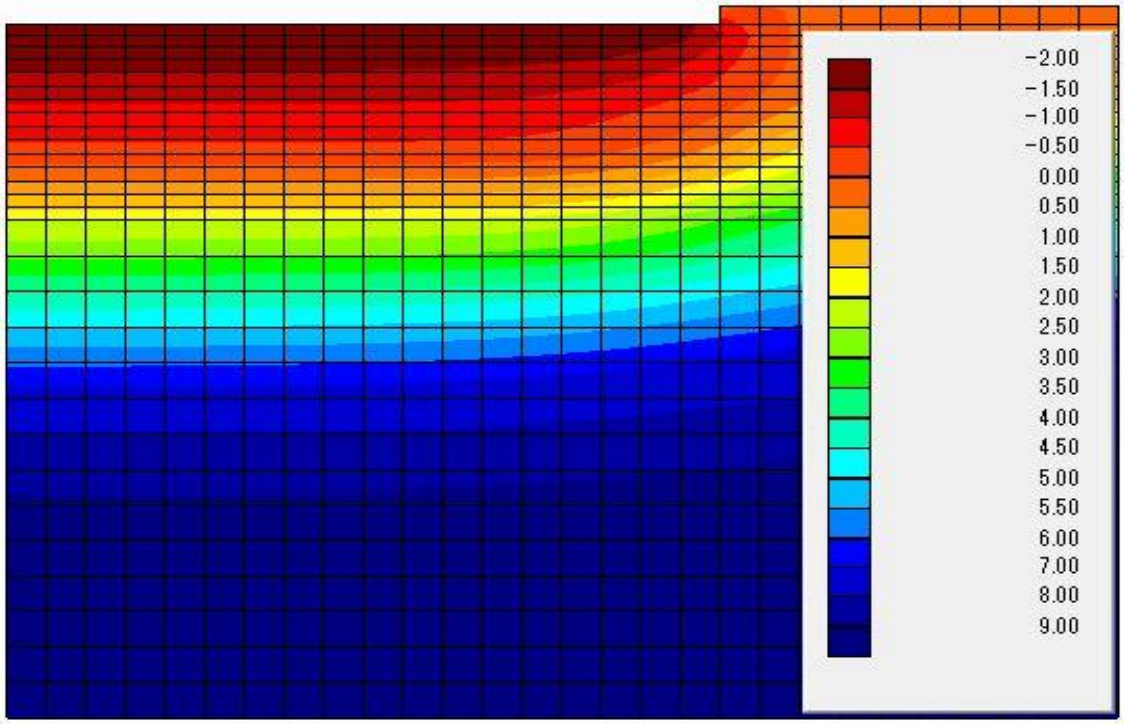

Figure 4.23 Temperature distribution on March 1st

The snowpack on footpath changes thermal condition in pavement during the winter season. Figure 4.23 presents the temperature distribution during the freezing process, the temperature under the pavement is lower than that under footpath with snow cover of which thermal conductivity is quite small. This thermal pattern gives rise to a frost penetration that is not parallel with the ground surface. It is also believed that a differential cooling accumulation along the cross-section of pavement results in a special thawing pattern, namely the thawing of the central section of pavement comes later than that close to the footpath (Figure 4.24).

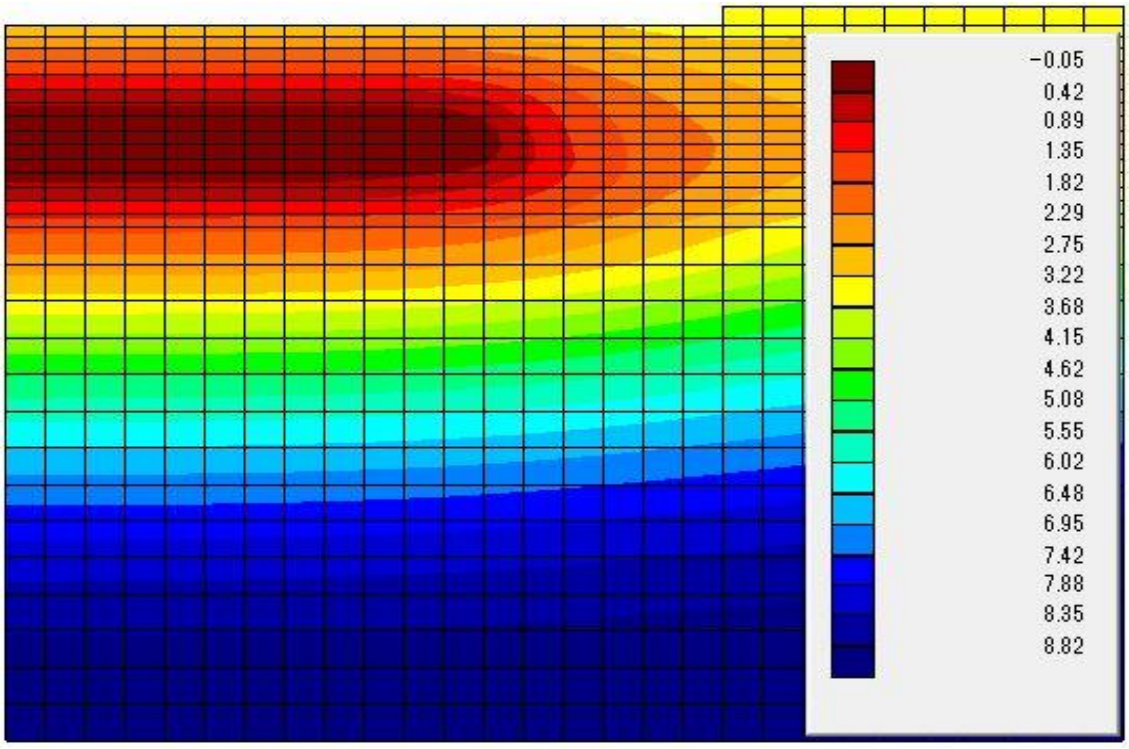

Figure 4.24 Temperature distribution on April 1st

Stress change in pavement

The layers below surface become frozen with the advance of the frost line, and therefore the phase change of water bonds soil particles and get the soils stiffer. The mechanical meaning of this physical change is that resilient modulus significantly increases. A resembling phenomenon is the weakness of mechanical properties of thawed soil during springtime, namely the decreased resilient modulus is even smaller than the value before freezing, as freeze-thaw cycle tends to increase the net volume of soil and looser soil structure decrease resilient modulus

Figure 4.25 presents stress variation in the pavement during winter and spring, and the locations of measuring points are represented by red circles in Figure 4.20. For the freezing process, the stress in upper frozen layers increases compared with the unfrozen state, while a decrease of stress is observed in the lower unfrozen layer. The stiffer base course and frost protection layer enhance

load dispersion in a wider region, as a result, the stress in subgrade soil is reduced. In springtime, the thawing proceeds from both the top downward and bottom upward with the arrival of warm surface temperature, therefore, the stress change appears within one month corresponding to the thawing duration of pavement. A reverse tendency is that reduction of stress in thawed upper layers takes place, while stress concurrently rises in the lower layer. Eventually, stress in base course and frost protection layer decreases and stress in subgrade increases through the comparison of unfrozen and thawed values.

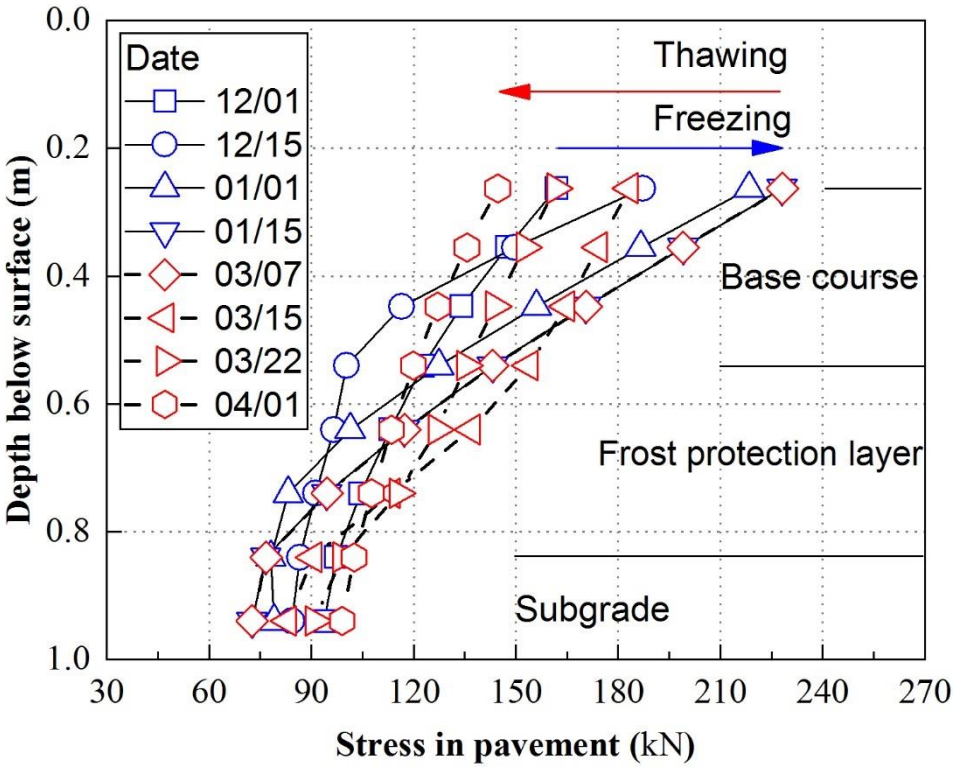

Figure 4.25 Stress variation in the pavement

The stress in subgrade soil is one of the main concerns in engineering practice. Both temperature and stress at the top of subgrade (see Point A in Figure 4.20) are plotted in Figure 4.26. With the descending of surface temperature, overlying base course and frost protection layer gradually get frozen, the temperature at Point A drops together with a decrease of stress. After more than two months of heat transfer, the thermal equilibrium is reached. As a result, temperature sustains a constant that is always slightly above 0, along with constant stress. The entire pavement is thawed within one month during the subsequent spring season due to two sides warming described previously, and the final value of stress is larger than unfrozen one.

As we know, the stress and strain level at the top of subgrade can be employed to estimate the possibility of permanent deformation of pavement indirectly. To quantify the effect of stress change on the performance of pavement structure, the allowable number of equivalent 49 kN

wheel load (N_{fs}) is applied to evaluate the lifespan of pavement. A larger N_{fs} represents a longer service time which is calculated by the empirical equation below (Japan Road Association, 2006),

$$N_{fs} = \beta_{s1} \cdot \left(1.365 \times 10^{-9} \cdot \varepsilon_z^{-4.477\beta_{s2}}\right) \quad 4.4$$

where N_{fs} is required number of cyclic wheel loads to cause 15 mm permanent deformation in layers which results in rutting in flexible pavement; β_{s1} and β_{s2} are empirical correction coefficient; and ε_z is compressive strain at the top of the subgrade.

Figure 4.27 shows the relation between the change of stress at the top of subgrade and an allowable number of equivalent 49 kN wheel. The decrease of stress temporarily strengths the ability of the pavement to resist residual deformation during the winter season. However, the stress increment of 1.73 kPa can highly shorten the service time of pavement during the spring season compared with the unfrozen state. To alleviate this problem, load restriction is suggested to account.

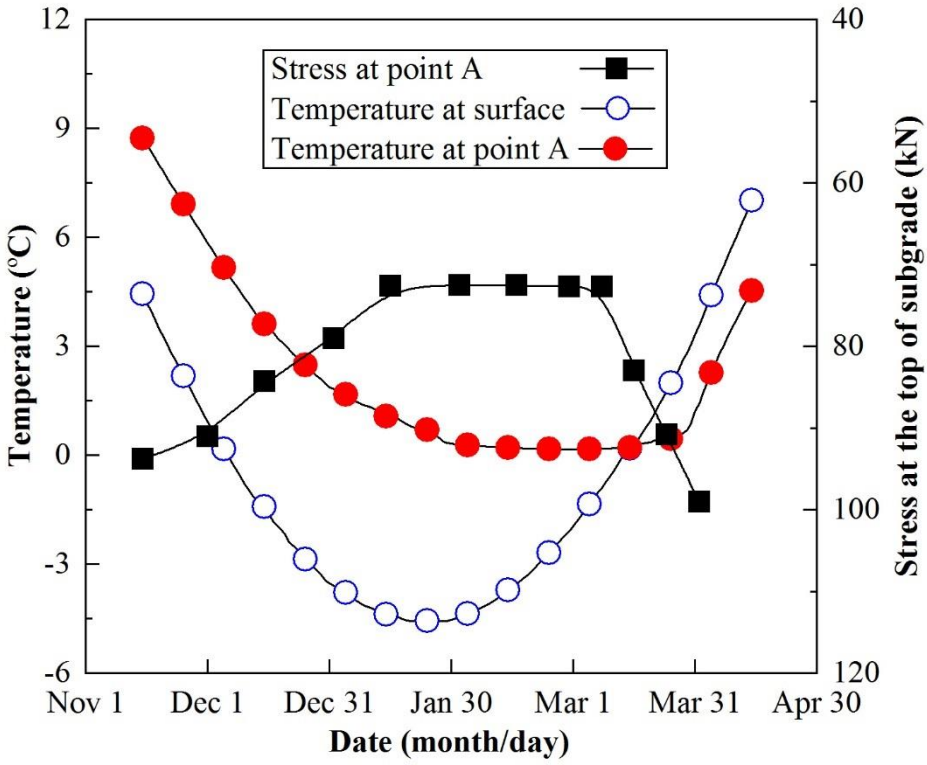

Figure 4.26 Temperature and stress at the top of the subgrade

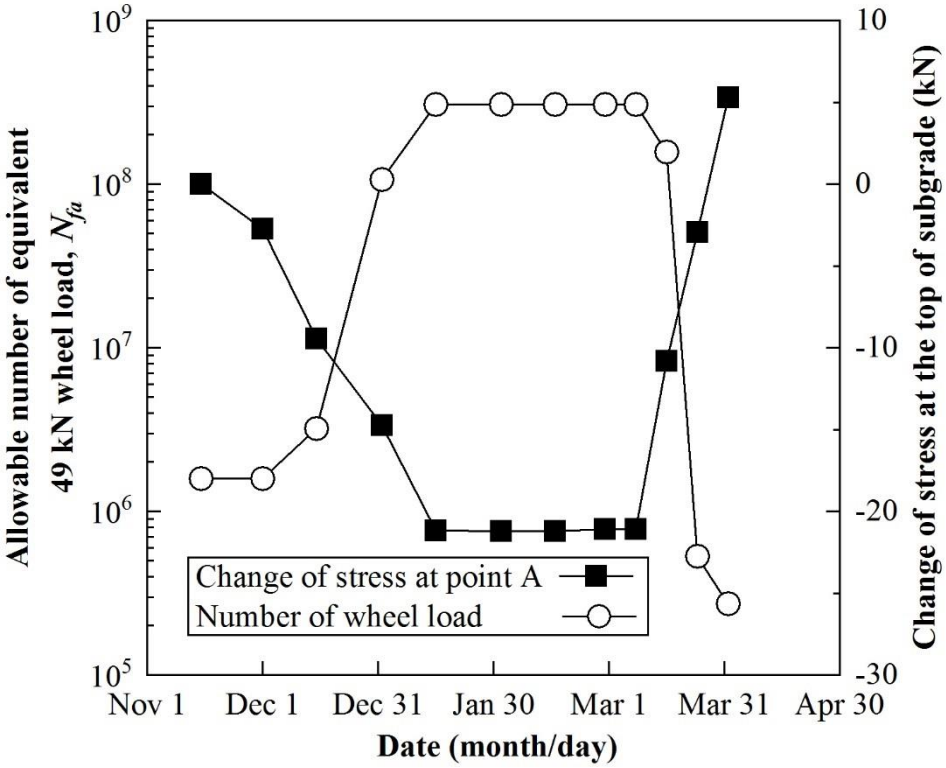

Figure 4.27 An allowable number of equivalent wheel load and change of stress at the top of the subgrade

4.3.4 Remarks

The following conclusions can be drawn from this study:

1. The thermal pattern in pavement located in the cold region was reproduced. The snow cover on the footpath that affects temperature distribution in pavement should be properly considered. The presence of frost protection layer can effectively resist and limit frost penetration in the subgrade.

2. The stress change in pavement is highly associated with the variation of resilient modulus that is sensitive to temperature. The stress variation in base course and frost protection layer presents a reverse trend compared with subgrade. The stress increment of subgrade in springtime may greatly deteriorate the performance of pavement and shorten its service life.

5 FURTHER DEVELOPMENT OF MODEL

5.1 MODIFIED GOVERNING EQUATIONS

5.1.1 Mass conservation equation

First, let us recall the continuity equation derived in chapter 3.

$$\nabla \cdot \left[-k_w \nabla \left(\frac{u_w}{\rho_w g} + z \right) \right] = \frac{1}{K_b} \frac{\partial u_w}{\partial t} + S_w \alpha_{Tu} \frac{\partial T}{\partial t} - S_w \frac{\partial \varepsilon_v}{\partial t} \tag{3.58}$$

Equation 3.58 indicates that S_w is total water saturation in two phases, namely sum of both liquid water saturation and solid ice saturation when the soil temperature is below freezing point. That also means liquid-gas capillary pressure (suction) is related to total quantity of water and ice on gas-liquid interface when an air-ice contact is assumed not present. However, this equation cannot capture primary character of freezing soil that is cryogenic suction induced by ice-liquid interface tension, which is dominant in water migration in freezing soil. Despite thermal expansion, change of temperature alone cannot cause pore-water pressure change, because stored mass on the left side of the equation does not change. This drawback prevents model from simulating water migration (redistribution) in soil subjected to freezing, which has been observed and studied in past several decades. Once liquid water is frozen and solidified into ice, this portion of water is immovable. Ignoring the ice flux term and treating ice mass term as sink term, the equation is given as,

$$C_H \frac{\partial u_w}{\partial t} = -\nabla \cdot \left(-k_w \nabla h \right) + n S_w \alpha_{Tw} \frac{\partial T}{\partial t} - S_w \frac{\partial \varepsilon_v}{\partial t} - \frac{\rho_i}{\rho_w} n \frac{\partial S_i}{\partial t} \tag{5.1}$$

This is the governing equation of mass conservation for the hydraulic field. If unsaturated-saturated seepage takes place with positive temperature, namely no ice formation, then the last term on the right side of equation vanishes. If the soil is nondeformable and mechanical factor is not taken account, the second to last term on the right side of the equation eliminates. If the process happens under the isothermal condition, the third to last term on the right side of the equation disappears. If all the above three factors are ignored, the Equation 5.1 reduces to classic Richards equation (Richards, 1931), which is given as,

$$C_H \frac{\partial u_w}{\partial t} = -\nabla \cdot \left(-k_w \nabla h \right) \tag{5.2}$$

5.1.2 Energy conservation equation

The energy conservation equation derived in chapter 3,

$$C_T \frac{\partial T}{\partial t} + L \frac{\partial \theta_i}{\partial t} = \nabla \cdot \left(-\lambda_T \nabla T \right) - C_{Tw} \nabla \cdot \left(\boldsymbol{v}_w T \right) \tag{3.21}$$

To introduce the influence of mechanical deformation on energy conservation,

$$\frac{\partial \theta_i}{\partial t} = \frac{\partial (nS_i)}{\partial t} = S_i \frac{\partial n}{\partial t} + n \frac{\partial S_i}{\partial t} = S_i \frac{\partial n}{\partial t} + n \frac{\partial S_i}{\partial T} \frac{\partial T}{\partial t} \tag{5.3}$$

Substituting Equation 5.3 into Equation 3.21 and collecting the derivative of temperature with respect to time term.

$$\left(C_T + Ln \frac{\partial S_i}{\partial T} \right) \frac{\partial T}{\partial t} + LS_i \frac{\partial n}{\partial t} = \nabla \cdot (-\lambda_T \nabla T) - C_{Tw} \nabla \cdot (\boldsymbol{v}_w T) \tag{5.4}$$

The term within the braces on the left side of Equation 5.4 is defined as so-called apparent heat capacity.

$$C_{Ta} = C_T + L \frac{\partial \theta_i}{\partial T} \tag{5.5}$$

where C_{Ta} is apparent heat capacity of soil.

Finally, the governing equation for energy conservation is obtained, which shares a similar form with Zhou and Li's study (2012).

$$C_{Ta} \frac{\partial T}{\partial t} + LS_i \frac{\partial n}{\partial t} = \nabla \cdot (-\lambda_T \nabla T) - C_{Tw} \nabla \cdot (\boldsymbol{v}_w T) \tag{5.6}$$

5.1.3 Equilibrium equation

Fredlund's two stress state variables theory is applied when modeling stress-strain relationship (Fredlund and Morgenstern, 1976).

$$\frac{\partial \varepsilon_v}{\partial t} = \frac{1}{K} \frac{\partial (\sigma_m - u_a)}{\partial t} + \frac{3}{H} \frac{\partial (u_a - u_w)}{\partial t} \tag{5.7}$$

where H is modulus of elasticity for soil structure with respect to change in matric suction, u_a-u_w. To treat pore-air pressure (u_a) as gauge pressure, and introduce thermal expansion strain and frost heave strain into equation 5.7 and rearrange terms,

$$\frac{\partial \sigma_m}{\partial t} = K \frac{\partial \varepsilon_v}{\partial t} + K \frac{3}{H} \frac{\partial u_w}{\partial t} - K \alpha_T \frac{\partial T}{\partial t} - K \frac{\partial \varepsilon_{f/t}}{\partial t} \tag{5.8}$$

Stress-strain relationship including the shear component is given as,

$$\frac{\partial \sigma_{ij}}{\partial t} = \left(K - \frac{2}{3} G \right) \frac{\partial \varepsilon_{kk}}{\partial t} \delta_{ij} + 2G \frac{\partial \varepsilon_{ij}}{\partial t} + \frac{\partial \sigma_0}{\partial t} \delta_{ij} \tag{5.9}$$

$$\frac{\partial \sigma_0}{\partial t} = K \frac{3}{H} \frac{\partial u_w}{\partial t} - K \alpha_T \frac{\partial T}{\partial t} - K \frac{\partial \varepsilon_{f/t}}{\partial t} \tag{5.10}$$

Considering static equilibrium and displacement-strain relation, the equation to be finally solved is obtained.

$$\left\{\frac{1}{2}C_{ijkl}\left(u_{k,l}+u_{l,k}\right)+\sigma_0\delta_{ij}\right\}_{,j}+\rho g_i=0 \tag{5.11}$$

5.1.4 Summary of modified governing equations

Continuity equation

$$C_H\frac{\partial u_w}{\partial t}=-\nabla\cdot\left(-k_w\nabla H\right)+nS_w\alpha_{Tw}\frac{\partial T}{\partial t}-S_w\frac{\partial \varepsilon_v}{\partial t}-\frac{\rho_i}{\rho_w}n\frac{\partial S_i}{\partial t} \tag{5.1}$$

Energy conservation

$$C_{Ta}\frac{\partial T}{\partial t}+LS_i\frac{\partial n}{\partial t}=\nabla\cdot\left(-\lambda_T\nabla T\right)-C_{Tw}\nabla\cdot\left(\boldsymbol{v_w}T\right) \tag{5.6}$$

Equilibrium equation

$$\left\{\frac{1}{2}C_{ijkl}\left(u_{k,l}+u_{l,k}\right)+\sigma_0\delta_{ij}\right\}_{,j}+\rho g_i=0 \tag{5.11}$$

$$\frac{\partial\sigma_0}{\partial t}=K\frac{3}{H}\frac{\partial u_w}{\partial t}-K\alpha_T\frac{\partial T}{\partial t}-K\frac{\partial \varepsilon_{f/t}}{\partial t} \tag{5.10}$$

5.2 MODIFIED NONLINEAR SOIL PROPERTIES

When the temperature is lowered from room temperature, water freezes at around 0 °C. It is thought that various changes will occur in the physical properties of the ground accompanying it.

5.2.1 Hydraulic properties

Permeability of unsaturated soil

Permeability of unsaturated soil is described the as same as the one in chapter 3.

$$k_w=k_{wr}k_s \tag{3.17}$$

$$k_{wr}=\left(S_e\right)^{1/2}\left[1-\left(1-S_e^{\frac{\lambda}{\lambda-1}}\right)^{\frac{\lambda-1}{\lambda}}\right]^2 \tag{3.60}$$

$$S_e=\left[1+\left(\alpha\psi\right)^{\lambda}\right]^{\frac{1-\lambda}{\lambda}} \tag{3.61}$$

$$S_e=\frac{S_w-S_{rr}}{S_{rs}-S_{rr}} \tag{3.62}$$

Modified permeability of freezing soil

It is believed that the concept of relative hydraulic conductivity of unsaturated soil is also applicable for the freezing case. The only note is that an impedance factor should be introduced to account for the blocking effect of pore ice on the hydraulic conductivity. The following formula

is applied instead of Equation 3.65 in chapter 3 in which Ω is impedance factor (Taylor and Luthin, 1978).

$$k_{wf} = 10^{-\Omega\theta_i} k_w \tag{5.12}$$

5.2.2 Thermal properties

Thermal conductivity

Thermal conductivity of ice (2.24 J/sec·m°C) is larger than water (0.60 J/sec·m°C). It is essential to take the influence of phase change on thermal conductivity into consideration. Côté and Konrad (2005) developed a generalized thermal conductivity model for moist soils based on the concept of normalized thermal conductivity proposed by Johansen (1977) which tends to overestimate thermal conductivity of frozen soil since influence of unfrozen water content is not well accounted for.

$$\lambda_T = \left(\lambda_{sat} - \lambda_{dry}\right) \times k_{Tr} + \lambda_{dry} \tag{5.13}$$

where λ_{sat} is thermal conductivity of saturated soil; λ_{dry} is thermal conductivity of dry soil, and k_{Tr} is normalized thermal conductivity.

The thermal conductivity of dry soil is directly related to the porosity since it is believed that the mineral content of solid particles only slightly influences thermal conductivity of dry soil.

$$\lambda_{dry} = \chi \times 10^{-\eta n} \tag{5.14}$$

where χ and η are material parameters considering particle shape effect, which are 1.7 and 1.8 for crushed rocks and gravels, 0.75 and 1.2 for natural mineral soils, respectively.

For unfrozen soil, the thermal conductivity of saturated soil is given as,

$$\lambda_{sat} = \left(\lambda_s\right)^{1-n} \left(\lambda_w\right)^n \tag{5.15}$$

where λ_s is thermal conductivity of soil particles; and λ_w is thermal conductivity of water.

The thermal conductivity of frozen saturated soil is weighted by the volumetric partition of each component.

$$\lambda_{sat} = \left(\lambda_s\right)^{1-n} \left(\lambda_i\right)^{n-\theta_u} \left(\lambda_w\right)^{\theta_u} \tag{5.16}$$

where λ_i is thermal conductivity of ice; and θ_u is volumetric unfrozen water content.

The normalized thermal conductivity is given in the form of following generalized equation,

$$k_{Tr} = \frac{\kappa S_r}{1+(\kappa-1)S_r} \tag{5.17}$$

where κ is an empirical parameter depending on soil types; and S_r is degree of saturation including water in liquid and solid phase.

Following equation is applied to give a smooth transition of thermal conductivity between unfrozen and frozen state, as above-mentioned equations only estimate thermal conductivity under unfrozen and frozen conditions.

$$\lambda_T = (\lambda_f - \lambda_u) \times S_i / S_r + \lambda_u \tag{5.18}$$

where λ_f is thermal conductivity of frozen soil; and λ_u is thermal conductivity of unfrozen soil.

Heat capacity

The heat capacity of ice (1880 kJ/m^3°C) is smaller than water (4187 kJ/m^3°C). Similarly, the heat capacity of soil is the sum of the volumetric heat capacity of each component weighted by the respective volume (Johnston et al., 1981).

$$C_T = (1-n)C_{Tp} + nS_wC_{Tw} + nS_iC_{Ti} \tag{5.19}$$

where C_{Ti} is volumetric heat capacity of ice.

5.2.3 Mechanical properties

The pore ice bonds the surrounding soil particles, accordingly, the frozen soil becomes stiffer compared with unfrozen one. For the sake of simplicity, a linear relation is given as below

$$E = f(S_i) = S_i(E_f - E_u) + E_u \tag{5.20}$$

5.3 SFCC AND ITS DEPENDENCE ON TOTAL WATER SATURATION

5.3.1 SFCC derived from SWCC

The relation between degree of saturation and suction is formulated by van Genuchten and Mualem (VGM) model.

$$S_w = S_w(\psi) = (S_{rs} - S_{rr})\left(1+(\alpha\psi)^{\lambda}\right)^{(1-\lambda)/\lambda} + S_{rr} \tag{5.21}$$

Equation 5.22 presents the relationship between cryogenic suction and negative temperature, where coefficient n is 1.0 for sorptive forces govern soil (designated SLS soils for solid-liquid-

solid contact, e.g. clays) and 2.2 for capillary forces govern soils (designated SS soil for solid-solid contact between particles, e.g. sand and silt).

$$\psi = n\frac{L\rho_w}{T_0}T \tag{5.22}$$

where T_0 is nominal freezing temperature, 273.15 unit in Kelvin.

Substituting Equation 5.22 into Equation 5.21, then we obtain the relationship between S_r and negative temperature T for saturated, which gives in the form of,

$$S_w = S_w(T) = (S_{rs} - S_{rr})\left(1+\left(\alpha n\frac{L\rho_w}{T_0}T\right)^{\lambda}\right)^{(1-\lambda)/\lambda} + S_{rr} \tag{5.23}$$

The partial derivative of S_r with respect to T shows below, as a transient process varies with time and incremental scheme (Δt) is applied.

$$\frac{\partial S_w}{\partial T} = (S_{rs} - S_{rr})\alpha n\frac{L\rho_w}{T_0}(1-\lambda)\left(1+\left(\alpha n\frac{L\rho_w}{T_0}T\right)^{\lambda}\right)^{(1-\lambda)/\lambda-1}\left(\alpha n\frac{L\rho_w}{T_0}T\right)^{\lambda-1} \tag{5.24}$$

Finally, we come to the S_w and T relationship in the incremental form.

$$\Delta S_w = \frac{\partial S_w}{\partial T}\Delta T \tag{5.25}$$

5.3.2 Dependence of SFCC on total water saturation

Dall'Amico et al. (2011) verified the van Genuchten SWCC can be combined with the Clapeyron equation to estimate saturation of liquid water in unsaturated soil subjected to the freezing process. The water saturation is in accordance with the total water saturation when soil is unfrozen. However, the temperature may also affect the water saturation as soil freezes. A depressed freezing temperature caused by pore-water pressure (suction) prior to freezing is obtained based on the Clapeyron equation in which the pore ice pressure is set as gauge pressure (Williams, 1964).

$$T_f = T_f(u_{w0}) = \frac{T_0}{L\rho_w}u_{w0} \tag{5.26}$$

where T_f is freezing point depression; and u_{w0} is pore-water pressure (suction) prior to freezing. Then the further pore-water pressure decrease is obtained during the subsequent freezing process.

$$\psi = \psi(T) = u_{w0} + \frac{L\rho_w}{T_0}(T - T_f)\times H_e(T - T_f) \tag{5.27}$$

where H_e is the Heaviside function.

Substituting Equation 5.27 into Equation 5.21, the water saturation is associated with both temperature and total water saturation.

$$S_w = S_w\left(T, u_{w0}\right) = \left(S_{rs} - S_{rr}\right)\left(1 - \left(\alpha u_{w0} + \alpha \frac{L\rho_w}{T_0}\left(T - T_f\right) \times H\left(T - T_f\right)\right)^{\lambda}\right)^{(1-\lambda)/\lambda} + S_{rr} \quad 5.28$$

5.4 ICE PRESSURE AND SEGREGATION CRITERION

Miller (1978) and O'Neill and Miller (1985) adopted a stress criterion to initiate ice segregation that is total pore pressure, weighted by water and ice pressure, should exceed overburden. Gilpin (1980) and Nixon (1991) applied a simpler separation pressure concept given in the form of

$$u_i = u_{ob} + u_{sep} \quad 5.29$$

where u_i is ice pressure; u_{ob} is overburden pressure; and u_{sep} is tensile strength of soil.

For calculation of ice pressure, Hopke (1980) and Mu and Ladanyi (1987) used an idealized distribution of temperature and ice pressure in which Clapeyron equation determines a linear variation of ice pressure along with negative temperature from freezing front to the base of freezing fringe. It is believed that this assumption estimates the profile of water and ice pressure close to phenomenon in saturated soil.

However, the accumulation of ice content in unsaturated soil is not necessarily dependent on temperature change, as inflow water driven by cryogenic suction gradient can be frozen under an isothermal phase change process. Another limitation is that ice pressure generates only if the soil is saturated. (Guymon et al., 1980) In present study, we assume ice pressure is function of ice content regardless of temperature to overcome sudden change of ice pressure when soil transfers from unsaturated to saturated state. The ice pressure remains constant when it is equal to sum of overburden pressure and tensile strength of soil.

$$u_i = u_i\left(S_i\right) = \frac{1}{\alpha}\left[\left(\frac{\left(1 - S_i\right) - S_{rr}}{S_{rs} - S_{rr}}\right)^{\frac{\lambda}{1-\lambda}} - 1\right]^{\frac{1}{\lambda}} \le u_{ob} + u_{sep} \quad 5.30$$

where u_{ob} is overburden pressure; and u_{sep} is tensile strength of soil.

Finally, pore-water pressure of freezing soil is determined by the following equation,

$$u_w = u_i - \psi \quad 5.31$$

5.5 MODELING OF FROST HEAVE AND THAW SETTLEMENT

5.5.1 Frost heave

The frost heave modeling here is a straightforward interpretation of observed test results. The frost heave phenomenon is formulated on a macro viewpoint for a field-scale application purpose. Thus, the sophisticated physical modeling of discrete ice lens and the frozen fringe is avoided.

The heaving only occurs when the combination of volumetric content of pore water and pore ice exceeds the porosity of soil (Mu and Ladanyi, 1987).

$$\varepsilon_f = 0.09\left(\theta_0 + \triangle\theta - \theta_u\right) + \triangle\theta + \left(\theta_0 - n\right) \qquad 5.32$$

where θ_0 is initial volumetric water content pre-freezing; and $\Delta\theta$ is increment of water content by moisture migration.

5.5.2 Thaw settlement

The phase transition of absorbed water separates soil skeleton where ice lens generates, while consolidation may occur in the unfrozen zone due to water migration to freezing front. When frozen soil is thawed, some of these deformations is recoverable, but some are not, since soil is a type of elastoplastic geomaterial. Avoiding discussion on complex mechanism of thawing process, thaw settlement is determined by a simple experimental equation and given as,

$$\varepsilon_t = \omega\varepsilon_f = \left(c + d\ln\sigma_n\right)\varepsilon_f \qquad 3.74$$

5.6 SUMMARY ON FURTHER DEVELOPED MODEL

The proposed model is a multi-filed coupled model with three fields in which one governing equation controls behavior in each field. The interactions between fields can be classified into two levels. The first level includes terms in governing equation which reflects influence of another field on behavior in this filed, as arrows shown in Figure 5.1.

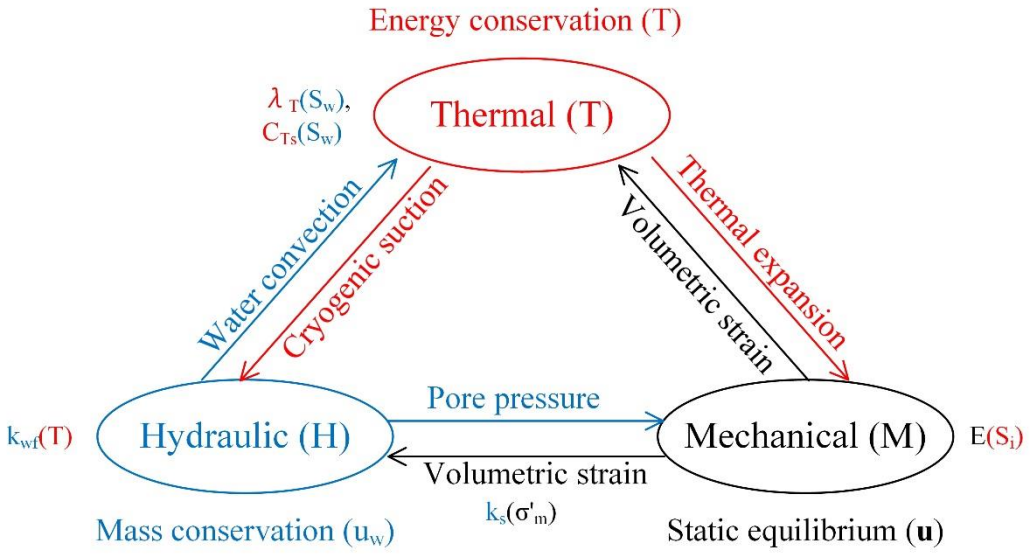

Figure 5.1 Schematic interpretation of THM coupling

For example, lowering of temperature freezes water and causes cryogenic suction in the hydraulic field, while water convection also contributes to heat transfer in thermal field. The second level

is influence of soil property in one field on that in another field, as soil properties shown in Figure 5.1. For instance, thermal properties like heat capacity and thermal conductivity depend on liquid water saturation or solid ice saturation.

5.7 MODEL VALIDATION 1: SIMULATION ON FROST HEAVE (SILT SOIL)

5.7.1 A representative frost heave test

A closed-system frost heave test is selected to illustrate the features of the model. A specimen is frozen from bottom-up with a drop of temperature from 0 to -3 °C for 15 hours, while the top temperature remains 0.1 °C. Applied overburden pressure is 10 kPa, and no water supply is available.

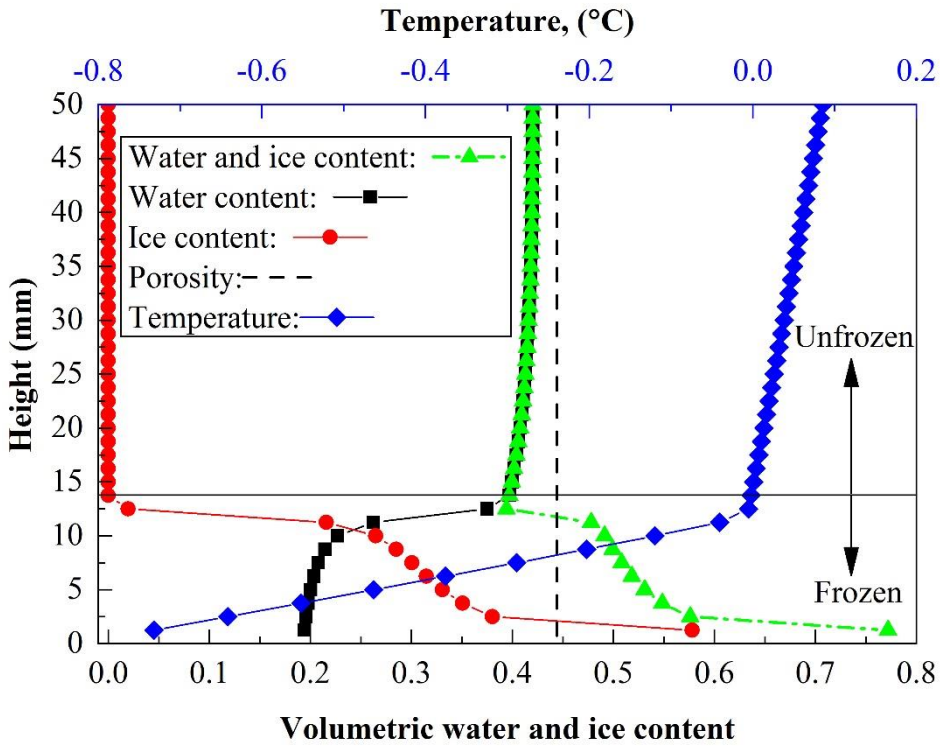

Figure 5.2 Volumetric total water content, and temperature profile

Figure 5.2 presents the temperature profile and volumetric water and ice content profile after 5 hours freezing. It is obvious that the temperature gradient (slope of curve) in frozen zone is much larger than that in unfrozen zone, as the thermal conductivity increased when soil is frozen, and water is transferred into ice. In unfrozen zone, the ice disappears and total content (water and ice) is always coincidence with water content. On the contrast of that, the water content decreases rapidly in frozen zone due to phase change of liquid water. However, the corresponding ice content increment alone cannot let the total water and ice content exceed the porosity. The reason is that frost heave occurs right behind freezing front. The inflow water driven by cryogenic suction

gradient feeds the ice formation which leads a rapid increase of total content behind freezing front. In the meantime, the phase change of this inflowing water consumes large amount of latent heat, as a result, the advance of freezing front is suppressed to some extent. Only if large enough heat budget is given to freeze inflow water, the remaining cooling could further lower the temperature and advance the freezing front.

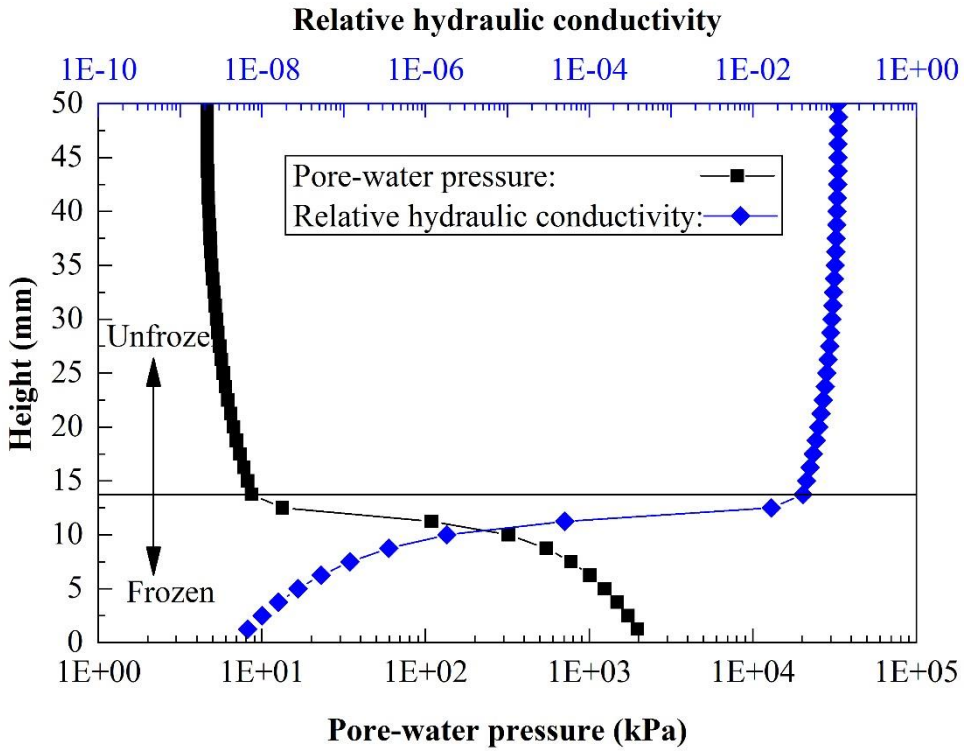

Figure 5.3 Pore-water pressure and relative hydraulic conductivity profiles

Pore-water pressure and relative hydraulic conductivity profiles after 5 hours of freezing are illustrated in Figure 5.3. Pore-water pressure increases rapidly right behind freezing front which is driven force of water migration towards freezing front. However, we should note that the relative hydraulic conductivity also decreases rapidly in this zone. The expected combination of these two factors causes observed large increment of total content in the adjacent of freezing front in Figure 5.2. One more point is that relative hydraulic conductivity decreases faster than increase of pore-water pressure, then further ice formation is not observed in the deeper frozen zone.

Figure 5.4 presents volumetric water and ice content profiles and frost heave ratio relationship. As freezing time goes by, the water content in the unfrozen zone decreases gradually since this is a closed-system test and no additional water supply is available. At early time of freezing (2.5h and 5h cases), the large total content accumulation is observed, which exceeds porosity and causes faster frost heaving. As the water content in unfrozen zone is lower, and reduced permeability is not large enough to transport water to freezing front and saturate it, therefore, frost heave develops very slow in the late stage of freezing.

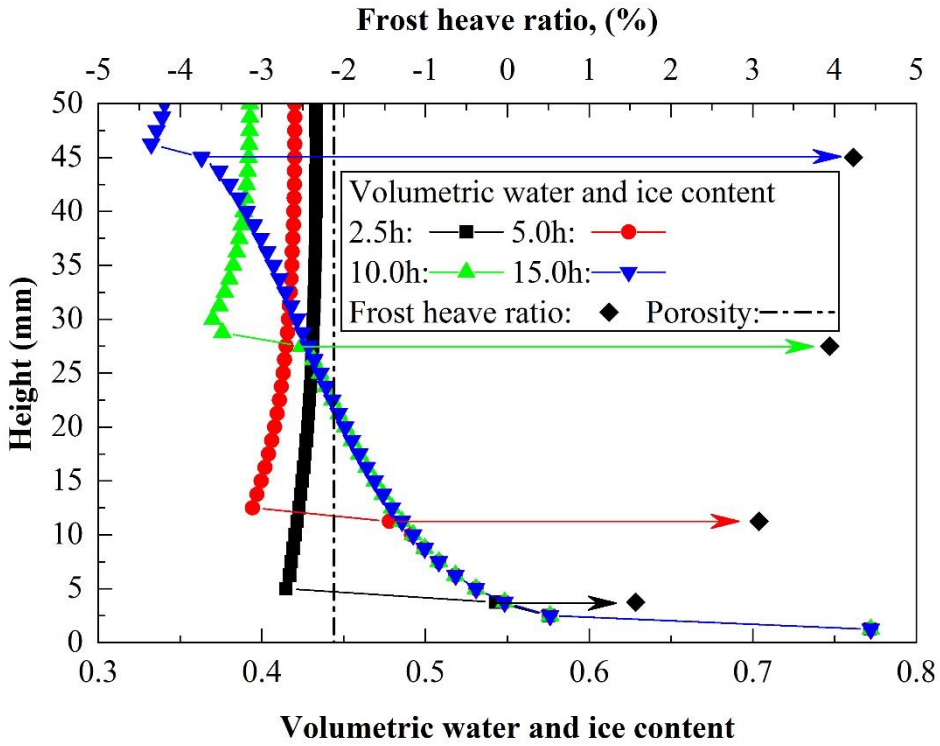

Figure 5.4 Volumetric water and ice content profile and frost heave ratio relationship

5.7.2 Performance of model for saturated case

Figure 5.5 shows the correlation of water migration and frost heave strain for open-system frost heave test. The proposed model well simulates this correlation in which sufficient water supply is the key factor for ice growth and frost heave.

Figure 5.6 and Figure 5.7 present influence of overburden pressure for open-system frost heave test. The larger the overburden pressure the smaller the frost heave and thaw settlement.

Generally, the new model predicts frost heave better compared with performance of old model. Although Equation 3.60 to Equation 3.62 are applied both in new and old model, the definition of S_w is slightly different. In old model, S_w is total saturation including liquid water and solid ice during freezing, that means total saturation may not change or even increases, although water saturation decreases. Therefore, hydraulic conductivity for freezing soil is mainly affected by Equation 3.65 in which the hydraulic conductivity of frozen soil is three orders of magnitude (0.001) smaller than unfrozen one. However, this operation may highly overestimate hydraulic conductivity for freezing soil that could be more than six orders smaller than unfrozen one in fact (Figure 5.3). On the contrary, the S_w is defined as liquid water saturation in new model, decreasing with temperature. The new model enables better prediction on frost heave since drawback of overestimation on hydraulic conductivity during freezing process is overcome. As a result, better prediction on thaw settlement is achieved.

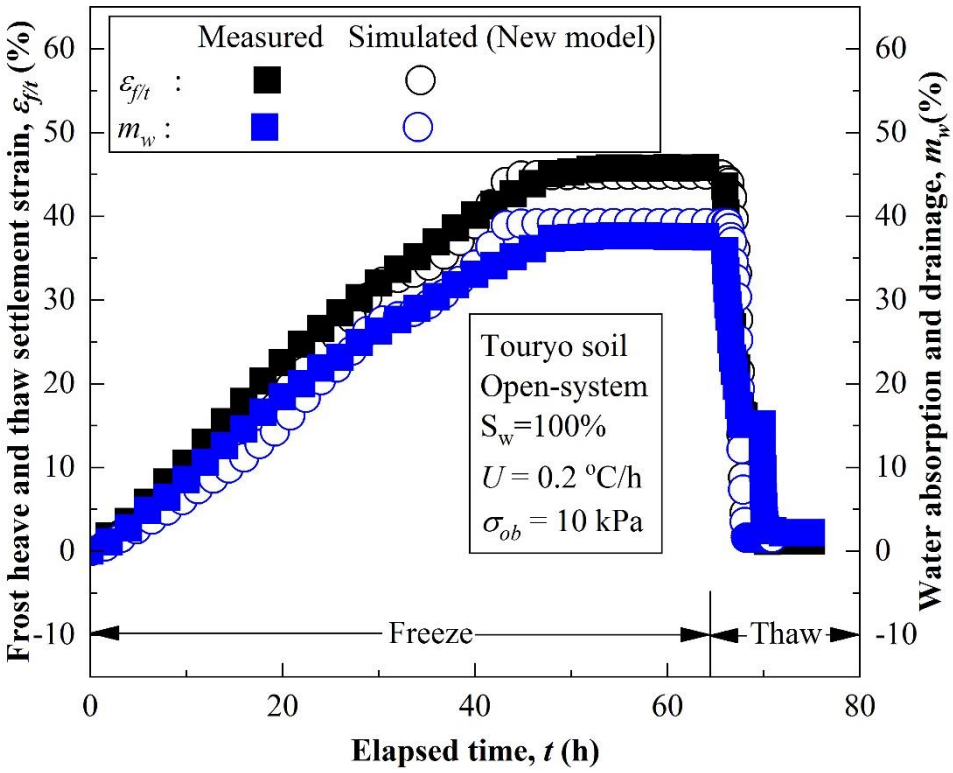

Figure 5.5 Simulation on correlation of water migration and frost heave

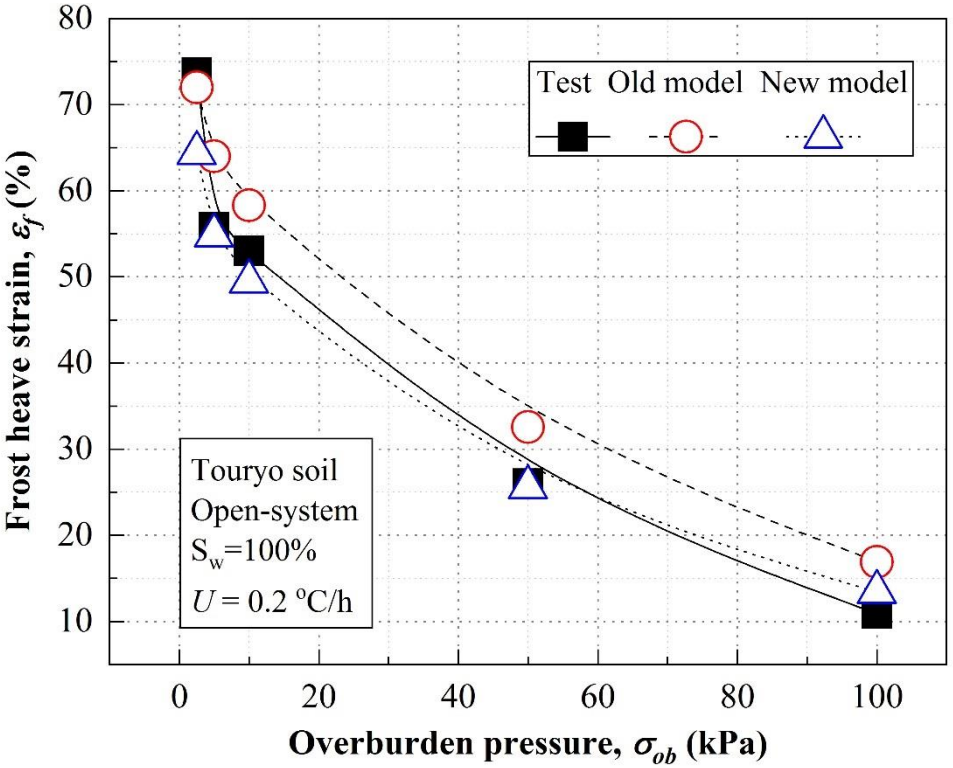

Figure 5.6 Simulation on influence of overburden for open-system: Frost heave

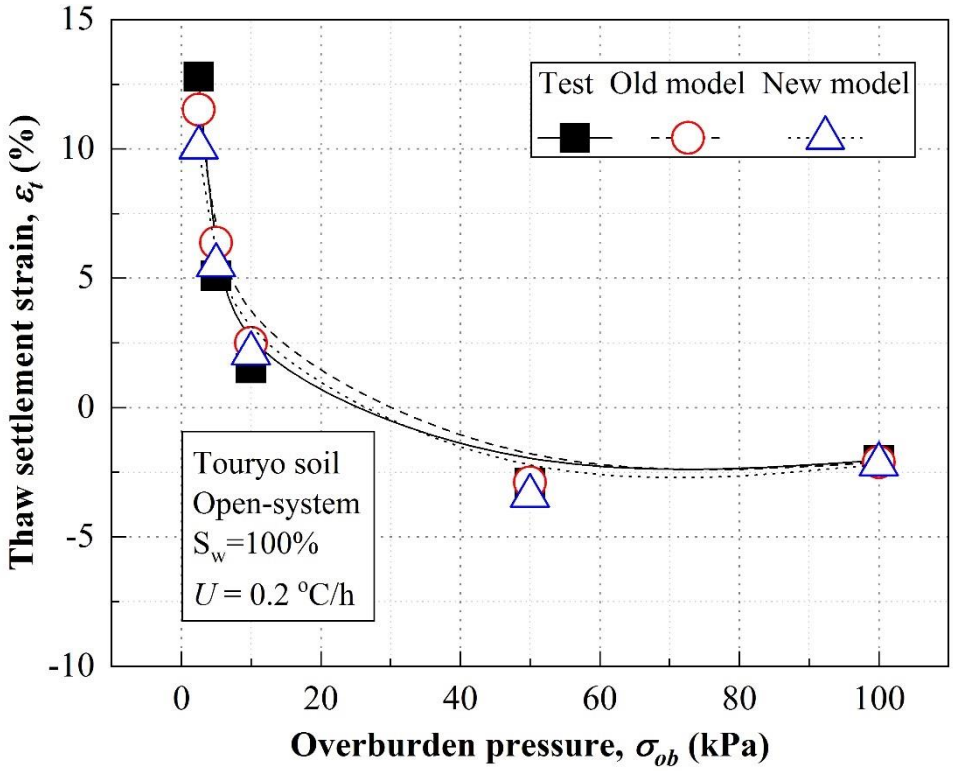

Figure 5.7 Simulation on the influence of overburden for open-system: Thaw settlement

Figure 5.8 and Figure 5.9 show the influence of cooling rate for open-system frost heave test. The faster freezing specimen, the smaller the frost heave.

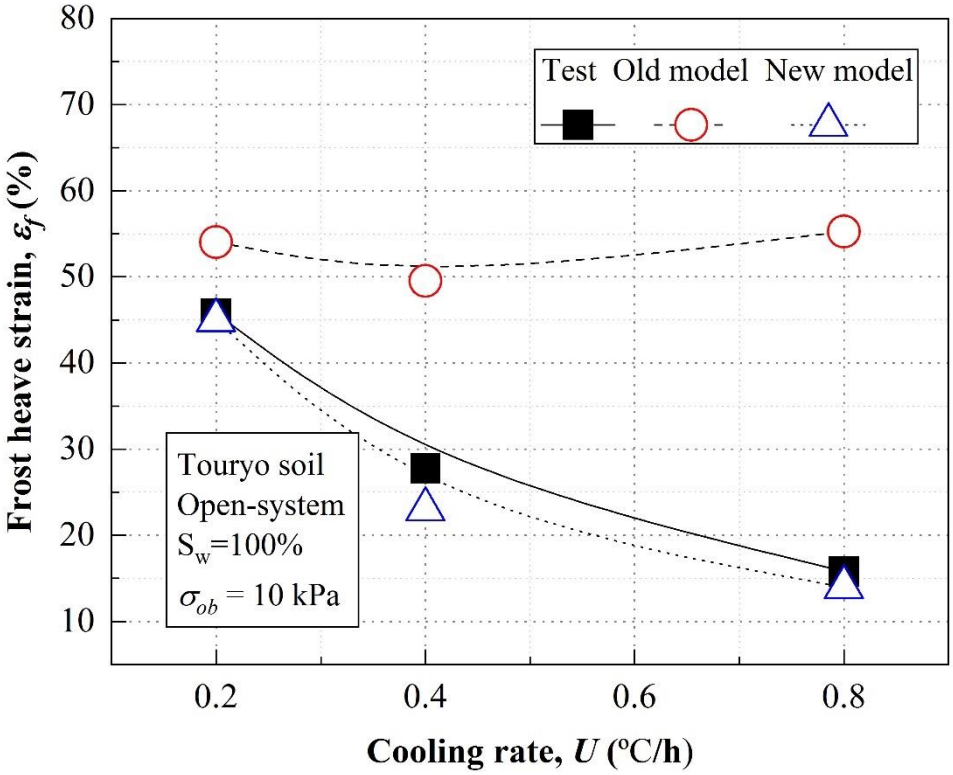

Figure 5.8 Simulation on influence of cooling rate for open-system: Frost heave

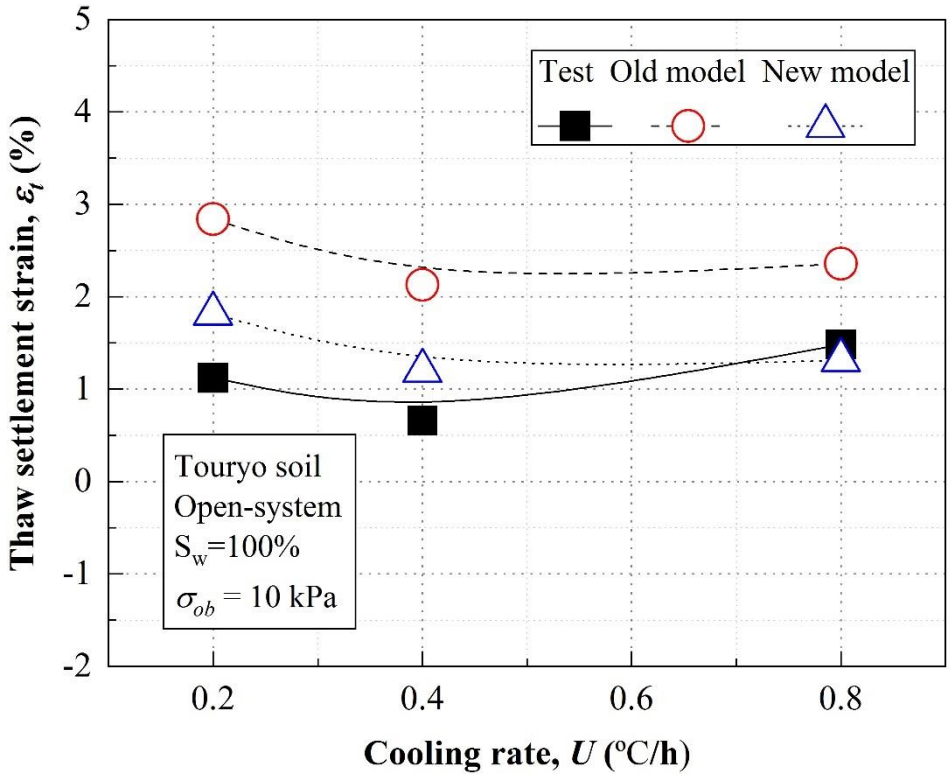

Figure 5.9 Simulation on influence of cooling rate for open-system: Thaw settlement

For high cooling rate case, the freezing front proceeds quickly from cold end to the warm end of specimen. The latent heat of inflow water is not able to consume all the heat budget provided by heat conduction from cold end, thus the forward speed of freezing front cannot be delayed effectively as compared with lower cooling rate case. State it in another way, the quick freezing not allowing enough time for water migration and ice growth. As for overestimation given by old model, experimental Equation 3.73 dominates the development of frost heave. However, none of parameters in that equation capture contribution of cooling rate, accordingly, it fails to predict frost heave correctly.

5.7.3 Performance of model for unsaturated case

Figure 5.10 and Figure 5.11 presents the influence of overburden pressure on frost heave for closed-system frost heave test. Generally, the larger the overburden pressure the smaller the frost heave and thaw settlement. The mechanism is that the larger ice pressure is required to initiate separation of soil skeleton for larger overburden pressure case, consequently, the smaller pore-water pressure is achieved for the given suction (subfreezing temperature) according to Equation 5.31. However, the frost heave in open system case is much larger than that in closed-system case with identical overburden pressure, as free water supply feeds the ice accumulation. As illustrated in Figure 5.2, for closed-system case, frost induced water redistribution allows water movement towards freeing front to feed ice formation and growth. As a result, the unfrozen zone in upper

side of soil column is desaturated, that also means unfrozen zone of an initial saturated column will become unsaturated in subsequent freezing process.

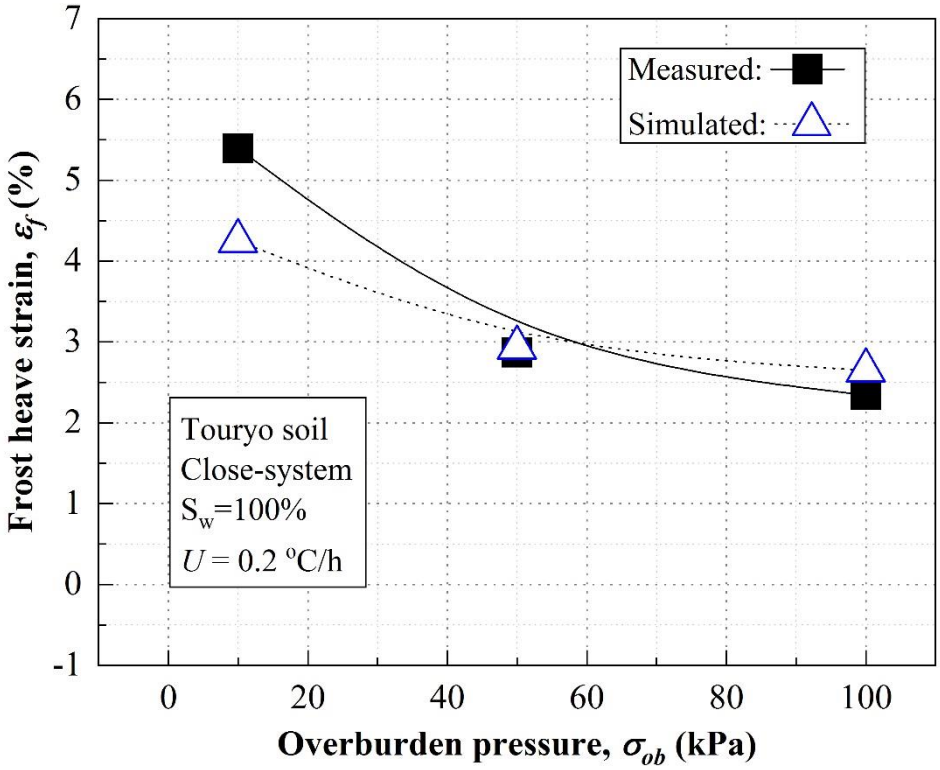

Figure 5.10 Simulation on influence of overburden for closed-system: Frost heave

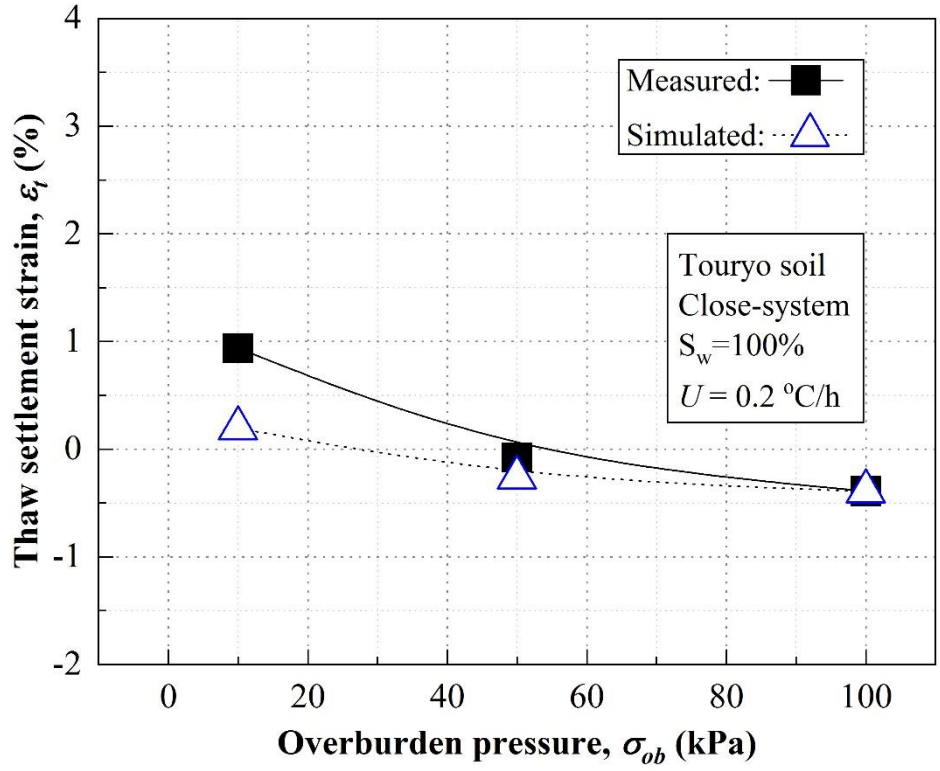

Figure 5.11 Simulation on influence of overburden for closed-system: Thaw settlement

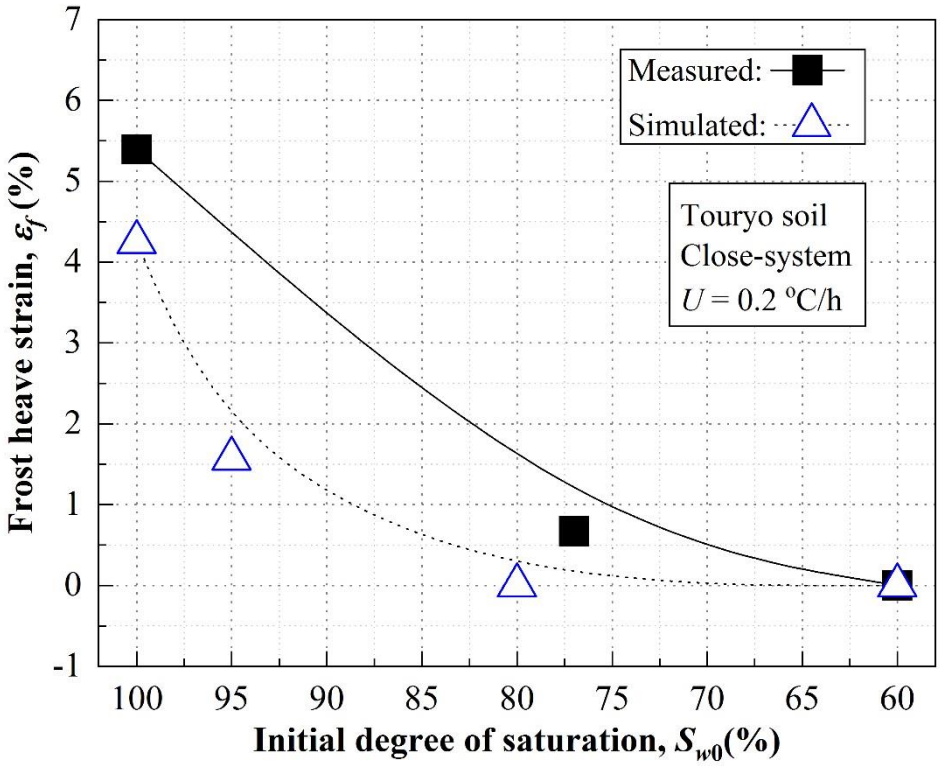

Figure 5.12 Simulation on influence of initial saturation for closed-system: Frost heave

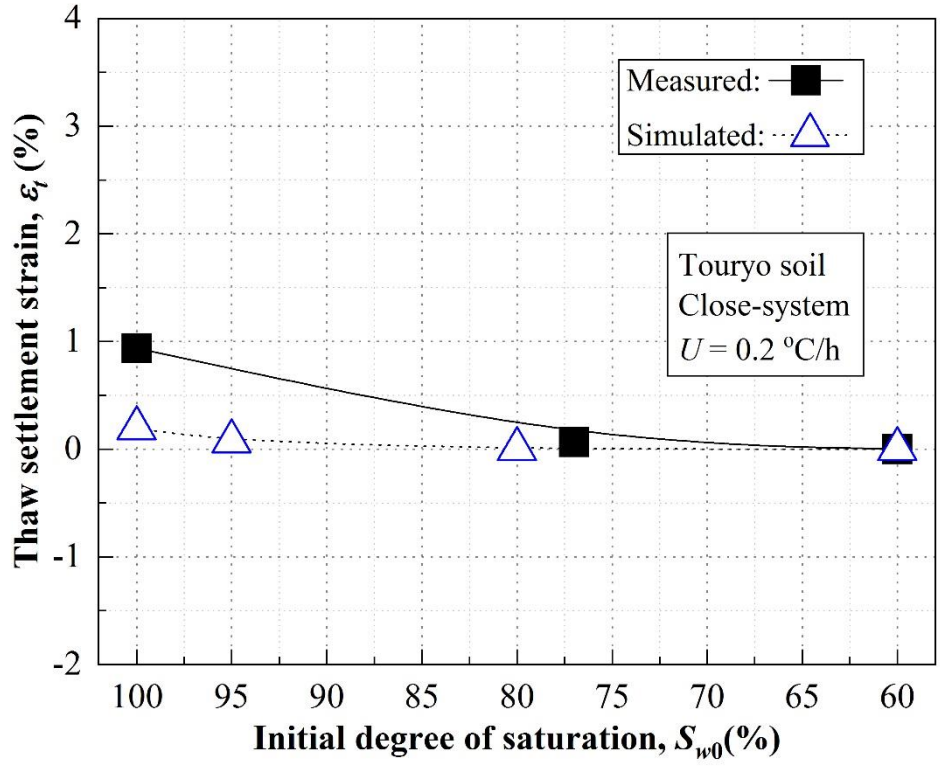

Figure 5.13 Simulation on influence of initial saturation for closed-system: Thaw settlement

Figure 5.12 and Figure 5.13 present the influence of the initial degree of saturation on frost heave. The larger initial degree of saturation, the larger frost heave. The soil does not appear to heave

when initial degree of saturation lower to 80%, as redistributed water is still not enough to full soil pores and generate enough ice pressure to separate soil skeleton.

5.7.4 Remarks

The following conclusions can be drawn from this study:

1. The new model is able to comprehensively capture main features of unsaturated freezing soil like suction induced freezing point depression, water-ice phase change, water redistribution caused by cryogenic suction gradient, and most importantly, the frost heave and thaw settlement of soil.

2. The validity of the model is examined by comparing simulated frost heave and thaw settlement with experimental results. Generally, the model predicts the frost heave and thaw settlement amount under various test conditions well. The effect of overburden pressure, water supply condition, initial degree of saturation and freezing rate on frost heave have been reproduced by proposed model.

5.8 MODEL VALIDATION 2: SIMULATION ON THAW SETTLEMENT (CLAY SOIL)

5.8.1 Frost heave test

The open-system frost heave test performed in SEIKEN cooperation is selected to verify the performance of the proposed model for frost heave and thaw settlement prediction. The test material is Fujinomori soil, which is classified as silty clay with medium frost susceptibility. The test soil is prepared as a slurry and consolidated under 1 MPa, then the specimen is trimmed as 40 mm in height and molded. The specimen is frozen form bottom-up and water is absorbed from the top end into the specimen to feed the growth of ice lens and generate the observed frost heave. The frost heave amount (displacement), water absorption and drainage, pedestal and top plate temperature are recorded. The typical test results for one-dimensional frost heave test are shown in Figure 5.14 and Figure 5.15.

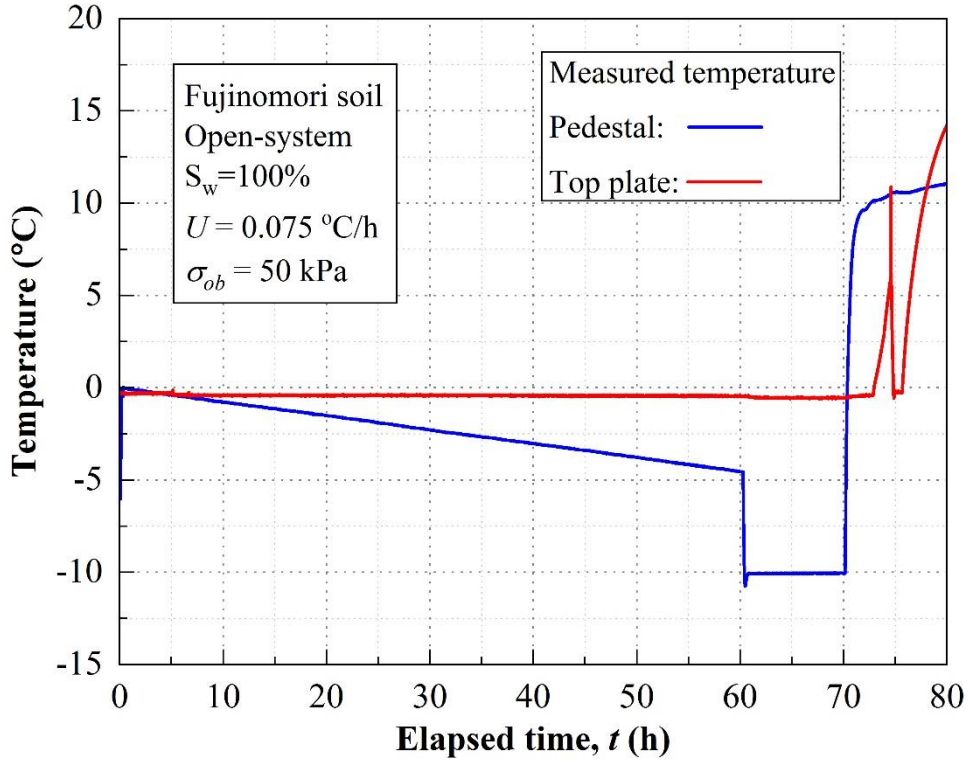

Figure 5.14 Time history of the pedestal and top plate temperature

Tests were performed under various overburden pressure, namely 50, 100, 400 kPa, along with test results, summarized in Table 5.1.

5.8.2 Simulation on frost heave test

Input parameters

The input parameters for analysis are listed in Table 5.2. The permeability of saturated soil and SFCC are tested for Fujinomori soil (Tokoro et al., 2016). All the other necessary inputs are

referred to as common values for soil properties.

Table 5.1 Summarization of test conditions and results of Fujinomori soil

Overburden pressure (σ_{ob}) Mpa	0.051	0.100	0.401
Initial height of sample mm	39.41	39.29	39.52
Porosity (n)	0.459	0.454	0.449
Freezing rate mm/hour	1.084	1.028	0.859
Cooling rate (U) °C/hour	-0.075	-0.065	-0.060
Frost heave (ε_f) %	16.365	12.572	2.174
Water absorption (m_w) %	11.925	8.348	-0.833
Thaw settlement (ε_t) %	2.613	1.807	-0.046

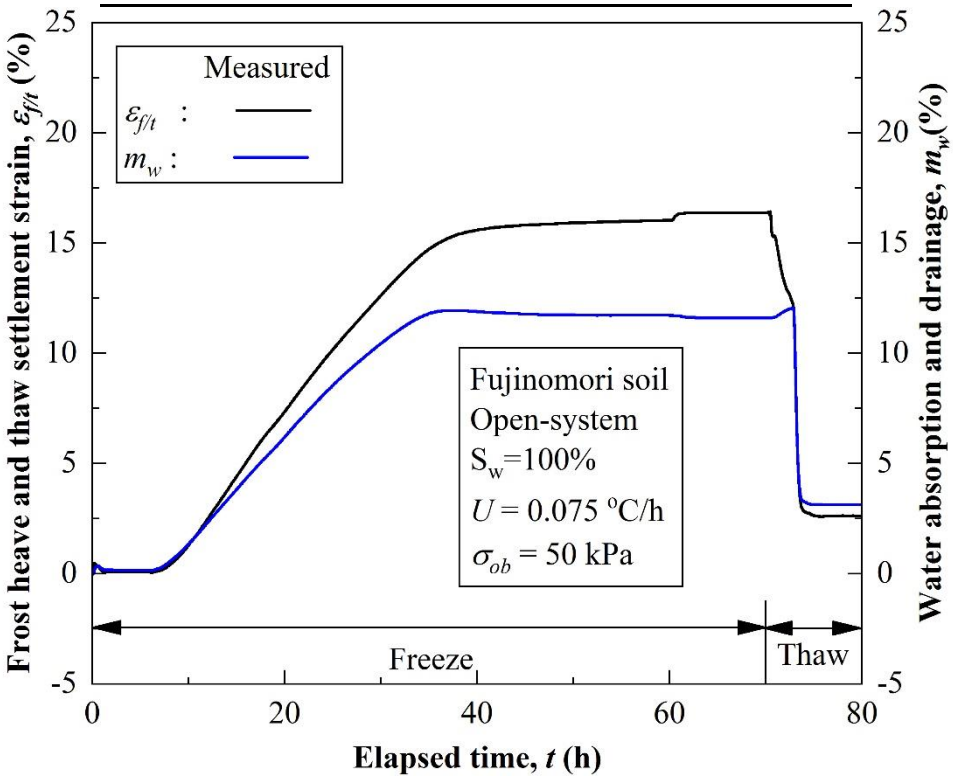

Figure 5.15 Frost heave and water absorption

The coefficient of thaw settlement under various overburden pressure is determined by Equation 3.74 based on test results listed in Table 5.1. Figure 5.16 shows the relationship between the thaw settlement coefficient and overburden pressure. The smaller the overburden pressure, the larger the thawing settlement.

Boundary conditions

The boundary conditions of each field are shown in Figure 5.17 and Figure 5.18. One dimensional frost heave test is simulated in which soil specimen is frozen bottom-up, while water absorbed into soil from top end.

Table 5.2 Input parameters in frost-heave test analysis of Fujinomori soil

Parameters	Values
Dry density of soil (ρ_d) kg/m^3	1460
Porosity (n)	0.455
Thermal conductivity of soil particles (λ_s) W/m°C	0.83
Thermal conductivity material parameter (χ)	0.75
Thermal conductivity material parameter (η)	1.20
Thermal conductivity empirical parameter (κ) unfrozen/ frozen	1.90/0.85
Volumetric heat capacity of soil particles (C_{Tp}) J/m^3°C	1.3E+6
van Genuchten-Mualem fitting parameter (α) 1/MPa	1.904
van Genuchten-Mualem fitting parameter (λ)	1.865
Saturated degree of saturation (S_{rs}) %	100.0
Residual degree of saturation (S_{rr}) %	18.50
Saturated water hydraulic conductivity (k_s) m/s	5.0E-10
Impedance factor (Ω)	7
Young's modulus of soil (E) MPa	12.5
Poisson's ratio (υ)	0.33
Thaw settlement fitting parameter (c)	1.100
Thaw settlement fitting parameter (d) 1/MPa	0.092

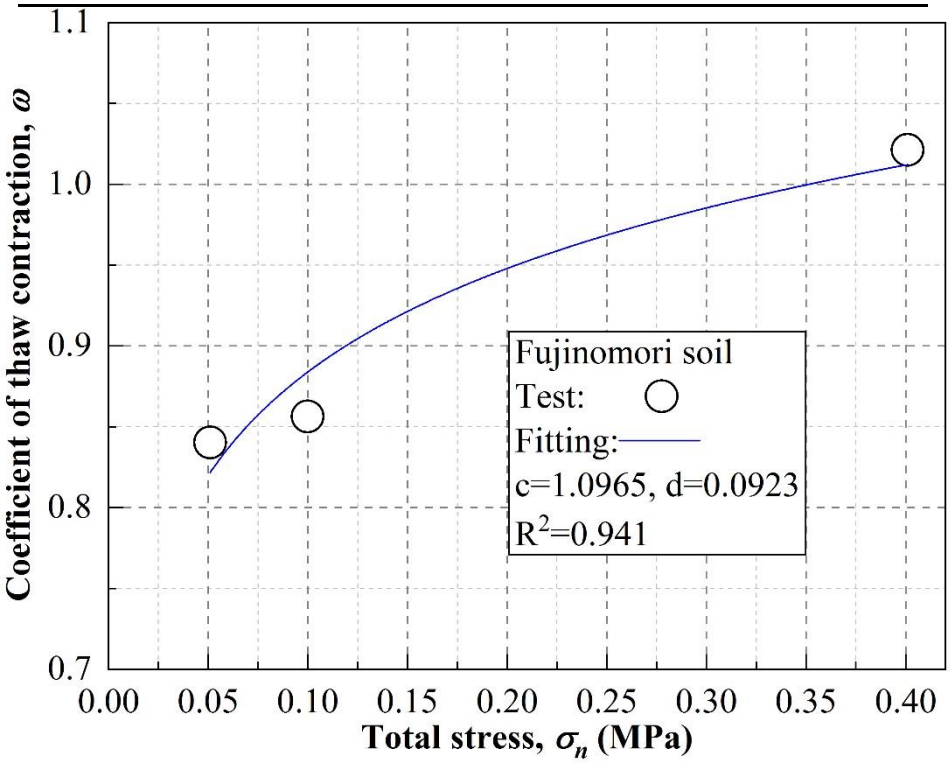

Figure 5.16 Determination of thaw settlement coefficient

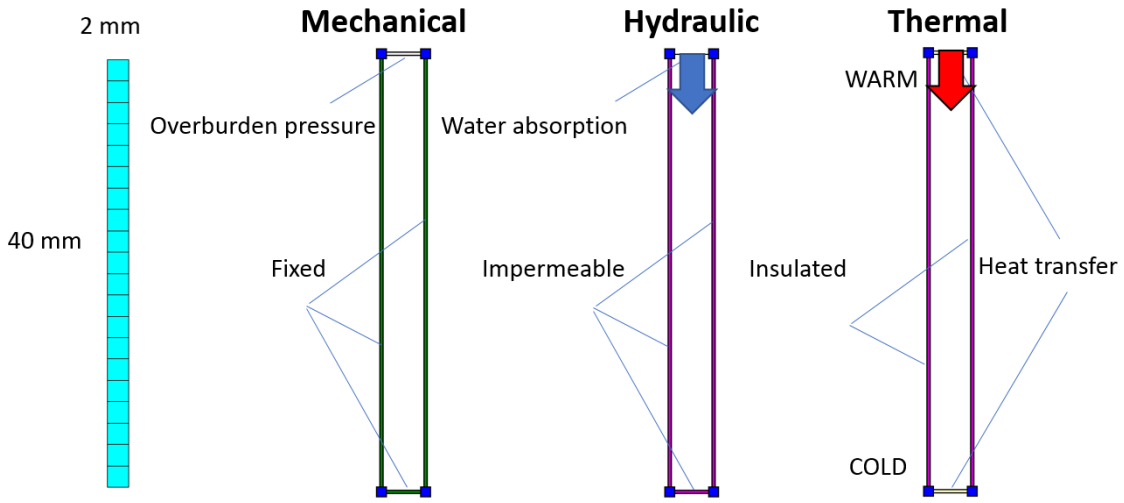

Figure 5.17 Boundary conditions - open system (freezing)

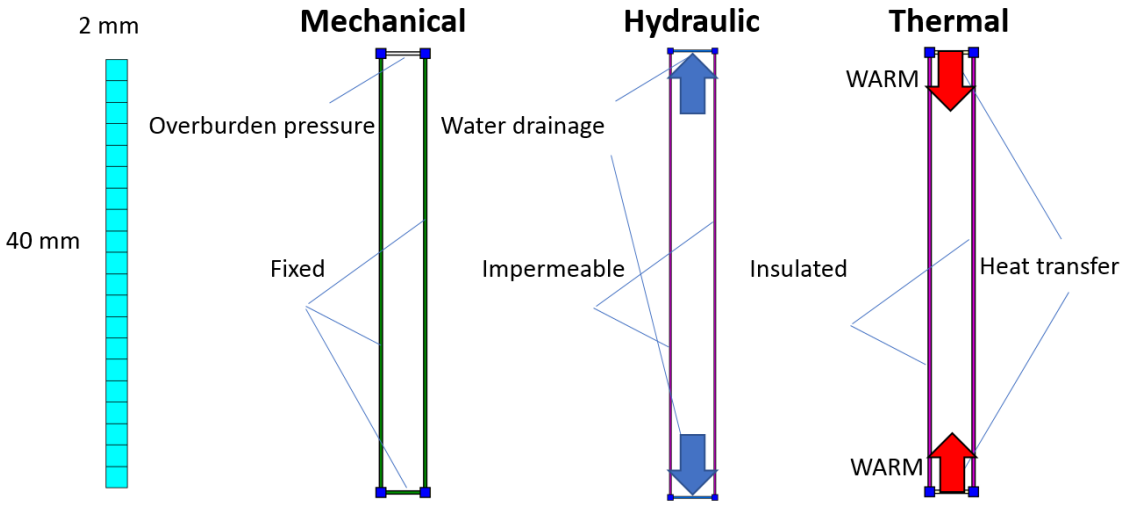

Figure 5.18 Boundary conditions - open system (thawing)

5.8.3 Results and discussions

Correlation between frost heave and absorbed water

The correlation between frost heave and absorbed water is correctly reproduced. Both the trend and the amount of simulated frost heave reasonably match with the measured one well. (Figure 5.19)

Influence of permeability after freeze-thaw

The program can change the saturated permeability after a freeze-thaw cycle. If the temperature changes from a negative value to a positive one, the program treats this as the completion of one freeze-thaw cycle and assign the larger permeability. The change of permeability after freeze-thaw cycle does not affect the freezing process and not affect residual deformation either. The larger the permeability, the shorter the duration of the consolidation process (Figure 5.20). The

consolidation duration will be highly overestimated if change of permeability due to freeze-thaw is not well considered.

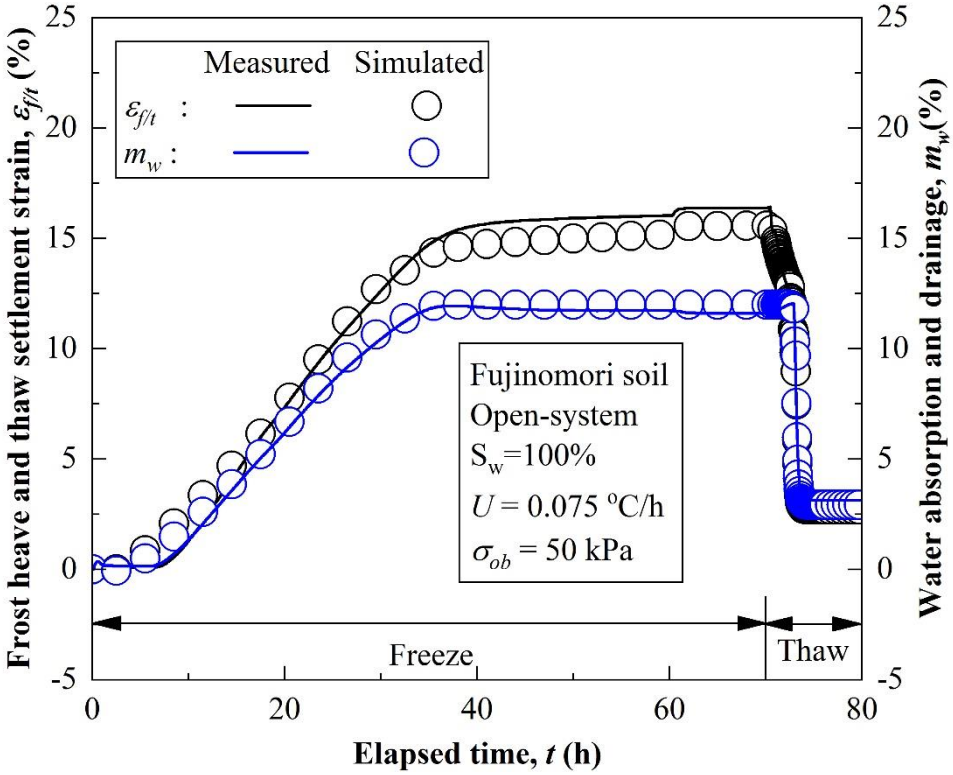

Figure 5.19 The relationship between frost heave and water absorption

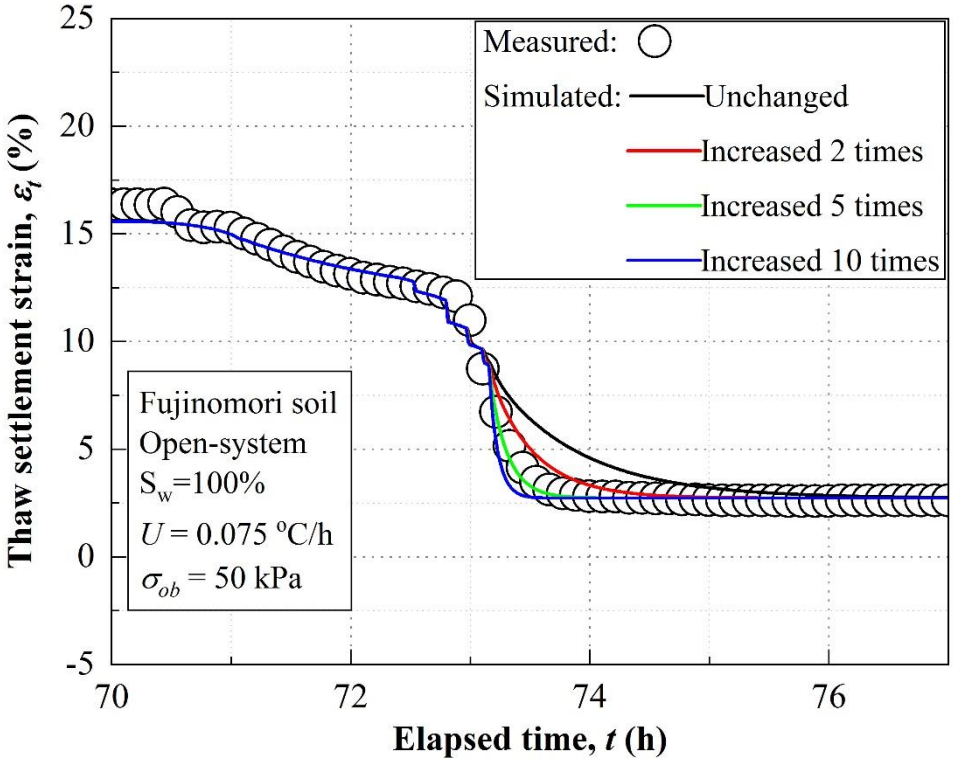

Figure 5.20 Influence of permeability on consolidation

Correlation between thaw settlement and drained water

The correlation between thaw settlement and drained water is correctly reproduced. Both the trend and the amount of simulated thaw settlement agree with the measured one (Figure 5.21). Thaw settlement can be divided into two stages. First, the ice-water phase change causes 9% volumetric shrinkage while water drainage does not happen. In this process, excess pore-water pressure accumulates. Then, thaw settlement develops gradually with water drainage and dissipation of excess pore-water pressure.

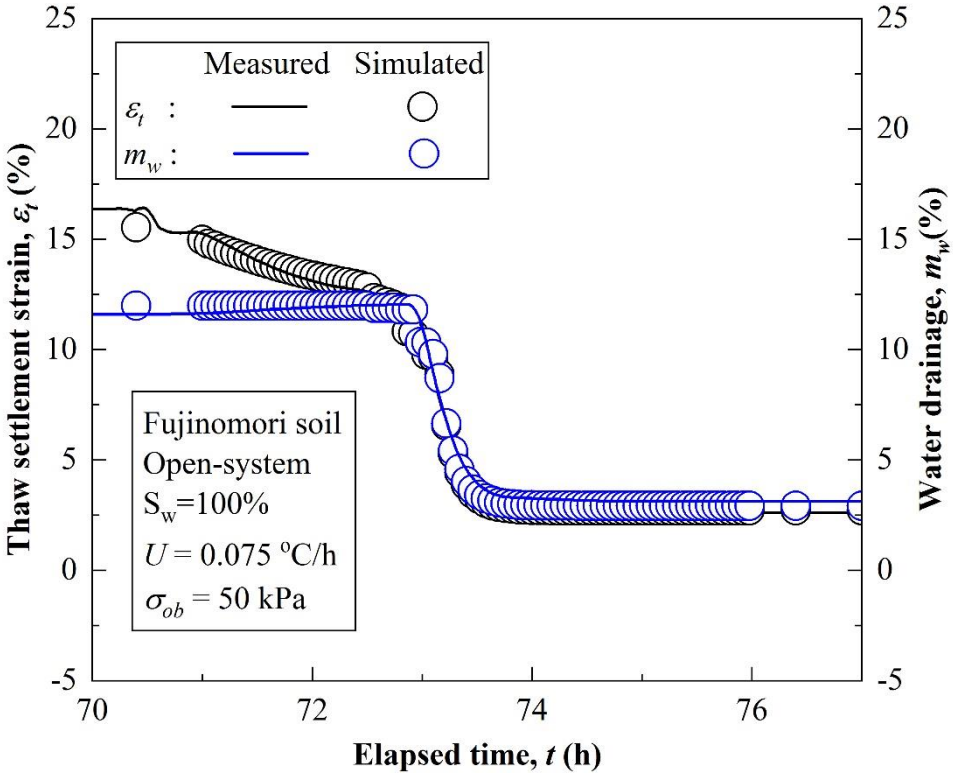

Figure 5.21 Relationship between thaw settlement and water drainage

The influence of overburden pressure on frost heave

Figure 5.22 presents a comparison between simulated and measured results for 100 kPa overburden condition. To compare with Figure 5.19, 50 kPa case and 100 kPa case share similar freeze-thaw behaviors, however, the larger the overburden pressure, the smaller the frost heave and water absorption, correspondingly, the smaller the thaw settlement.

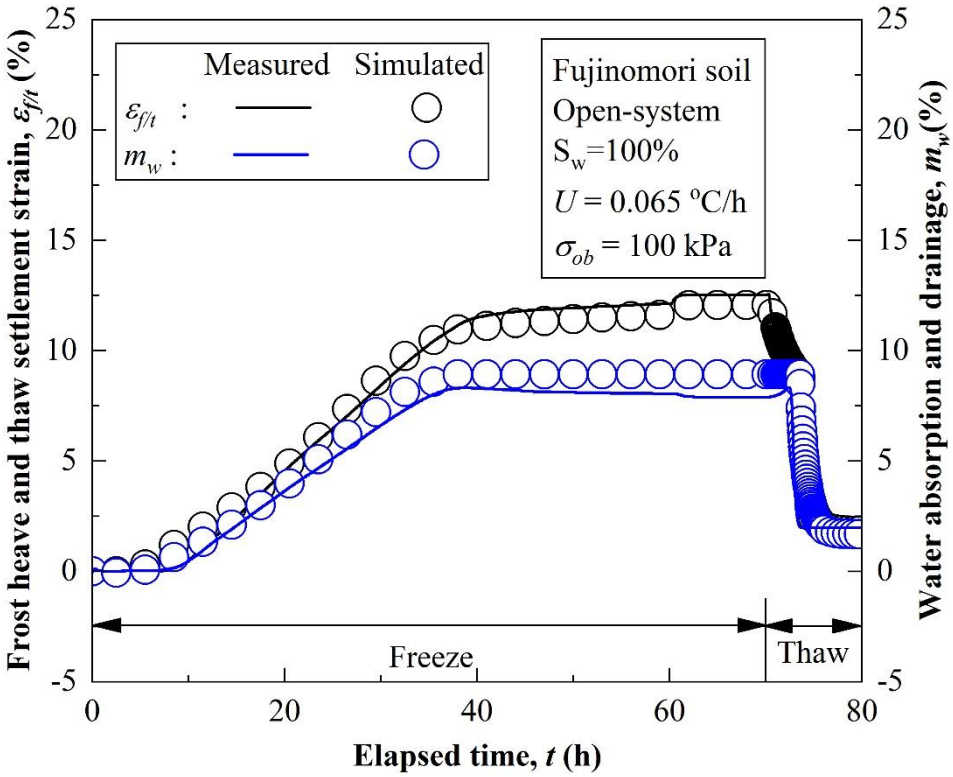

Figure 5.22 The influence of overburden pressure on frost heave

5.8.4 Remarks

The proposed model can reproduce the freeze-thaw behavior for clay soil. The frost heave and thaw settlement can be estimated quantitatively. The correlation between thaw settlement and water drainage are well reproduced. The permeability change due to freeze-thaw should be accounted for, otherwise, elapsed time for thawing process will be unrealistically extended.

5.9 MODEL APPLICATION: SIMULATION ON SOIL SLOPE

5.9.1 Problem statement

For soil slope in cold region, frost heave in winter causes uplift of surface soil while subsequent thaw settlement leads in the downslope movement of soil mass, this phenomenon is termed as solifluction (Higashi and Corte, 1971). The laboratory model test is conducted to simulate this soil mass movement process (Harris et al., 2001), together with field measurement (Matsuoka and Moriwaki, 1992). The relationship between mass movement and significant factors are studied including frost heave, ground ice, moisture contents, pore-water pressure and undrained shear strength during thawing (Matsuoka, 1998; Matsumoto et al., 2010; Harris et al., 1995 and 2008). All these previous studies provide us enlightening in mechanism of solifluction process, although it is often carried out for slopes in high mountain and permafrost areas. From an engineering standpoint of view, the progressive damage may also take place for soil slope in season cold region, which draws concerns on safety and stability of earth structure. For example, slope collapse may occur induced by accumulation of downslope movement along with freeze-thaw cycles. The long-term monitoring on freeze-thaw actions of instrumented slope is performed to investigate countermeasure like vegetation reinforcement, which reveals that frost heave generates along heat flow direction and thaw settlement develops in gravity direction (Ueno et al., 2010; Rui et al., 2018). Li et al. (2014 and 2015) performed experimental and numerical investigations on frost damage of a canal in seasonally frozen region, in which frost induced water redistribution and freeze-thaw deformation are simulated for a model test. However, some limitations exist as pointed out by authors like assumption on isotropic volumetric expansion of frost heave and simplified air temperature boundary condition. The isotropic expansion assumption may enlarge simulated deformation in horizontal direction, what is more important, the gravitational thaw settlement pattern is not noted by author. In this study, freeze-thaw behavior of slope is main interests of author together with unique frost heave and thaw settlement pattern.

A long-term field monitoring on freeze-thaw action of a soil slope was conducted for 5 years in Hokkaido, Japan. (Ueno et al., 2010) The size of the experimental slope is about 38 m in length, 2.0 to 2.8 m in height, and slope ratio is 1: 1.2. A paved road is constructed at the top of this cut slope. The experimental slope was divided into several sections to study the effects of various vegetations on the freeze-thaw action of slope. In each section, three measuring targets were placed along the slope surface in upper, middle and lower part of slope respectively, thereby the deformation perpendicular and parallel to slope surface were monitored continuously. A freezing depth meter was instrumented in middle of slope and the maximum measuring depth is 1 m. Two thermal couples were installed besides freezing depth meter at slope surface and 30 cm depth (Figure 5.23).

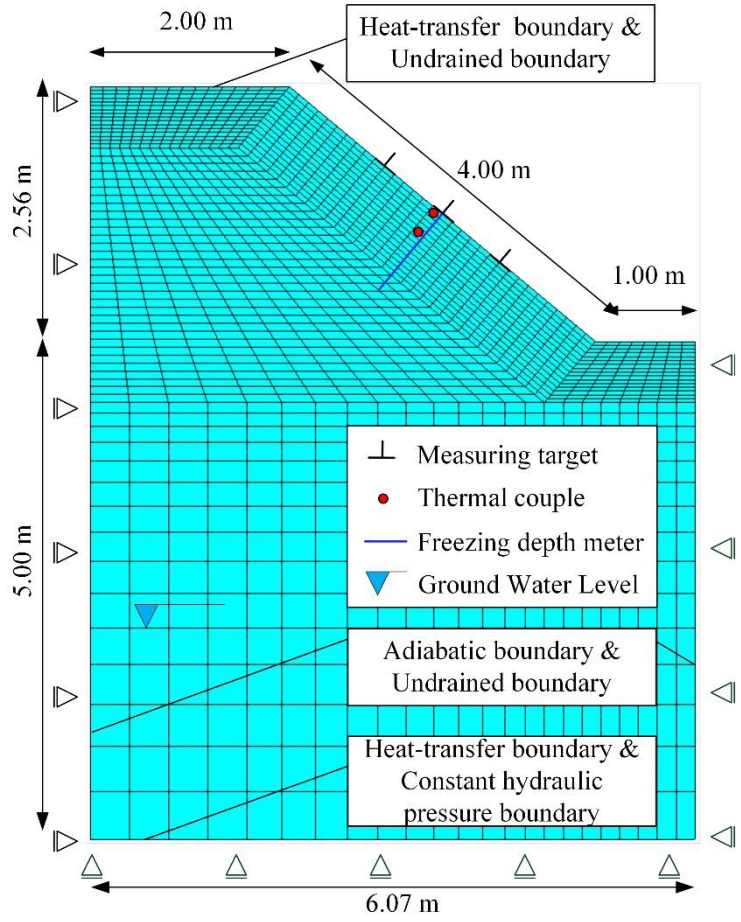

Figure 5.23 Size, instrument configuration, mesh and boundary conditions of slope

One section of the experimental slope is selected for simulation with 2.56 m in height and a slope length 4.00 m. The shoulder and toe of slope extend 2 m and 1 m respectively to eliminate boundary effects. The ground depth is set as 5 m to appropriately reproduce ground temperature field. The fine elements are assigned to the shallow layer close to slope surface where is severely affected by temperature boundary. This operation also benefits to accurate analysis on temperature change, water migration and relating deformation. Relative coarse elements are meshed for region far away from surface boundary to achieve balance between accuracy and computation time. The subsurface elements are intentionally arranged parallel to slope surface, which is convenient to extract the nodal information like displacement and temperature at given locations. Four nodes quadrilateral element are assigned to entire domain with 1792 nodes and 1705 elements in total.

5.9.2 Soil properties

Slope soil is a volcanic soil composed of 7% clay, 25% silt, 63% sand, and 5% gravel with a uniformity coefficient 37.1. (Ueno et al., 2010) The optimum water content is 29% with a maximum dry density 1.3 g/cm^3. The slope soil is classified as a high frost-susceptible soil with

a tested frost heave rate 0.39 mm/h. The soil water characteristic curve and saturated permeability of a soil named DLV-1 are referred as inputs for slope soil since particle size distribution of slope soil are close to that of DLV-1 soil (Guymon et al., 1993). The thermal conductivity and heat capacity of soil mineral is determined by referring same report. (Table 5.3) For sake of simplicity, the structure of pavement at top of slope is not simulated, hence the entire slope is made by slope soil.

Table 5.3 Input parameters in soil slope analysis

Parameters	Values
Dry density of soil (ρ_d) kg/m^3	1300
Porosity (n)	0.482
Thermal conductivity of soil particles (λ_s) W/m°C	0.45
Thermal conductivity material parameter (χ)	0.75
Thermal conductivity material parameter (η)	1.20
Thermal conductivity empirical parameter (κ) unfrozen/ frozen	1.90/0.85
Volumetric heat capacity of soil particles (C_{Tp}) J/m^3°C	1.26E+6
van Genuchten-Mualem fitting parameter (α) 1/MPa	126.8
van Genuchten-Mualem fitting parameter (λ)	1.136
Saturated degree of saturation (S_{rs}) %	100.0
Residual degree of saturation (S_{rr}) %	0.300
Saturated water hydraulic conductivity in horizontal direction (k_{sh}) m/s	5.6E-6
Saturated water hydraulic conductivity in vertical direction (k_{sv}) m/s	1.4E-6
Young's modulus of soil (E) MPa	40.0
Poisson's ratio (υ)	0.33

5.9.3 Initial and boundary conditions

Mechanical boundary condition

The deformation on the left and right boundary are fixed, while vertical direction constraint is acted at bottom of model. The slope surface is free to deform in initial condition analysis (self-weight induced consolidation) and in subsequent freeze-thaw analysis (frost heave and thaw settlement). The shoulder and toe of slope extend 2 m and 1 m to let slope surface deform compatibly, avoiding the unrealistic constraint from left and right sides.

Thermal boundary condition

The left and right sides are set as adiabatic boundaries, while the temperature at the bottom of the model is set as annual average air temperature 7.1 °C. The daily average air temperature from nearby weather station during 2004-2005 is presented in Figure 5.24 together with measured

temperature at slope surface in site. The daily average air temperature is applied at slope surface and toe during unfrozen season as a rough approximation, while measured temperature at slope surface is imposed during freeze-thaw season. It is essential to consider thermal influence of black pavement at slope top in terms of temperature boundary, although pavement layers are not physically simulated by different materials. The pavement surface temperature is estimated through an empirical equation in Japanese pavement design handbook (Japan Road Association, 2006).

$$M_p = M_a\left(1+\frac{2.54}{z+10.16}\right)-\frac{25.4}{9(z+10.16)}+\frac{10}{3} \qquad 5.33$$

where, M_p is averaged pavement temperature, M_a is averaged air temperature and z is depth from pavement surface (cm).

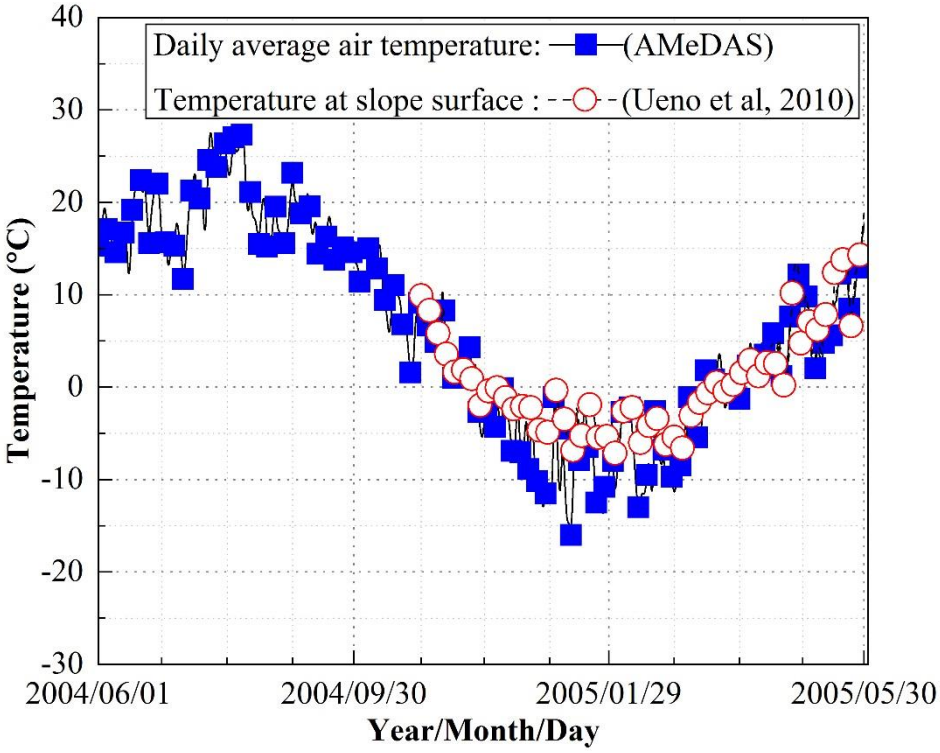

Figure 5.24 Daily average air temperature and temperature at slope surface

Hydraulic boundary condition

The water content in slope was measured in each October from 2005 to 2007 by sampling. (Ueno et al., 2010) The averaged water content for three years is around 30.6%, which corresponds to a calculated saturation of 82.5%. The groundwater table is deemed as 3 m below groundwater surface. The flux 6.985E-5 m/hour is applied at slope surface to simulate rainfall, which is calculated from 57 mm rainfall during 34 days prior to freezing season. The slope surface boundary is assigned as impervious boundary in freezing process, while it becomes drained boundary during thawing process. The constant pore pressure boundary is set at bottom of model

to simulate groundwater table, whereas left and right sides boundary are set as impervious boundary. The initial analysis is performed for three years until thermal equilibrium is achieved.

5.9.4 Results and discussions

Thermal field - Ground temperature at 30 cm depth

Figure 5.25 presents the comparison between the simulated and measured temperature at 30 cm depth below the middle of slope. Generally, the simulated time history of temperature matches with measured one. The temperature at 30 cm ground depth reaches 0 °C in early January, after one month's heat transfer between slope and atmosphere. The simulated temperature drops slightly faster during freezing season and rises during thawing season slightly faster than measured one, it is may induced by enlarged thermal conductivity assigned for slope soil. A platform appears when temperature approaches 0 °C both for simulated and measured ones, because of consumption of latent heat accompanying with water-ice phase change.

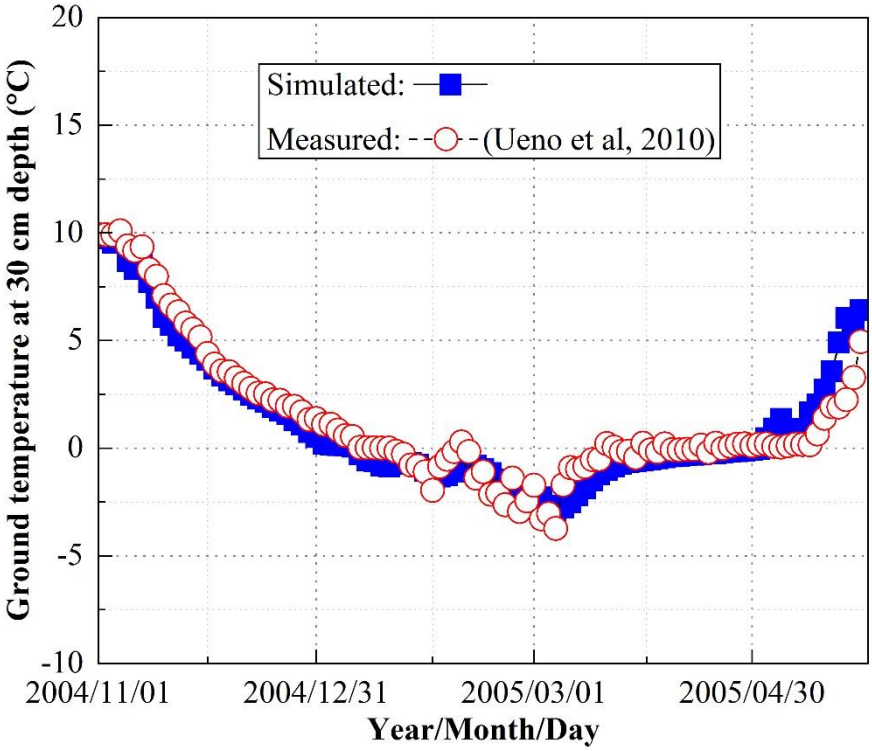

Figure 5.25 Ground temperature at 30 cm depth

Ground temperate at 30 cm fluctuates more severely in late winter (2005/01/30-2005/03/01) than that in early winter (2004/12/01-2005/01/30). A possible reason is that soil at 30 cm depth is located below freezing front and is still unfrozen in early winter. The freezing front, where water-ice phase transition takes place, behaves like a thermal barrier, which let soil underneath it relatively not sensitive to surface temperature fluctuations. However, once the freezing front pass through the 30 cm depth and the soil there is frozen, thermal conductivity and the thermal gradient

are increased compared with unfrozen one, the temperature fluctuates more severely following change of surface temperature.

Thermal field - Frost penetration depth

Figure 5.26 compares the simulated frost penetration depth with the measured one. The maximum frost penetration depth is around 60 cm and is reached on March 12th. The Simulated one matches with the measured well-considering uncertainty in field. However, simulated curve is with several platforms and is not smooth enough, as the mesh assigned is still not sufficiently fine. The lumped temperature in element and consumption of latent heat may also contribute to this phenomenon.

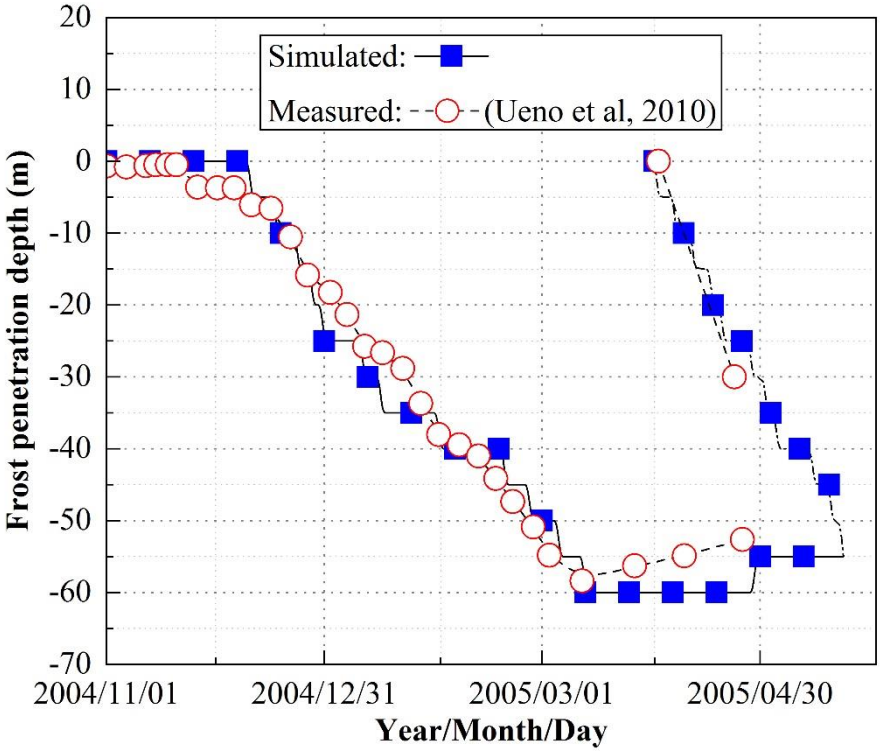

Figure 5.26 Variation of frost penetration depth

Thermal field - Temperature distribution

Simulated temperature distribution on March 1st, 2005 is presented in Figure 5.27. The temperature at slope top is lower than that at slope toe corresponding with the temperature boundary applied. A high-temperature core remains deep under pavement which provides stored heat to resists advance of frost line. The frost penetration is not parallel to slope surface from slope top to slope toe. The penetration depth at slope top is larger than that at slope toe. Not only due to the assigned boundary but also due to special geometry feature, which let slope top (convex surface) is more sensitive to surface temperature change than slope toe (concave surface).

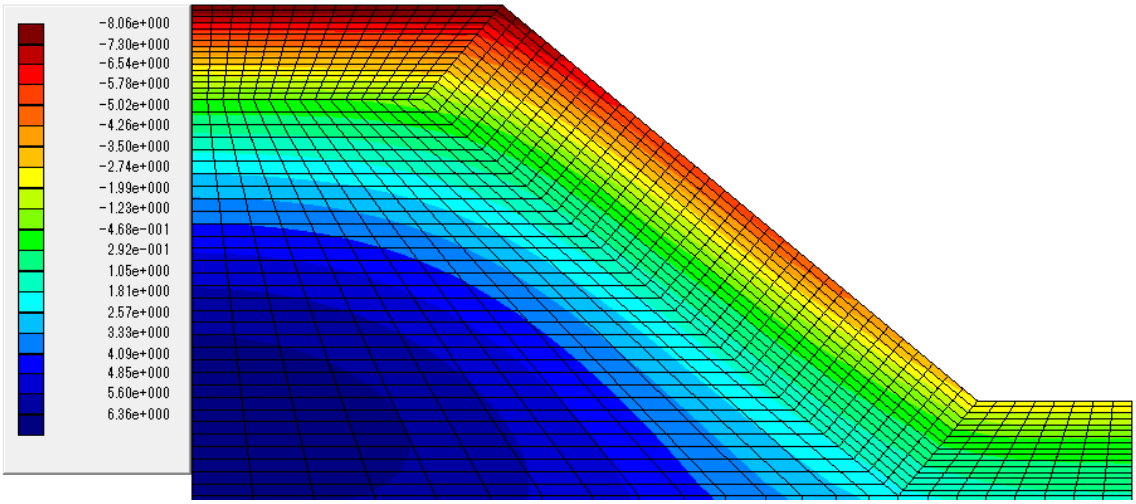

Figure 5.27 Simulated temperature distribution on March 1st, 2005 (Unit: Celsius degree)

Thermal field - Heat flow in slope

Simulated heat flux in slope on March 1st, 2005 is shown in Figure 5.28.

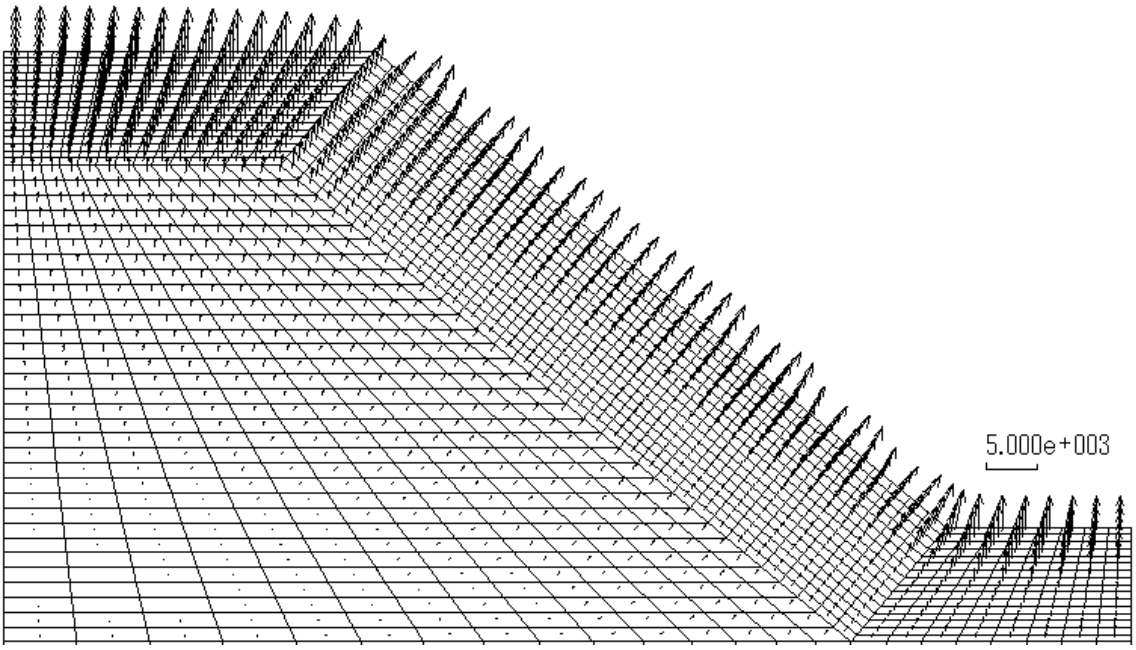

Figure 5.28 Simulated heat flow vector in slope on March 1st, 2005 (Unit: W/m^2)

Heat flow is associated with both thermal conductivity and thermal gradient based on Fourier's law of heat conduction. The heat flux is relatively large in the zone adjacent to the slope surface where thermal gradient and thermal conductivity becomes larger due to freezing. The heat flux at deep unfrozen ground away from surface is smaller as thermal gradient is more gentle and thermal conductivity is smaller compared with frozen zone. The direction of heat flux is along the thermal gradient direction, which is slightly towards upper side of slope and not necessarily parallel to

slope surface. The boundary between large and small heat flow vectors are overlapped with 0 °C line in Figure 5.27 which is also the boundary separating frozen and unfrozen zones.

Hydraulic field - Water saturation distribution

Figure 5.29 presents the distribution of (unfrozen/liquid) water saturation on March 1st, 2005. The water saturation at slope top is lower than that at slope toe as lower negative temperature leads in lower unfrozen water saturation. The water saturation along slope surface also coincides with negative temperature as shown in Figure 5.27. The water saturation increases with depth away from surface where remains unfrozen state until reaches groundwater table.

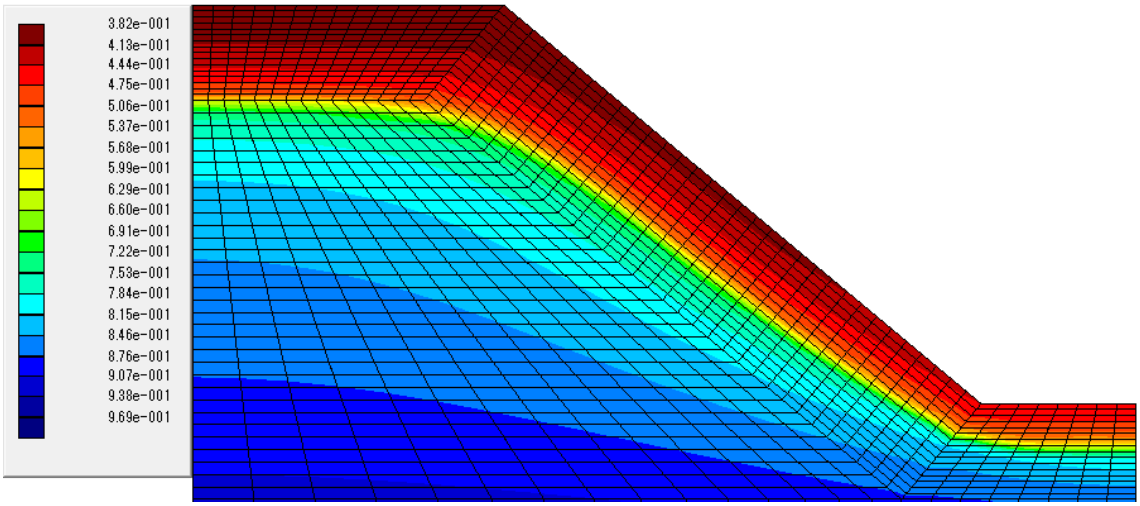

Figure 5.29 Simulated liquid-water saturation distribution on March 1st, 2005

Hydraulic field - Total water saturation

The total-water saturation (ice and unfrozen water) are presented in Figure 5.30.

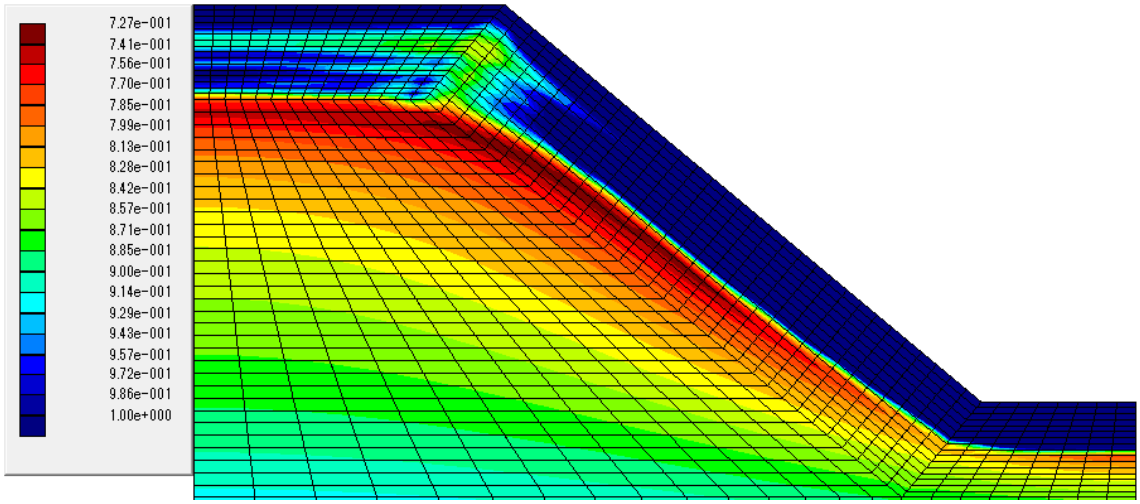

Figure 5.30 Simulated total-water saturation distribution on March 1st, 2005

In the shallow surface layer, the total saturation reaches 1.0 which illustrates that the soil skeleton separates and frost heave generates. A lower total saturation (0.727) layer exists below the freezing front where soil is unfrozen, and water is transported to freezing front.

Figure 5.31 shows change of total water saturation during the freezing season which is difference between November 1st, 2004 and March 1st, 2005 and means temporal accumulation of water mass. The plus-value stands for water absorption, while minus value represents loss of water. Corresponding with Figure 5.30, the water from subsurface soil migrates towards freezing front. The simulated increase of total saturation mainly occurs within top 40 cm soil below slope surface, while loss of water mainly happens at depth from 40 cm to 80 cm matching with measurement well (Ueno et al., 2010).

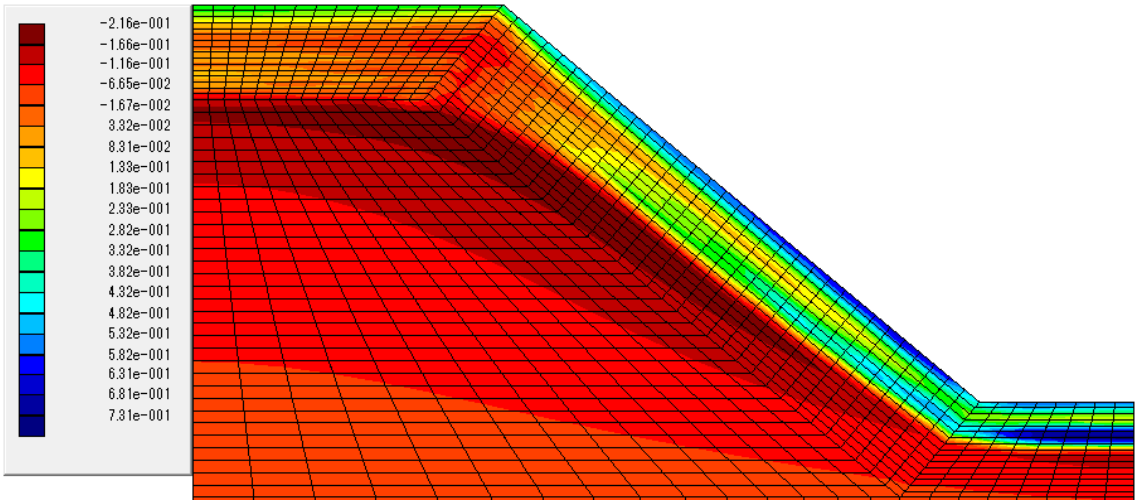

Figure 5.31 Simulated water redistribution during November 1st, 2004 to March 1st, 2005

Hydraulic field - Water-ice phase change

Latent heat is consumed when pore-water in the soil is frozen and water-ice phase transition takes place (Figure 5.32). The boundary between zero and non-zero value is freezing front which corresponds with 0 °C isothermal in Figure 5.27. The location of large latent heat value is same as that of total water accumulation as shown in Figure 5.31, which indicates location of ice accumulation, namely the location of ice lens.

Hydraulic field - Pore-water pressure and water flux in slope

Pore-water pressure distribution is shown in Figure 5.33. The large plus value (suction) generates in shallow layer subjected to negative temperature. The distribution of pore-water pressure agrees with temperature distribution in Figure 5.27 and water saturation distribution in Figure 5.29.

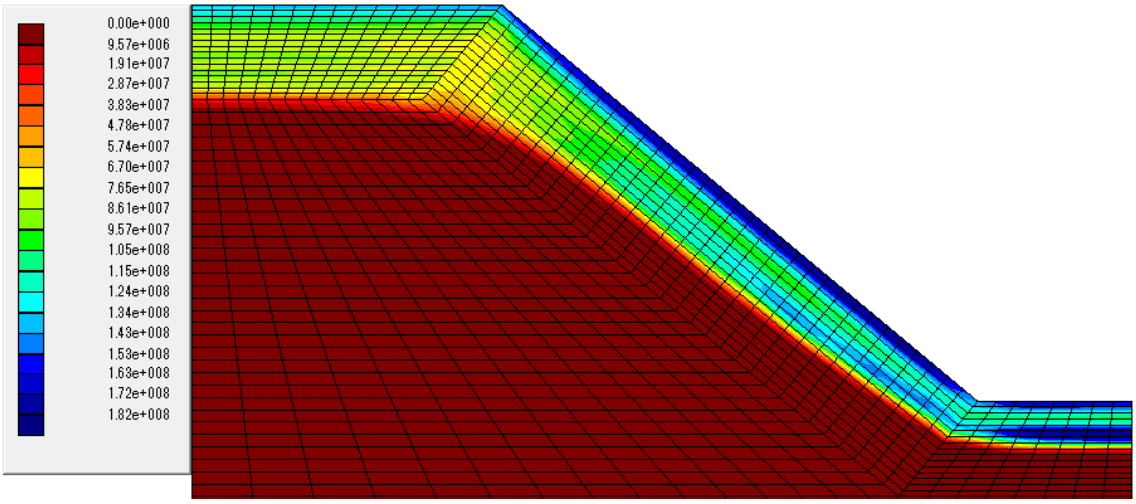

Figure 5.32 Simulated latent heat for water-ice phase change on March 1st, 2005 (Unit: J)

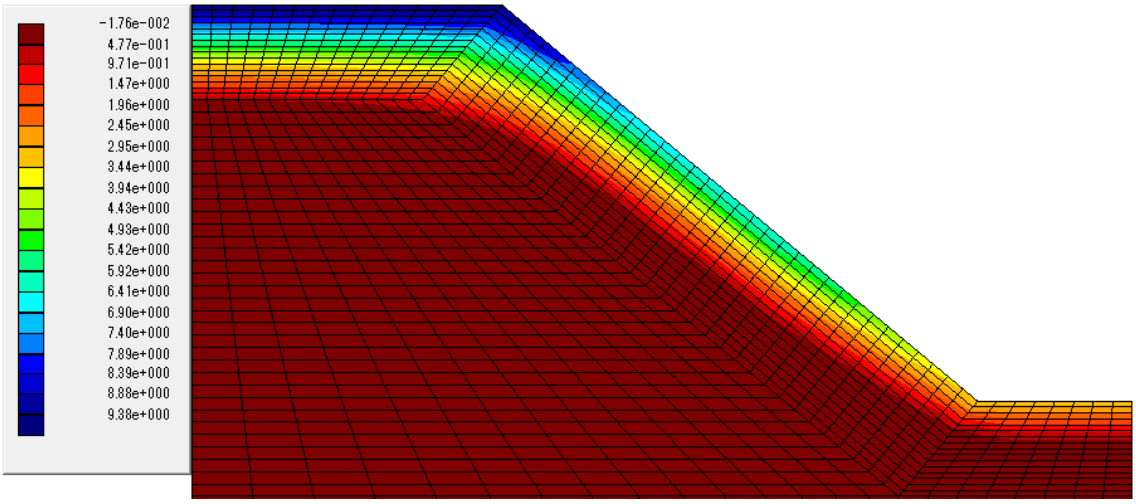

Figure 5.33 Simulated pore-water pressure distribution on March 1st, 2005 (Unit: MPa)

Figure 5.34 shows simulated water flux in slope. The water flows towards freezing front from lower to upper part of the slope. The water flux is associated with hydraulic conductivity and pore-water pressure gradient according to Darcy's law. In the unfrozen zone, the water flux at slope top is smaller than that at slope toe, as slope top is far away from groundwater level and lower water saturation leads to smaller relative hydraulic conductivity. On the contrary, the slow freezing rate at slope toe enables water flow continuously towards freeing front. In the frozen zone, the water flux is very small and negligible as ice formation blocks the pathway for water flow resulting in very small conductivity, although the pore-pressure and hydraulic gradient are considerably large.

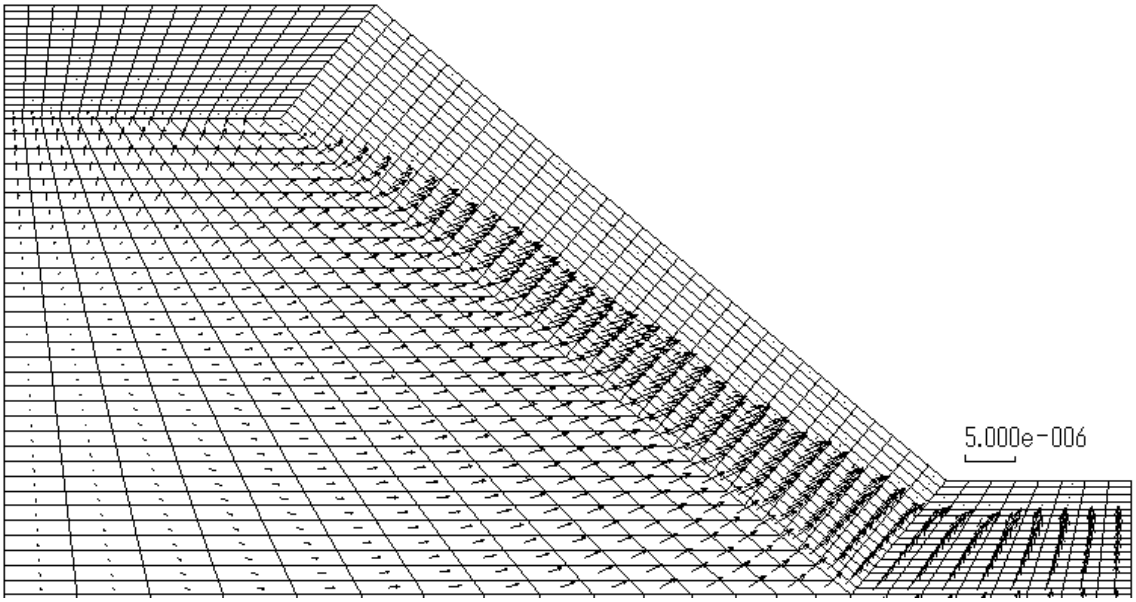

Figure 5.34 Simulated water flow vector in slope on March 1st, 2005 (Unit: m/h)

Mechanical field - Frost heave and thaw settlement

Figure 5.35 and Figure 5.36 shows frost heave and thaw settlement of the entire slope illustrating deformation pattern of soil slope subjected to freeze-thaw.

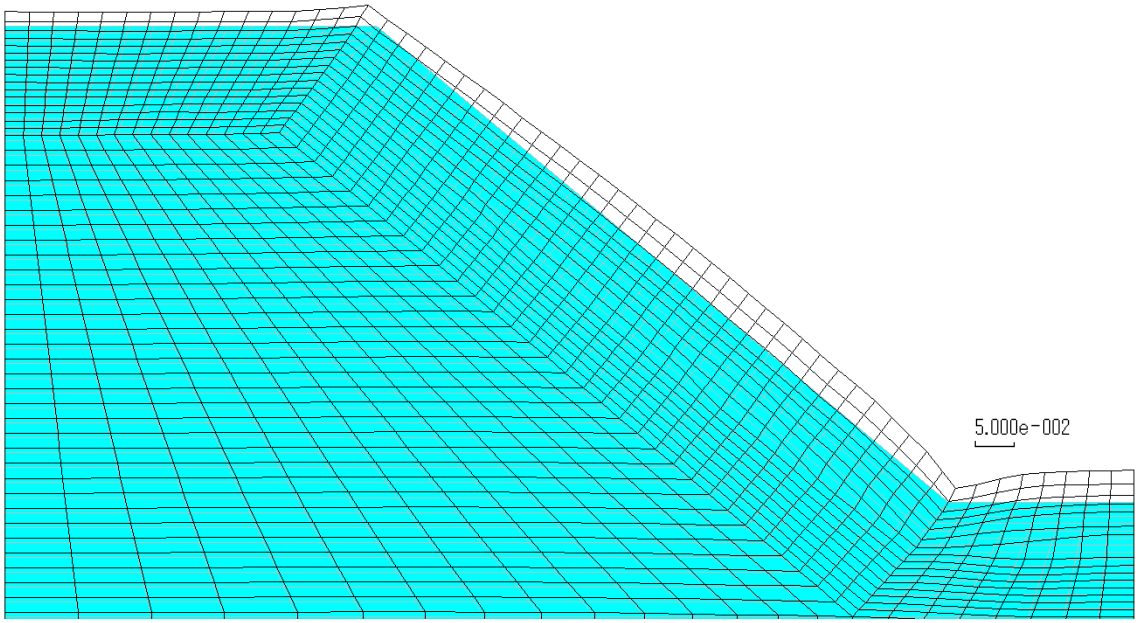

Figure 5.35 Simulated frost heave deformation on March 1st, 2005 (Unit: m)

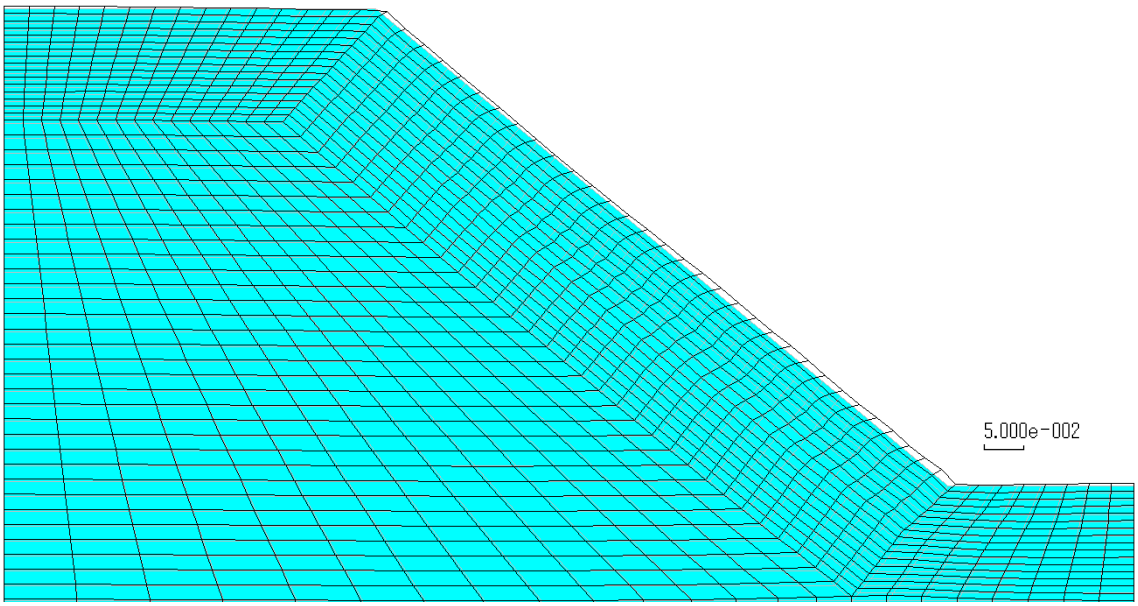

Figure 5.36 Simulated thaw settlement deformation on May 29th, 2005 (Unit: m)

The maximum frost heave is achieved at slope toe where the thermal and hydraulic conditions are most favorable for frost heave, namely sufficient water supply and small freezing rate (Figure 5.28, Figure 5.31, and Figure 5.32). Generally, the frost heave seems to develop along perpendicular direction of slope surface (Figure 5.35) which will be detailed discussed in following section. The thawed shallow surface soil settles when spring comes, and air temperature rises above 0 °C. However, the surface soil moves downward along slope surface, and not recover to initial position prior to freezing, thus residual deformation generates both in direction perpendicular to and along slope surface (Figure 5.36).

Mechanical field - Trajectory of measuring targets

Figure 5.37 shows a comparison of simulated and measured deformation along perpendicular direction to the slope surface. Generally, the trend and quantity of this deformation at three positions on slope surface are reproduced, although some difference remains in the early stage of freezing may due to unknown of exact soil properties and in-situ conditions. Figure 5.38 compares simulated deformation along slope surface direction with measured one. This deformation occurs which means the frost heave deformation does not happen along normal direction of slope as we usually think of. The minus value represents the upward movement along slope surface, while plus value stands for downward one.

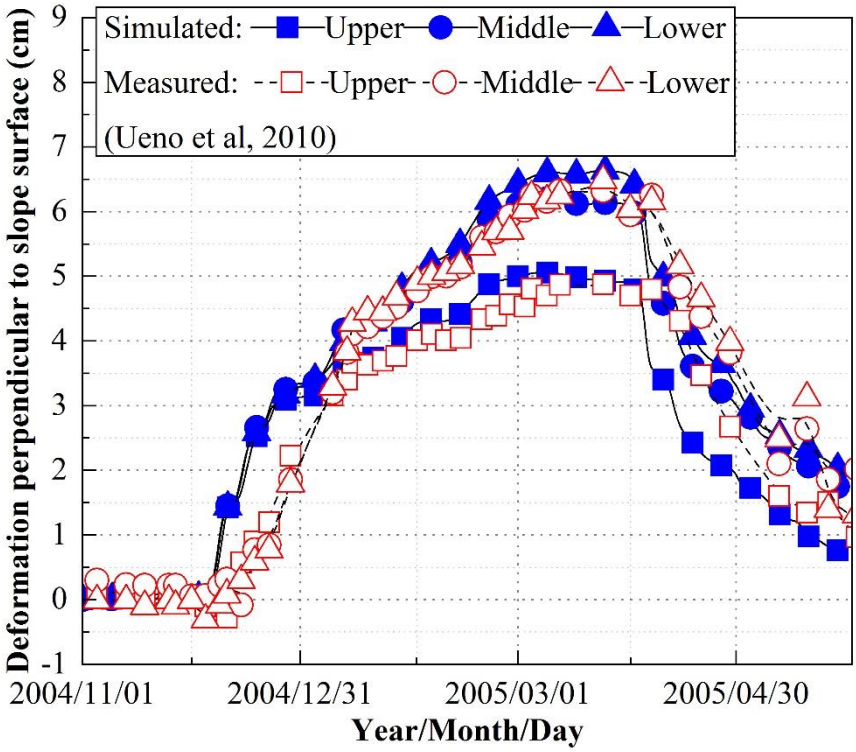

Figure 5.37 Deformation perpendicular to slope surface

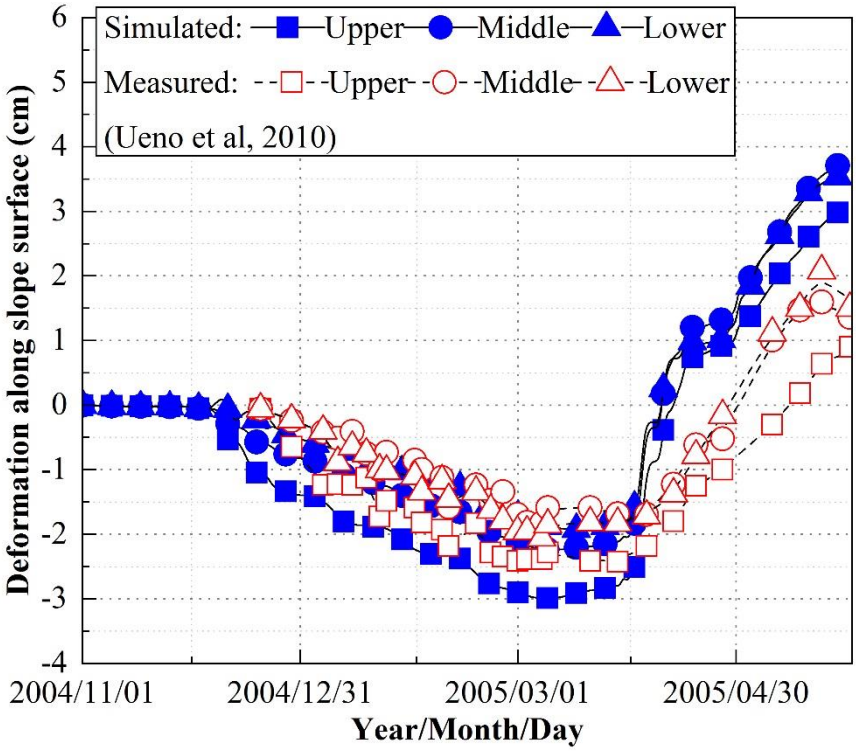

Figure 5.38 Deformation along slope surface

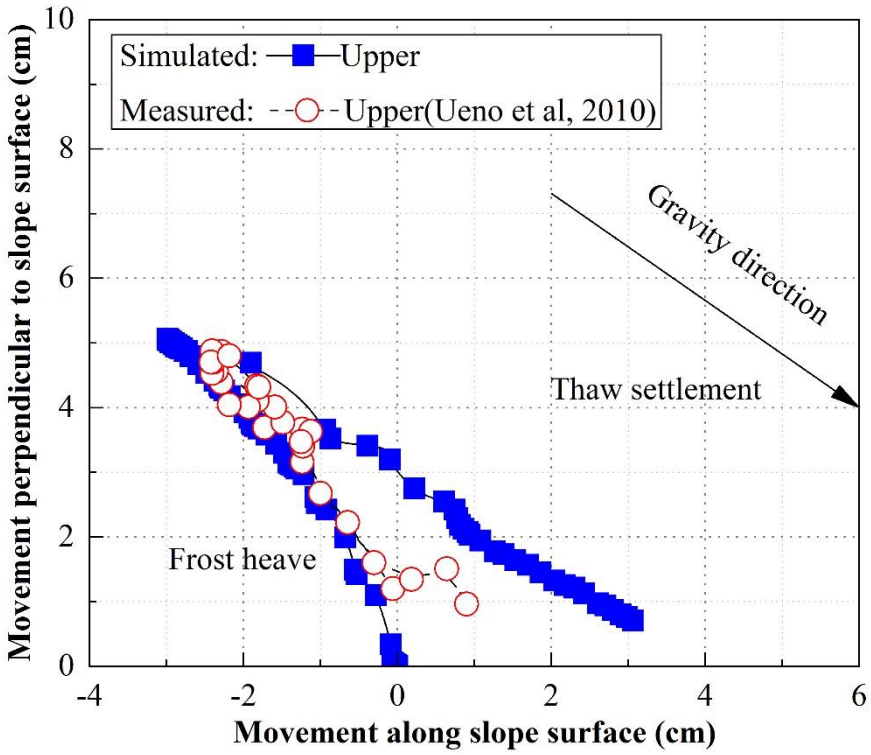

Figure 5.39 Trajectory of upper measuring target

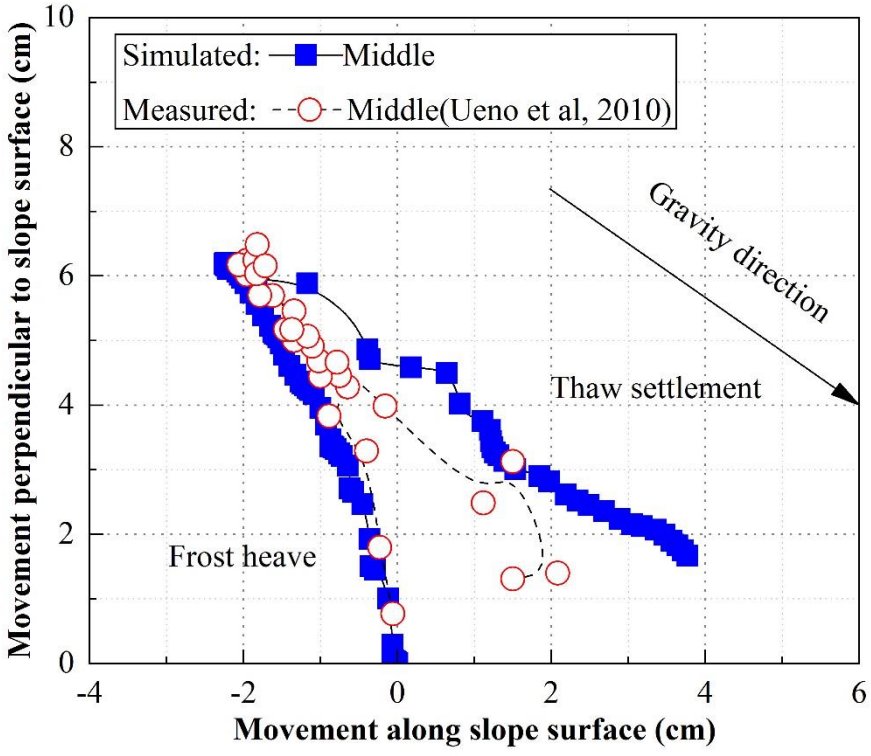

Figure 5.40 Trajectory of middle measuring target

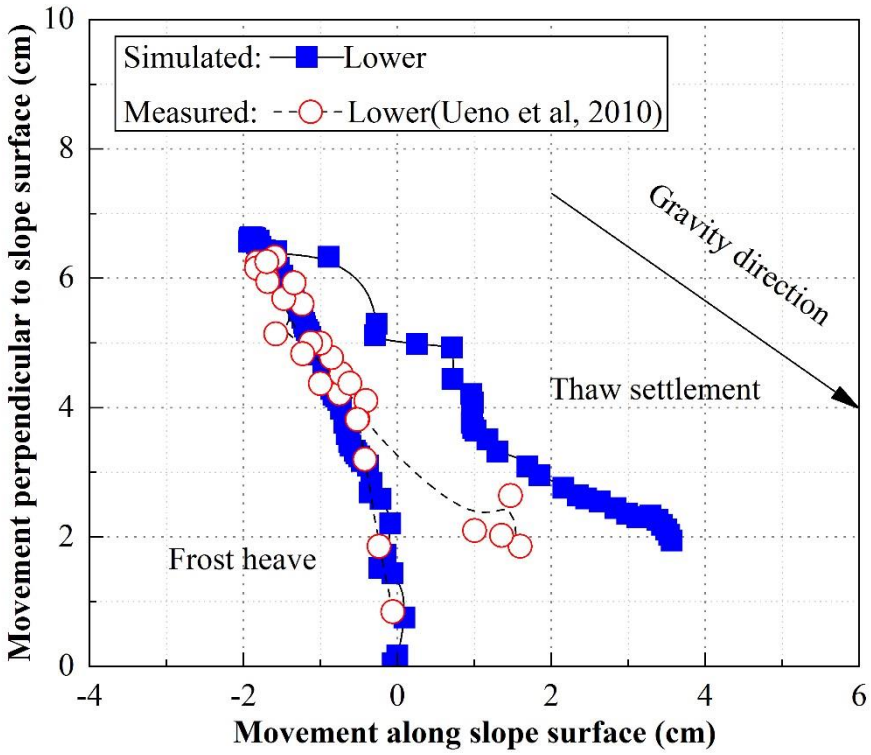

Figure 5.41 Trajectory of lower measuring target

As the deformation along two directions is known, the trajectory of measuring target can be determined as shown in Figure 5.39, Figure 5.40, and Figure 5.41. In these figures, the vertical axis direction is the perpendicular direction of slope surface, while horizontal axis direction is along slope surface. The frost heave generates along the direction slightly upward than perpendicular direction to slope surface, whereas thaw settlement roughly develops along gravity direction. The simulated frost heave roughly matches with measurement due to complex in-situ conditions and uncertainties, while simulated downslope movement always larger than measured one.

Mechanical field - Mechanism of observed phenomenon

It is generally believed that frost heave generates perpendicular to slope surface, however, both measurement and simulation disagree with this point. Frost heave generates along with heat flow and/or thermal gradient direction. In this study, as isothermals are not parallel to slope surface (Figure 5.27), heat flow and thermal gradient direction are not perpendicular to slope surface (Figure 5.28). For the difference between measured and simulated thaw settlement, a possible reason is that roots of vegetations may reinforce the shallow surface soil which restrains surface soil from freely settling down along gravity direct.

5.9.5 Remarks

The following conclusions can be drawn from this study:

1. The freeze-thaw behavior of a soil slope in season cold region is simulated through a coupling THM analysis. The thermal pattern of soil slope is reproduced in which frost penetration at slope top is deeper than that at slope toe and isothermal is not parallel to slope surface. The simulated variation of ground temperature at 30 cm depth below slope surface matches with measured one well, as well as frost penetration depth. The water redistribution induced by freezing is reproduced together with water-ice phase change and ice accumulation.

2. The frost heave and thaw settlement actions are correctly reproduced, then the mechanism of this unique deformation pattern is revealed. The frost heave generates in heat flow and/or thermal gradient direction, not necessary to be perpendicular to slope surface. Thaw settlement mainly develops along gravity direction, although vegetation roots may suppress this trend to some extent.

6 CONCLUSIONS AND RECOMMENDATIONS

The following conclusions can be derived from this study:

To study the freeze-thaw behavior of partially saturated soil, especially frost heave and thaw settlement, a thermo-hydro-mechanical model is presented. The validity of the model is examined through a comparison between the simulated and measured frost heave test results. The model is generally good at predicting the freeze-thaw action under different conditions, including water supply and overburden pressure.

A numerical study is performed on the freeze-thaw behavior of pavement around a box culvert. The simulation reproduced the primary behavior of the pavement during the freeze-thaw process. The frost penetration depth is much deeper for the pavement right above the culvert than in the adjacent zones. A hump and a dip of pavement appear above the culvert during the freeze and thaw processes, respectively. The frost heaving force is high enough to cause cracking of the culvert. Uneven frost heave and thermal contraction cause considerable tensile stress in the asphalt mixture layer and this has a more significant impact on the fatigue life than the wheel load. An insulation material wrapped around the culvert and above the frost-susceptible soil may mitigate the damage from uneven frost heave.

One more analysis is conducted to research stress change in pavement subjected to freeze-thaw. The thermal pattern in the pavement located in the cold region was reproduced. The snow cover on the footpath that affects temperature distribution in pavement should be properly considered. The presence of frost protection layer can effectively resist and limit frost penetration in the subgrade. The stress change in pavement is highly associated with the variation of resilient modulus that is sensitive to temperature. The stress variation in base course and frost protection layer presents a reverse trend compared with subgrade. The stress increment of subgrade in springtime may greatly deteriorate the performance of pavement and shorten its service life.

Further development of the existing model is carried out to overcome the limitations. The recent findings and progress in unsaturated and frozen soil area are integrated into the model. The nonlinear soil properties like hydraulic conductivity, thermal conductivity, and heat capacity are modeled. Furthermore, special attention is paid to incorporate the unsaturated with the freezing. The analogy between drying and freezing process is introduced into the model, together with the dependence of unfrozen water content on total water content. The frost heave and thaw settlement are modeled in a phenomenon-based way, although the level of sophistication is still far away from the author's expectation.

The new model is able to comprehensively capture main features of unsaturated freezing soil like suction induced freezing point depression, water-ice phase change, water redistribution caused by

cryogenic suction gradient, and most importantly, the frost heave and thaw settlement of soil. The validity of the model is examined by comparing simulated frost heave and thaw settlement with experimental results. Generally, the model predicts the frost heave and thaw settlement amount under various test conditions well. The effect of overburden pressure, water supply condition, initial degree of saturation and freezing rate on frost heave have been reproduced by proposed model.

A further study on freeze-thaw behavior of a soil slope in season cold region is simulated through a coupling THM analysis. The thermal pattern of soil slope is reproduced in which frost penetration at slope top is deeper than that at slope toe and isothermal is not parallel to slope surface. The simulated variation of ground temperature at 30 cm depth below slope surface matches with measured one well, as well as frost penetration depth. The water redistribution induced by freezing is reproduced together with water-ice phase change and ice accumulation. The frost heave and thaw settlement actions are correctly reproduced, then mechanism of this unique deformation pattern is revealed. The frost heave generates in heat flow and/or thermal gradient direction, not necessary to be perpendicular to slope surface. Thaw settlement mainly develops along gravity direction, although vegetation roots may suppress this trend to some extent.

All these studies demonstrate that the proposed model is ready for a field-scale application. However, we should note that the limitations and drawbacks remain.

LIST OF REFERENCES

1. Abe R, Kumagai M, Maruyama K. A study of materials and environmental conditions for mechanistic-empirical pavement design in cold snowy regions. Journal of Japan Society of Civil Engineers, Ser. E1 (Pavement Engineering), 2011, 67(3): 17-25. (in Japanese)
2. Andersland O B, Ladanyi B. Frozen ground engineering[M]. Wiley, Hoboken, NJ, 2004.
3. Bishop A W. The principle of effective stress[J]. Teknisk ukeblad, 1959, 39: 859-863.
4. Cole D M, Irwin L H, Johnson T C. Effect of freezing and thawing on resilient modulus of a granular soil exhibiting nonlinear behavior[J]. Transportation Research Record, 1981, 809: 19-26.
5. Corapcioglu M Y, Panday S. Multiphase approach to thaw subsidence of unsaturated frozen soils: Equation development[J]. Journal of engineering mechanics, 1995, 121(3): 448-459.
6. Côté J, Konrad J M. A generalized thermal conductivity model for soils and construction materials[J]. Canadian Geotechnical Journal, 2005, 42(2): 443-458.
7. Dall'Amico M, Endrizzi S, Gruber S, et al. A robust and energy-conserving model of freezing variably-saturated soil[J]. The Cryosphere, 2011, 5(2): 469-484.
8. Fredlund D G, Morgenstern N R. Constitutive relations for volume change in unsaturated soils[J]. Canadian Geotechnical Journal, 1976, 13(3): 261-276.
9. Gilpin R R. A model for the prediction of ice lensing and frost heave in soils[J]. Water Resources Research, 1980, 16(5): 918-930.
10. Guymon G L, Berg R L, Hromadka T V. Mathematical model of frost heave and thaw settlement in pavements[R]. Cold Regions Research and Engineering Lab Hanover NH, 1993.
11. Guymon G L, Hromadka Ii T V, Berg R L. A one dimensional frost heave model based upon simulation of simultaneous heat and water flux[J]. Cold Regions Science and Technology, 1980, 3(2-3): 253-262.
12. Guymon G L, Hromadka T V, Berg R L. Two-dimensional model of coupled heat and moisture transport in frost-heaving soils[J]. Journal of energy resources technology, 1984, 106(3): 336-343.
13. Guymon G L, Luthin J N. A coupled heat and moisture transport model for arctic soils[J]. Water Resources Research, 1974, 10(5): 995-1001.
14. Hansson K, Šimůnek J, Mizoguchi M, et al. Water flow and heat transport in frozen soil[J]. Vadose Zone Journal, 2004, 3(2): 693-704.
15. Harlan R L. Analysis of coupled heat‐fluid transport in partially frozen soil[J]. Water Resources Research, 1973, 9(5): 1314-1323.
16. Harris C, Davies M C R, Coutard J P. Laboratory simulation of periglacial solifluction:

significance of porewater pressures, moisture contents and undrained shear strengths during soil thawing[J]. Permafrost and periglacial processes, 1995, 6(4): 293-311.
17. Harris C, Kern‐Luetschg M, Smith F, et al. Solifluction processes in an area of seasonal ground freezing, Dovrefjell, Norway[J]. Permafrost and Periglacial Processes, 2008, 19(1): 31-47.
18. Harris C, Rea B, Davies M. Scaled physical modelling of mass movement processes on thawing slopes[J]. Permafrost and Periglacial Processes, 2001, 12(1): 125-135.
19. Hayashi K, Suzuki T, Toyota K. Study on the shape of freezing front and frost heave damage of C-box structure[M]. Current Practices in Cold Regions Engineering. 2006: 1-14.
20. Higashi A, Corte A E. Solifluction: a model experiment[J]. Science, 1971, 171(3970): 480-482.
21. Hopke S W. A model for frost heave including overburden[J]. Cold Regions Science and Technology, 1980, 3(2-3): 111-127.
22. Ishikawa T, Tokoro T, Akagawa S. Frost heave behavior of unsaturated soils under low overburden pressure and its estimation[C]. Proceedings of GEO Quebec, 2015.
23. Janoo V C, Berg R L. Thaw weakening of pavement structures in seasonal frost areas[J]. Transportation Research Record, 1990, 1286, 217-233.
24. Japanese Geotechnical Society. Test method for frost heave prediction of soils, In Japanese Geotechnical Society Standards-Laboratory Testing Standards of Geomaterials, Japanese Geotechnical Society, Tokyo, Vol. 1, 2015.
25. Japan Road Association. Pavement design handbook[M]. Japan Road Association, Tokyo, 2006. (in Japanese)
26. Johansen O. Thermal conductivity of soils[R]. Cold Regions Research and Engineering Lab Hanover NH, 1977.
27. Johnston G H, Ladanyi B, Morgenstern N R, et al. Engineering characteristics of frozen and thawing soils[J]. Permafrost Engineering Design and Construction. Edited by Johnston, GH John Wiley & Sons, 1981.
28. Kishikawa, T, Otgonjargal, D, Kawaguchi, T, et al. Influence of freeze-thaw on stress propagation in the ground[C], Proceedings of Technical Report of the Annual Meeting of the JGS Hokkaido Branch, 2017. (in Japanese).
29. Konrad J M, Morgenstern N R. A mechanistic theory of ice lens formation in fine-grained soils[J]. Canadian Geotechnical Journal, 1980, 17(4): 473-486.
30. Konrad J M, Morgenstern N R. The segregation potential of a freezing soil[J]. Canadian Geotechnical Journal, 1981, 18(4): 482-491.
31. Konrad J M, Morgenstern N R. Effects of applied pressure on freezing soils[J]. Canadian

Geotechnical Journal, 1982, 19(4): 494-505.
32. Konrad J M, Morgenstern N R. Frost heave prediction of chilled pipelines buried in unfrozen soils[J]. Canadian Geotechnical Journal, 1984, 21(1): 100-115.
33. Koopmans R W R, Miller R D. Soil Freezing and Soil Water Characteristic Curves 1[J]. Soil Science Society of America Journal, 1966, 30(6): 680-685.
34. Li N, Chen B, Chen F, et al. The coupled heat-moisture-mechanic model of the frozen soil[J]. Cold Regions Science and Technology, 2000, 31(3): 199-205.
35. Li N, Chen F, Su B, et al. Theoretical frame of the saturated freezing soil[J]. Cold Regions Science and Technology, 2002, 35(2): 73-80.
36. Li N, Chen F, Xu B, et al. Theoretical modeling framework for an unsaturated freezing soil[J]. Cold Regions Science and Technology, 2008, 54(1): 19-35.
37. Li S, Lai Y, Pei W, et al. Moisture–temperature changes and freeze–thaw hazards on a canal in seasonally frozen regions[J]. Natural hazards, 2014, 72(2): 287-308.
38. Li S, Zhang M, Tian Y, et al. Experimental and numerical investigations on frost damage mechanism of a canal in cold regions[J]. Cold Regions Science and Technology, 2015, 116: 1-11.
39. Liu Z, Yu X. Coupled thermo-hydro-mechanical model for porous materials under frost action: theory and implementation[J]. Acta Geotechnica, 2011, 6(2): 51-65.
40. Matsumoto H, Yamada S, Hirakawa K. Relationship between ground ice and solifluction: field measurements in the Daisetsu Mountains, Northern Japan[J]. Permafrost and Periglacial Processes, 2010, 21(1): 78-89.
41. Matsuoka N. The relationship between frost heave and downslope soil movement: field measurements in the Japanese Alps[J]. Permafrost and Periglacial Processes, 1998, 9(2): 121-133.
42. Matsuoka N, Moriwaki K. Frost heave and creep in the Sør Rondane Mountains, Antarctica[J]. Arctic and Alpine Research, 1992, 24(4): 271-280.
43. Miller R D. Frost heaving in non-colloidal soils[C]. Proceeding 3rd International Conference Permafrost. National Research Council of Canada, 1978: 707-713.
44. Mu S, Ladanyi B. Modelling of coupled heat, moisture and stress field in freezing soil[J]. Cold Regions Science and Technology, 1987, 14(3): 237-246.
45. Mualem Y. A new model for predicting the hydraulic conductivity of unsaturated porous media[J]. Water resources research, 1976, 12(3): 513-522.
46. Newman G P, Wilson G W. Heat and mass transfer in unsaturated soils during freezing[J]. Canadian Geotechnical Journal, 1997, 34(1): 63-70.
47. Nishimura S, Gens A, Olivella S, et al. THM-coupled finite element analysis of frozen soil: formulation and application[J]. Géotechnique, 2009, 59(3): 159.

48. Nixon J F. Discrete ice lens theory for frost heave in soils[J]. Canadian Geotechnical Journal, 1991, 28(6): 843-859.
49. O'Neill K, Miller R D. Exploration of a rigid ice model of frost heave[J]. Water Resources Research, 1985, 21(3): 281-296.
50. Painter S L, Karra S. Constitutive model for unfrozen water content in subfreezing unsaturated soils[J]. Vadose Zone Journal, 2014, 13(4).
51. Potts D M, Zdravkovic L. Finite element analysis in geotechnical engineering: theory [M]. Thomas Telford, 1999.
52. Richards L A. Capillary conduction of liquids through porous mediums[J]. Physics, 1931, 1(5): 318-333.
53. Rui D, Ji M, Nakamur D, et al. Experimental study on gravitational erosion process of vegetation slope under freeze–thaw[J]. Cold Regions Science and Technology, 2018, 151: 168-178.
54. Sheng D, Axelsson K, Knutsson S. Frost heave due to ice lens formation in freezing soils: 1. Theory and verification[J]. Hydrology Research, 1995, 26(2): 125-146.
55. Sheng D, Zhang S, Yu Z, et al. Assessing frost susceptibility of soils using PCHeave[J]. Cold Regions Science and Technology, 2013, 95: 27-38.
56. Shoop S A, Bigl S R. Moisture migration during freeze and thaw of unsaturated soils: modeling and large scale experiments[J]. Cold Regions Science and Technology, 1997, 25(1): 33-45.
57. Simonsen E, Isacsson U. Soil behavior during freezing and thawing using variable and constant confining pressure triaxial tests[J]. Canadian Geotechnical Journal, 2001, 38(4): 863-875.
58. Simonsen E, Janoo V C, Isacsson U. Resilient properties of unbound road materials during seasonal frost conditions[J]. Journal of Cold Regions Engineering, 2002, 16(1): 28-50.
59. Skempton A W. The pore-pressure coefficients A and B[J]. Geotechnique, 1954, 4(4): 143-147.
60. Tai B, Liu J, Wang T, et al. Numerical modelling of anti-frost heave measures of high-speed railway subgrade in cold regions[J]. Cold Regions Science and Technology, 2017, 141: 28-35.
61. Taylor G S, Luthin J N. A model for coupled heat and moisture transfer during soil freezing[J]. Canadian Geotechnical Journal, 1978, 15(4): 548-555.
62. Thomas H R, Cleall P J, Li Y, et al. Modelling of cryogenic processes in permafrost and seasonally frozen soils[J]. Geotechnique, 2009, 59(3): 173-184.
63. Tokoro T, Kimura K, Ishikawa T, et al. Temperature dependency of permeability

coefficient of frozen soil[C]. Proceedings of GEO Vancouver, 2016.
64. Toyota K., Yamaguchi K, Saito K, et al. Frost heaving properties of backfill soil around box-culvert[C], Proceedings of Technical Report of the Annual Meeting of the JGS Hokkaido Branch, 2002. (in Japanese)
65. Tozuka S, Toyota K, Mizuno T, et al. Field verification on frost heaving prevention of berm drainage canal at face of cut slope in cold area[C]. Proceedings of Technical Report of the Annual Meeting of the JGS Hokkaido Branch, 2006. (in Japanese).
66. Ueno K, Rui D, Nakamura D, et al. Behavior of vegetation protection slopes during freezing and thawing[J]. Soils Found, 2010, 5: 413-424. (in Japanese)
67. Van Genuchten M T. A closed-form equation for predicting the hydraulic conductivity of unsaturated soils 1[J]. Soil science society of America journal, 1980, 44(5): 892-898.
68. Williams P J. Unfrozen water content of frozen soils and soil moisture suction[J]. Geotechnique, 1964, 14(3): 231-246.
69. Yin X, Liu E, Song B, et al. Numerical analysis of coupled liquid water, vapor, stress and heat transport in unsaturated freezing soil[J]. Cold Regions Science and Technology, 2018, 155: 20-28.
70. Zhang S, Teng J, He Z, et al. Importance of vapor flow in unsaturated freezing soil: a numerical study[J]. Cold Regions Science and Technology, 2016, 126: 1-9.
71. Zhang Y, Michalowski R L. Thermal-hydro-mechanical analysis of frost heave and thaw settlement[J]. Journal of geotechnical and geoenvironmental engineering, 2015, 141(7): 04015027.
72. Zheng H, Kanie S. Combined thermal-hydraulic-mechanical frost heave model based on Takashi's equation[J]. Journal of Cold Regions Engineering, 2014, 29(4): 04014019.
73. Zhou J, Li D. Numerical analysis of coupled water, heat and stress in saturated freezing soil[J]. Cold Regions Science and Technology, 2012, 72: 43-49.

LIST OF NOTATIONS

Description	Symbol
Apparent heat capacity of soil	C_{Ta}
Bulk modulus of water	K_w
Bulk modulus for the soil structure	K
Bulk modulus for the soil structure under drained conditions	K_d
Bulk modulus for the soil structure under undrained conditions	K_u
Coefficient of frozen water permeability	k_{wf}
Coefficient of thaw contraction	ω
Coefficient of water permeability	k_w
Coefficient of water permeability when mean effective stress equals 0	k_0
Degree of saturation for liquid water	S_w
Degree of saturation for ice	S_i
Degree of saturation including water in liquid and solid phase	S_r
Density of water	ρ_w
Displacement vector of soil element	$\boldsymbol{u}$
Divergence operator	$\nabla\cdot$
Dry density of soil	ρ_d
Effective degree of saturation	S_e
Effective stress at the direction of heat flow	σ'_n
Elastic constant tensor	C_{ijkl}
Elevation	z
Final freezing temperature	T_f
Freezing point depression	T_f
Frost heave fitting parameter	κ_f
Frost heave fitting parameter	ς
Frost heave or thaw settlement strain	$\varepsilon_{f/t}$
Frost heave strain	ε_f
Flux vector of water	$\boldsymbol{v_w}$
Gradient operator	∇
Gravity acceleration	g
Heaviside function	H_e
Ice pressure	u_i
Impedance factor	Ω
Increment of water content by moisture migration	$\Delta\theta$

Infinitesimal strain tensor	ε_{ij}
Initial degree of saturation	S_{w0}
Initial volumetric water content pre-freezing	θ_0
Kronecker delta	δ_{ij}
Latent heat of fusion of water	L
Mass of water	M_w
Maximum frost expansion strain of saturated soil without overburden pressure	ε_{fmax}
Mean effective stress	σ'_m
Mean strain tensor	ε_{kk}
Mean total normal stress	σ_m
Modulus of elasticity for soil structure with respect to change in matric suction	H
Nominal freezing temperature	T_0
Normalized thermal conductivity	k_{Tr}
Overburden pressure	u_{ob}
Pore-air pressure	u_a
Pore-pressure coefficient B	β
Pore-water pressure	u_w
Pore-water pressure (suction) prior to freezing	u_{w0}
Porosity	n
Reciprocal of volume elastic constant of the pore water	K_b
Relative water hydraulic conductivity	k_{wr}
Residual degree of saturation	S_{rr}
Saturated degree of saturation	S_{rs}
Saturated water hydraulic conductivity	k_s
Saturated water hydraulic conductivity fitting parameter	a
Shear modulus for the soil structure	G
Slope of soil freezing characteristic curve (SFCC)	$\partial\theta_i/\partial T$
Specific moisture capacity of soil	C_H
Storage volume of water per unit volume	m
Strain of water	ε_w
Suction	ψ
Temperature	T
Tensile strength of soil	u_{sep}
Thermal conductivity empirical parameter	κ
Thermal conductivity material parameter	χ
Thermal conductivity material parameter	η

Thermal conductivity of dry soil	λ_{dry}
Thermal conductivity of frozen soil	λ_f
Thermal conductivity of ice	λ_i
Thermal conductivity of saturated soil	λ_{sat}
Thermal conductivity of soil	λ_T
Thermal conductivity of unfrozen soil	λ_u
Thermal conductivity of water	λ_w
Thermal conductivity of soil particles	λ_s
Thaw settlement fitting parameter	c
Thaw settlement fitting parameter	d
Thaw settlement strain	ε_t
Thermal expansion coefficient of soil under drained condition	α_{Td}
Thermal expansion coefficient of soil under undrained condition	α_{Tu}
Thermal expansion coefficient of water	α_{Tw}
Time	t
Total hydraulic potential head	h
Total latent heat stored in water	L_f
Total stress at the direction of heat flow/gravity	σ_n
Total stress tensor	σ_{ij}
van Genuchten-Mualem fitting parameter	α
van Genuchten-Mualem fitting parameter	λ
Volume of soil element	V_0
Volume of water	V_w
Volumetric ice content	θ_i
Volumetric heat capacity of ice	C_{Ti}
Volumetric heat capacity of soil	C_T
Volumetric heat capacity of soil particles	C_{Tp}
Volumetric heat capacity of water	C_{Tw}
Volumetric strain of soil element	ε_v
Volumetric unfrozen water content	θ_u
Volumetric water content	θ_w
Young's modulus of soil	E
Young's modulus of frozen soil	E_f
Young's modulus of unfrozen soil	E_u